Biomechanics-driven Stochastic Learning for Human Motion Sensing Systems

February 2021

Ryo Eguchi

A Thesis for the Degree of Ph.D. in Engineering

Biomechanics-driven Stochastic Learning for Human Motion Sensing Systems

February 2021

Graduate School of Science and Technology
Keio University

Ryo Eguchi

SUMMARY OF Ph.D. DISSERTATION

Human motion sensing technologies have recently attracted attention in the fields of medicine and healthcare. To estimate and track human motions using wearable/fixed sensors, the sensing systems must model the user-specific relationship between the sensor measurements and the motion parameters or complex motion dynamics. However, the estimation accuracies of previous learning approaches were diminished through overfitting when the diversity and size of the dataset were constrained by device resources and users' motor capacities. In addition, a single model cannot adapt to changes in the sensor-motion relationship due to sensing conditions and complicated motions that cannot be represented by one specific model. To address these issues, this dissertation presents biomechanics-driven stochastic learning for the motion sensing systems, which achieves data-efficient learning of estimation models using limited datasets and adaptive estimation using multiple models.

Chapter 1 describes the background and major contributions of the dissertation.

Chapter 2 presents the force plate-free learning for estimating the vertical ground reaction force (vGRF) using insoles instrumented with a small number of force sensors. The system learns a regression model using sensor measurements obtained during a single leg stance, by applying the biomechanics that the vGRF approximately matches the body weight. The regression avoids overfitting through biomechanical constraints that peak/trough vGRFs are linear with respect to stance duration during walking.

Chapter 3 presents the insole-based estimation of vGRF for users with decreased motor abilities. The system probabilistically augments the sensor measurements and vGRFs for a single step to a dataset for multiple steps, using the biomechanical assumption that measurements vary owing to the inconsistency of walking. A Gaussian process regression model is then learned to prevent overfitting.

Chapter 4 presents a shift-adaptive estimation of the knee joint angle using an instrumented brace. The system learns relationships between the strains of two stretch sensors and joint angles at varying brace positions using Gaussian mixture models (GMMs). This utilizes the biomechanics that skin strain decreases as the distance from the joint increases. The angle is then calculated adaptively to the brace shift using the maximum likelihood (ML) GMM identified by the sensor strains in a previous 1 s period.

Chapter 5 presents a learning-based occlusion compensation for leg tracking with a laser range sensor. The system learns relationships between leg trajectory and traveling direction for straight walking and turning under different curvatures/directions using GMMs. When an occlusion occurs during tracking, the walking type is identified by a joint probability of both legs' trajectories using biomechanics that they move in a coordinated manner. The ML GMM then estimates the direction and position of the hidden leg.

Chapter 6 summarizes the findings and presents the conclusions and future research directions.

Acknowledgment

This research was carried out by the author from April 2015 to March 2021 in the Takahashi Laboratory of the Graduate School of Science and Technology, Keio University, under the supervision of Professor Masaki Takahashi of the Faculty of Science and Technology at Keio University.

First, I would like to express my sincere gratitude to my supervisor, Prof. Masaki Takahashi, for his continuous support of my Ph.D. study and related research and for his patience, motivation, and immense knowledge. His guidance helped me in all phases of the research and writing of this thesis, and I cannot imagine having had a better advisor and mentor for my Ph.D. study.

I would also like to thank the rest of my thesis committee—Prof. Toshiyuki Murakami, Prof. Masayuki Kohiyama, and Associate Prof. Junichi Ushiba of Keio University—for their insightful comments, encouragement, and hard questioning, which widened my research from various perspectives.

I would like to express my sincere gratitude to Prof. Tomoki Aoyama of Kyoto University and Associate Prof. Takahiko Fukumoto of Kio University, who provided great support for the validation of our system at clinical sites. Without their precious support, it would not have been possible to conduct this research. Furthermore, I would like to express my sincere gratitude to Dr. Matthew Howard, Dr. Michael Brendan, and the people at the Robot Learning Lab of King's College London, who supported my research visit and provided meaningful advice to my research.

I also thank my fellow lab-mates for providing stimulating discussion and all the fun we had over the past six years. Special words of gratitude also go to Dr. Ayanori Yorozu and Dr. Hirotaka Iijima, who always had words of encouragement and who helped me take on my research.

Last, but not least, I would like to thank my parents for supporting me spiritually throughout the writing of this thesis as well as in my life.

February 2021

Ryo Eguchi

Contents

1 Introduction **1**

1.1 Background 1

1.2 Overview of Motion Sensing Systems 2

1.2.1 Kinetic Motion Sensing Systems 2

1.2.2 Kinematic Motion Sensing Systems 3

1.2.3 Spatial Motion Sensing Systems 4

1.3 Problem Definition 4

1.3.1 Problems in Estimation of GRF Using Instrumented Insole 5

1.3.2 Problems in Estimation of Joint Angle Using Stretch Sensor 5

1.3.3 Problems in Leg Tracking Using LRS 6

1.4 Major Contributions 6

1.4.1 Data-efficient Learning for User-specific Model Acquisition 6

1.4.2 Multiple Model Learning for Adaptive Estimation 7

1.5 Dissertation Outline 7

2 Force Plate-free Learning for Estimation of Vertical Ground Reaction Force Using Instrumented Insole **11**

2.1 Chapter Overview 11

2.2 Force Plate-free Learning 11

2.2.1 Hardware 11

2.2.2 Learning Flow 12

2.3 Evaluation of Force Plate-free Learning 16

2.3.1 Experiment A: Validation for Healthy Young Adults 16

2.3.2 Experiment B: Validation for Elderly and Patients with Gait Disorders . 20

2.3.3 Discussion 23

2.4 Conclusion 26

3 One-step Learning for Estimation of Vertical Ground Reaction Force Using Instrumented Insole **27**

3.1 Chapter Overview 27

3.2 One-step Learning . . . 27
3.2.1 Hardware . . . 27
3.2.2 Learning Flow . . . 28
3.3 Evaluation of One-step Learning . . . 33
3.3.1 Study Procedure . . . 33
3.3.2 Acquisition of Datasets for Learning and Evaluation . . . 33
3.3.3 Evaluation of Probabilistic Data Augmentation . . . 34
3.3.4 Evaluation of GPR . . . 38
3.3.5 Discussion . . . 39
3.4 Conclusion . . . 42

4 Shift-adaptive Estimation of Joint Angle Using Instrumented Brace with Two Stretch Sensors 43

4.1 Chapter Overview . . . 43
4.2 Shift-adaptive Estimation of Knee Joint Angle . . . 43
4.2.1 Instrumented Knee Brace with Two Stretch Sensors . . . 43
4.2.2 Learning of User-specific GMMs from Multiple Brace Shifts . . . 45
4.2.3 Shift-adaptive Estimation . . . 46
4.3 Evaluation of Shift-adaptive Estimation . . . 47
4.3.1 Experimental Setup . . . 47
4.3.2 Generation of Virtual Knee Joint Marker . . . 48
4.3.3 Study Procedure . . . 49
4.3.4 Data Analysis . . . 50
4.3.5 Results . . . 52
4.3.6 Discussion . . . 52
4.4 Conclusion . . . 55

5 Learning-based Occlusion Compensation for Leg Tracking Based on Fusion of Laser Range Sensor and Instrumented Insoles 56

5.1 Chapter Overview . . . 56
5.2 Learning-based Occlusion Compensation for Leg Tracking . . . 56
5.2.1 Sensor Configuration . . . 56
5.2.2 Pre-measurement Using Two LRSs without Occlusion . . . 57

5.2.3 Learning of Trajectory–Direction Relationship Using GMMs 63
5.2.4 GMM-based Occlusion Compensation 65
5.3 Evaluation of Learning-based Occlusion Compensation 68
5.3.1 Study Procedure 68
5.3.2 Data Analysis 69
5.3.3 Results 70
5.3.4 Discussion 75
5.4 Conclusion 75

6 Conclusion **77**
6.1 Summary of Contributions 77
6.1.1 Theoretical Contributions 77
6.1.2 Practical Contributions 79
6.2 Future Work 79
6.2.1 Validation for Patients with Severe Musculoskeletal Disease 79
6.2.2 Robustness for Different Conditions of Fabric and Clothes 80
6.2.3 Extension to Three-dimensional Motion Sensing 80

Nomenclature

Variables

g	Gravitational acceleration	$\mathrm{m/s^2}$
m	Body mass	kg
$N_\mathrm{L}, N_\mathrm{R}$	Number of time steps since last start of swing phase	
$\bar{\boldsymbol{M}}_{\mathrm{r/i}}$	Relative markers positions to their center at reference/interpolation frame	
$\bar{\boldsymbol{P}}_\mathrm{i}$	Relative interpolated marker positions to their center at interpolation frame	
β_l	Probability of each component l of Gaussian mixture models	
$\boldsymbol{\mu}_\mathrm{da}$	Actual measurements of instrumented insole and Wii Balance Board during one walking step	N
$\boldsymbol{\Sigma}_\mathrm{da}$	Variability of measurements of instrumented insole and Wii Balance Board between walking steps	N
$\boldsymbol{C}_\mathrm{i}$	Covariance matrix of relative markers positions between reference and interpolation frames	
$\boldsymbol{D}$	Matrix of dataset	N
$\boldsymbol{d}$	Vector of dataset	N
$\boldsymbol{\beta}$	Coefficient vector of basis function	
$\boldsymbol{\mu}_l$	Mean vector of component l of Gaussian mixture model	
$\boldsymbol{\Sigma}_l$	Covariance matrix of component l of Gaussian mixture model	
$\boldsymbol{A}$	State transition matrix	
$\boldsymbol{a}_k^f$	Acceleration vectors of leg f at time step k	$\mathrm{m/s^2}$
$\boldsymbol{B}$	Driving matrix	
$\boldsymbol{B}_\mathrm{u}$	Input matrix	
$\boldsymbol{C}$	Observation matrix	
$\boldsymbol{c}$	Capacitance of stretch sensors	pF
$\boldsymbol{d}'$	Transformed dataset into unified coordinate system	
$\boldsymbol{f}_\mathrm{s}$	Sensor forces of instrumented insole	N
$\boldsymbol{F}_\mathrm{s}^\mathrm{s}$	Matrix of measured forces of instrumented insole during SLS	N
$\boldsymbol{F}_\mathrm{s}^\mathrm{we}$	Matrix of measured forces of instrumented insole during entire stance of walking	N

$\boldsymbol{F}_{\mathrm{s}}^{\mathrm{wm}}$	Matrix of measured forces of instrumented insole during mid-stance of walking	N
$\boldsymbol{h}$	Constant basis function	
$\boldsymbol{K}_k^f$	Kalman gain of leg f at time step k	
$\boldsymbol{p}'$	Leg position transformed into unified coordinate system	m
$\boldsymbol{P}_{k-1/k-1}^f$	*A posteriori* covariance matrix of leg f at time step $k-1$	
$\boldsymbol{P}_{k/k-1}^f$	*A priori* covariance matrix of leg f at time step k	
$\boldsymbol{P}_{k/k}^f$	*A posteriori* covariance matrix of leg f at time step k	
$\boldsymbol{p}_k^f$	Position of leg f at time step k	m
$\boldsymbol{Q}$	Covariance matrix of system noise sequence	$(\mathrm{m/s^2})^2$
$\boldsymbol{R}$	Covariance of measurement noise sequence	$(\mathrm{m})^2$
$\boldsymbol{USV}$	Matrices of singular value decomposition	
$\boldsymbol{u}_k^f$	Input vector of leg f at time step k	$\mathrm{m/s^2}$
$\boldsymbol{v}_k^f$	Velocity of leg f at time step k	m/s
$\boldsymbol{w}$	Measurement noise	m
$\boldsymbol{w}_{\mathrm{s}}$	Coefficient weight vector for sensor forces of instrumented insole	
$\boldsymbol{x}_k^f$	State vector at time step k	
$\boldsymbol{y}_k^f$	Observation vector of leg f at time step k	m
Δt	Sampling time	ms
$\hat{\Sigma}_{\theta\theta,l}$	Variance of joint angle estimated by component l of Gaussian mixture model	$\mathrm{deg^2}$
$\hat{\Sigma}_{\theta\theta}$	Variance of estimated joint angle	$\mathrm{deg^2}$
$\hat{\Sigma}_{\theta'_v\theta'_v}$	Variance of traveling direction	$\mathrm{rad^2}$
$\hat{\theta}$	Estimated joint angle	deg
$\hat{\theta}_l$	Expected value of joint angle estimated by component l of Gaussian mixture model	deg
$\hat{\boldsymbol{x}}_k^f$	*A posteriori* state estimate of leg f at time step k	
$\hat{\boldsymbol{x}}_{k-1/k-1}^f$	*A posteriori* state estimate of leg f at time step $k-1$	
$\hat{\boldsymbol{x}}_{k/k-1}^f$	*A priori* state estimate of leg f at time step k	
$\hat{\boldsymbol{y}}_{k/k-1}^f$	Predicted position of leg f	m

$\hat{\theta}_v$	Estimated traveling direction in sensor coordinate system	rad
$\hat{\theta}'_v$	Estimated traveling direction in unified coordinate system	rad
λ	Threshold of gating	
π_l	Prior probability of component l of Gaussian mixture model	
σ_f	Signal standard deviation	
σ_l	Characteristic length scale	
SE_bp	Standard error of linear approximation to relationship between upper bound of peak vertical ground reaction force and stance duration	
SE_bt	Standard error of linear approximation to relationship between lower bound of trough vertical ground reaction force and stance duration	
θ_r	Rotation angle of transformation matrix from sensor to unified coordinate system	rad
θ_ub	Upper bound of estimated joint angle for identification of maximum likelihood Gaussian mixture model	deg
θ	Joint angle	deg
θ'	Joint angle scaled to [0, 1]	
θ'_v	Traveling direction transformed into unified coordinate system	rad
b	Sign variable of Kabsch algorithm	
c_l	Capacitance of lower stretch sensor	pF
c'_l	Capacitance of lower stretch sensor scaled to [0, 1]	
c_u	Capacitance of upper stretch sensor	pF
c'_u	Capacitance of upper stretch sensor scaled to [0, 1]	
$c_{a,b}$	Cost of global nearest neighbor algorithm for a-th and b-th observations	
$d^f_{2,j}$	Mahalanobis distance evaluating relation between prediction of leg f and j-th observation on XY-axis considering only measurement noise	
$d^f_{3,j}$	Mahalanobis distance evaluating relation between prediction of leg f and j-th observation on XY-axis and traveling direction	
$d_{f,j}$	Mahalanobis distance between leg f and j-th observation	
f	Side of leg (L,R)	
f_wb	Measurement of Wii Balance Board	N
f_bp	Upper bound of peak vertical ground reaction force	N

f_{bt}	Lower bound of trough vertical ground reaction force	N
f_{est}	Vertical ground reaction force estimated by instrumented insole using learned model	N
f_{fp}	Ground truth of vertical ground reaction force obtained from force plate	N
g_k^f	Average norm of acceleration vectors of leg f at time step k	$\mathrm{m/s^2}$
J_k	Number of total observations	
k	Discrete time step	
k_{i}	Interpolation frame	
k_{r}	Reference frame	
L	Number of components of Gaussian mixture model	
l	Index of component of Gaussian mixture model	
m_{gm}	Index of Gaussian mixture model	
$n^{\ddot{x}_k}, n^{\ddot{y}_k}$	Acceleration disturbances of leg f time step k	$\mathrm{m/s^2}$
n_{da}	Number of virtual walking steps generated in data augmentation	
n_{st}	Number of measured walking steps for learning	
N_{t}	Size of test dataset	
N_{ALL}	Total number of time steps	
n_{gm}	Number of learned Gaussian mixture models	
n_{s}	Number of force sensors of instrumented insole	
$N_{\mathrm{s}}^{\mathrm{s}}$	Size of data obtained from instrumented insole during SLS	
$N_{\mathrm{s}}^{\mathrm{we}}$	Size of data obtained from instrumented insole during entire stance of walking	
$N_{\mathrm{s}}^{\mathrm{wm}}$	Size of data obtained from instrumented insole during mid-stance of walking	
P_{G}	Probability extracted from χ^2 distribution	
p_{g}	Gait phase	
r	Euclidean distance	
$r_{\mathrm{C/ST}}$	Rate of steps with occlusion compensation in successful tracking steps	%
$r_{\mathrm{ST/ALL}}$	Rate of successful tracking steps	%
s	Summed number of sensor measurements	
T	Time window	
t_{s}	Stance duration during walking	ms

w_{l}	Leg width of target person	m
$\boldsymbol{\gamma}$	Unconstrained parameterization vector	
$\boldsymbol{M}_{\mathrm{r/i}}$	Markers positions at reference/interpolation frame	
$\boldsymbol{O}_{\mathrm{r/i}}$	Center of markers positions at reference/interpolation frame	
$\boldsymbol{P}_{\mathrm{i}}$	Interpolated marker positions at interpolation frame	
$\boldsymbol{R}_{\mathrm{i}}$	Rotation matrix from reference to interpolation frame	
$\boldsymbol{y}_k^j$	j-th observation at time step k	m
$\boldsymbol{S}_k^f$	Innovation covariance matrix of leg f at time step k	
σ^2	Noise variance	
$\widehat{\dot{x}}_{k-1}^f, \widehat{\dot{y}}_{k-1}^f$	Velocity of leg f at time step $k-1$ changed by estimated traveling direction	$\mathrm{m/s^2}$

Functions

$\boldsymbol{K}(\cdot,\cdot)$	Covariance function of Gaussian process regression
$f_{\mathrm{l}}(\cdot)$	Latent variable of Gaussian process regression
$k(\cdot,\cdot)$	Kernel function of Gaussian process regression
$p(\cdot)$	Probability density function

Chapter 1

Introduction

1.1 Background

In recent years, human motion sensing technologies have attracted increasing attention in the fields of medicine and healthcare. This has been driven by electronic device advancements, such as enhanced miniaturization, high-speed signal processing, and cost-effectiveness. These technologies quantify kinetic, kinematic, and spatial motion parameters [e.g., the ground reaction force (GRF), joint angle, and step length/width calculated from leg positions, as shown in Figure 1.1]. These parameters facilitate the early detection and treatment of progressive musculoskeletal diseases [e.g., knee osteoarthritis (OA)], which are difficult to assess by visual and X-ray inspections alone.

For example, patients with mild to moderate knee OA [Kellgren–Lawrence (KL) grades 1 and 2] exhibit push-off vertical GRF (vGRF) and total impulse during the stance phase of walking that are 18% and 12% smaller than those of asymptomatic counterparts, respectively [1]. These patients also exhibit reductions of 6.9°, 14.5°, and 200 mm in their swing-phase maximum knee flexion angle [2], range of motion [2], and step length [1] during walking, respectively. In addition, patients with severe OA (KL grades 3 and 4) exhibit further reductions of 15.4°, 12.1–16.1°, and 230 mm in their swing-phase knee flexion angle [3], range of motion [2, 3], and step length [3], respectively, compared with moderate OA patients.

This dissertation focuses on sensing systems to quantify the motion parameters of patients that have mild to moderate progressive musculoskeletal disease but do not exhibit extreme movement disorders. The systems require to estimate and track human motion using wearable/fixed sensors, which are accessible and suitable for use in small clinics and healthcare centers. In accordance with the previous studies [1–3], this dissertation sets the sensing accuracy criteria to 12% for the vGRF, 6.9° for the knee flexion angle, and 100 mm for the leg position when

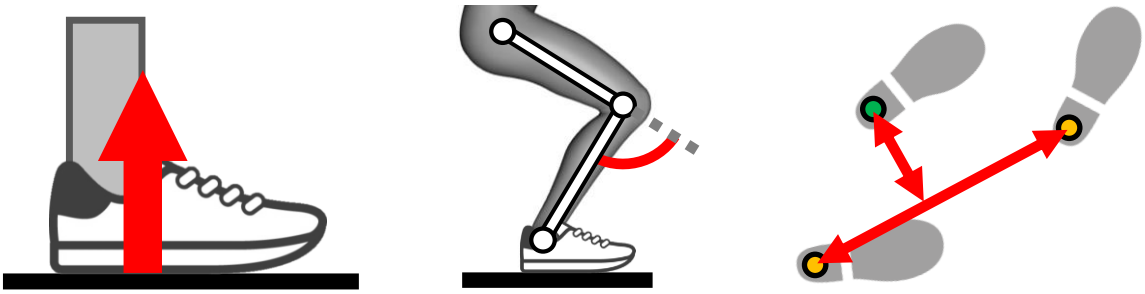

(a) (b) (c)

Figure 1.1. Motion parameters focused on this dissertation. (a) Vertical ground reaction force, (b) knee joint angle, and (c) step length and width calculated from leg positions.

calculating step length.

1.2 Overview of Motion Sensing Systems

1.2.1 Kinetic Motion Sensing Systems

Force plates are the gold standard for measuring GRF because of their high accuracy. However, they are often cost-prohibitive for use in small clinics. In addition, their fixed installation does not support measurement during continuous walking for long distances and leads the patients to target the plates causing unnatural walking.

As an alternative to force plates, various wearable systems measuring/estimating GRF during long-range walking have been proposed, for example, inertial measurement units [4–8], mobile force plates [9,10], and force sensing insoles [11,12]. In particular, the insole-type sensors do not affect natural walking and exhibit advantages in terms of evaluating pathological gaits, through measurement of stance duration, the center of pressure (COP), and GRF on each foot. Some of these devices have already been commercially available [e.g., Pedar (Novel, Munich, DE) and F-Scan (Tekscan, South Boston, US)]. They measure plantar pressure, which approximately matches vertical ground reaction force (vGRF) [11,12], and can estimate shear forces and joint torques through an inverse dynamics-based optimization using vGRF, COP, and kinematic information [13–16]. However, the full cost of these commercial devices remains prohibitive for widespread use at clinical sites.

Accordingly, previous studies have developed various in-shoe measurement systems using a small number of low-cost force sensing resistors (FSRs) [17–21]. In addition, some groups estimated GRF from these sensors or local plantar pressure measurements by representing their relation using machine learning techniques (e.g., linear [22–25] and nonlinear regressions [26–29]), with root mean square errors (RMSEs) under 10%. Note that learning a model to estimate GRF

from insoles should be performed as subject-specific owing to individual differences in the sizes and shapes of the foot.

1.2.2 Kinematic Motion Sensing Systems

Infrared motion capture cameras with retroreflective markers are typically employed for accurate kinematic motion analysis. However, their fixed installation limits the measurement range.

Meanwhile, IMUs integrating accelerometers, gyroscopes, and magnetometers have recently achieved remarkable development as wearable motion-sensing technologies [30]. The system reconstructs human motion using the orientations of IMUs attached to the body segments. To estimate the sensor orientation, a strap-down-integration of the angular rates is typically employed and its drift is eliminated using the gravitational acceleration and heading determined from magnetometer measurements if available. Although numerous fusion algorithms have been proposed, elimination of long-term drift and compensation for magnetic disturbances inevitable in a living environment still have attracted interest from researchers [31]. In addition, IMUs are typically made of rigid components and must be tightly attached to the body because the motion reconstruction is based on fixed sensor-to-segment frames and linked rigid-body modeling. The restraints these introduce restrict their long-term wearability in daily life.

As alternatives to IMUs, it has been proposed to use wearable sensors that directly measure changes in the joint angles, such as electrogoniometers (rotational potentiometers) [32,33], fiber-optic sensors [34–37], flex sensors [38–40], and stretchable strain sensors [41–47]. In particular, the stretch sensor, which transduces a mechanical deformation (sensor strain) to resistive or capacitive change, can (i) comply with fabric stretch and capture motion, (ii) avoid mechanical damage to the sensor, (iii) maintain user comfort when incorporated into garments (e.g., gloves [43], knee/ankle braces [44], or soft sensing suits [41, 46, 47]).

To estimate joint motions from such sensors, previous studies have modeled relationships between the sensor strains and motion parameters (e.g., joint angles or positions) via supervised/semi-supervised learning. For example, Nakamoto et al. [43] constructed a glove instrumented with a stretch sensor, whose capacitance was proportional to the square of the stretch length. They applied a linear least squares technique and estimated the wrist joint angle from the sensor capacitance with an RMSE less than 3°. Totaro et al. [44] integrated three/five capacitive sensors into commercial knee/ankle braces. They combined sensor outputs using third, fourth, and fifth-order polynomials and estimated joint angles (knee flexion/extension, ankle dorsi/plantar flexion, adduction/abduction, and rotation) with an RMSE less than 4°.

1.2.3 Spatial Motion Sensing Systems

In achieving the continuous tracking of the absolute positions of legs in the measurement space, fixed sensors still retain an advantage over wearable sensors such as IMUs, which are prone to drift errors. Although motion capture cameras are the gold standard for spatial sensing, they are not always accessible at clinical sites, owing to their cost, scale, and portability, as well as the complexity of their operations (e.g., camera calibration and pasting markers to appropriate positions).

In contrast, robotic vision technologies, (e.g., sonar sensors [48–51], RGB-Depth sensors [52–56], and laser range sensors (LRSs) [57–72]) have recently been employed for human detection and tracking. In particular, LRSs can obtain highly accurate two-dimensional distance data over wide ranges and can detect/track both legs during walking when installed at shin height (100–300 mm from the floor). To detect leg positions from scanned distance data, previous works have applied specific geometrical shapes [57, 58, 62–66, 72] or supervised learning techniques [59, 61, 67–70].

To track both legs while simultaneously maintaining their left/right distinction, numerous groups have combined motion prediction based on human walking models using linear/unscented Kalman filters [58,65,66,71] or particle filters [64,67] and data association techniques (e.g., global nearest neighbor (GNN) [58, 64, 66] or joint probabilistic data association [67] algorithms). For example, Yorozu et al. [66] tracked a timed up and go test that included rapid turning, by using the Kalman filtering considering gait phase and a GNN-based data association. They also applied Catmull–Rom spline-based interpolations to leg occlusions (i.e., where one leg is hidden from the sensor by the other). The errors of the tracked leg trajectories were approximately 50 mm when verified against motion capture cameras. Meanwhile, when walking on circular paths (useful for assessing fall risks [73, 74]), occlusion occurs continuously in several sampling steps and produces false tracking. To address this, several groups have proposed combinations of an LRS and RGB-Depth camera [58,64] or IMU [63] to obtain the walking direction or spline-based trajectory interpolation after occlusion [66, 72].

1.3 Problem Definition

To estimate and track human motions using wearable/fixed sensors, the system must model the user-specific relationships between the sensor measurements and the motion parameters or complex nonlinear motion dynamics. However, existing learning approaches decrease estimation accuracy through overfitting when the diversity and size of the dataset are constrained by device resources and the feasibility of user motion. In addition, the single model cannot adapt to

changes in the sensor–motion relationship because of the sensing conditions and the complicated motions that cannot be represented by a specific model. To address these issues, data-efficient learning using small datasets and limited sensor resources (i.e., without highly accurate devices) are required to generate motion estimation models. Moreover, multiple models must be trained according to the measurement condition, and adaptive estimation through selecting an adequate model therefrom must be established to handle the changes in sensor–motion relationships and complicated dynamic motions. Examples of these problems in measurement/estimation systems for kinetic, kinematic, and spatial motion parameters are described below.

1.3.1 Problems in Estimation of GRF Using Instrumented Insole

To estimate GRF from a small number of force sensors or local plantar pressure measurements, previous studies have proposed to learn a user-specific model, representing relationships between insole measurements and GRF, using linear/nonlinear regressions [22–24,26–29]. However, these learning methods have two fundamental problems remaining in order to be used at clinical sites. First is that they rely on the use of highly accurate devices (e.g., force plates) unavailable in small clinics to obtain ground truth of GRF as a target value of learning. Second is that the learning requires measurements of multiple walking steps (e.g., 10–20 steps on the floor [23] or 60–120 s on an instrumented treadmill [27,29]) to prevent overfitting on small datasets, because foot contact conditions (e.g., force magnitude and plantar pressure distribution) vary between steps. However, the measurement of multiple steps prior to a clinical test induces fall risks and physically taxes elderly people and patients with musculoskeletal disease. In addition, an efficient learning procedure is desired in clinical assessments owing to consultation time limitations.

1.3.2 Problems in Estimation of Joint Angle Using Stretch Sensor

To estimate joint motions from stretch sensors incorporated into garments, previous studies have modeled the relationship between the sensor strains and motion parameters using supervised/semi-supervised learning techniques (e.g, linear/polynomial regressions [43, 44] or deep neural networks (DNN) [46, 47]). However, typically these only model a single relationship assuming the sensor to be located at a specific point on the body. Consequently, these approaches may exhibit reduced performance when the strain–parameter relationship varies due to shifting of the sensor with respect to the body, which is caused by long-term wearing or donning/doffing of garments. Especially in the knee brace, Brouwstein [75] reported that 15 min of exercise induces the brace shift of up to 11 mm, and Singer et al. [76] mentioned that individuals will likely stop their activity to adjust the brace position when it has shifted by more than 20 mm distally on the leg. Thus, the previous single model-based approaches may decrease

motion estimation accuracy when unnoticed brace shift occurs during long-term use.

1.3.3 Problems in Leg Tracking Using LRS

To track both legs during walking, previous studies have combined a state prediction using model-based Kalman/particle filters and data association techniques. However, when walking on circular paths, the position estimation accuracies decrease because continuous occlusion occurs over several sampling steps preventing observations from being obtained. This arises because human leg motions are highly nonlinear and difficult to model accurately [58, 77]. Accordingly, numerous groups have installed LRSs onto mobile robots that follow humans at relatively close distances (1–2 m) and tracked legs using models that consider horizontal rotation, angular velocity, and/or angular acceleration [58, 63, 67]. Meanwhile, a clinical assessment system must track legs across a wider range (3–5 m from the sensor) using an LRS fixed to the floor [65, 66]. However, the number of lasers irradiating the leg surface decreases as the distance from the sensor increases, because the laser spreads radially. This increases the position error and makes it difficult to accurately obtain the walking direction and angular velocity prior to occlusion, causing accuracy of motion prediction during occlusion to further deteriorate. To address this problem, sensor combination that measures walking direction have been proposed, however, unnatural wearable devices (e.g., IMUs mounted on the back [63]) can affect natural walking, and RGB cameras [58,64] are unsuitable for clinical use because of privacy protection regulations [78].

1.4 Major Contributions

This dissertation presents *biomechanics-driven stochastic learning* for human motion sensing systems, which achieves the data-efficient learning of motion estimation models from limited datasets and the adaptive estimation using multiple models. For data-efficient learning, training/constraint dataset acquisition or data augmentation, which are based on human biomechanics, and stochastic learning techniques enable learning of sophisticated models using a small dataset with constrained diversity while avoiding overfitting. For adaptive estimation, the learning of multiple stochastic models and biomechanics-based identification of the appropriate model therefrom allow changes in the sensor–motion relationship and complicated dynamic motions to be handled, which is difficult to achieve using a single model.

1.4.1 Data-efficient Learning for User-specific Model Acquisition

Chapters 2 and 3 present the data-efficient learning for generating motion estimation models from small datasets and limited sensor resources (i.e., without highly accurate devices). More

specifically, to estimate vGRF during walking using an insole instrumented with a small number of force sensors, constrained linear least squares regression and Gaussian process regression combined with a data augmentation—which utilize biomechanics (i.e., vGRF characteristics during single leg stance and/or walking)—learn sophisticated models while avoiding overfitting on limited datasets.

1.4.2 Multiple Model Learning for Adaptive Estimation

Chapters 4 and 5 describe the learning of multiple Gaussian mixture models (GMMs) and the adaptive estimation using the maximum likelihood (ML) model. These models handle changes in the relationships between the sensor measurements and the motion parameters or complex motion dynamics, which are difficult to represent with a single model. More specifically, to estimate joint angles using a brace instrumented with two stretch sensors, the system learns different strain–angle relationships at varying brace shift positions, which are induced by biomechanics (i.e., characteristics of the skin stretch around the joint). The ML model identified by referring to the relationship between the two sensor strains estimates the joint angle adaptively to the brace shift. In LRS-based leg tracking, the relationships between trajectories of the legs and their traveling directions during walking under different curvatures/directions are modeled in advance by GMMs. The system then estimates the direction and position of the hidden leg during occlusion using the ML GMM, which is identified from the joint probability of both legs' trajectories using biomechanics (i.e., interlimb coordination during one walking cycle).

1.5 Dissertation Outline

This section presents an outline of the dissertation. Figure 1.2 depicts the overall configuration. Chapter 1 describes the background and major contributions. Chapters 2–6 are summarized as follows.

Chapter 2: Force Plate-free Learning for Estimation of Vertical Ground Reaction Force Using Instrumented Insole

Chapter 2 presents *force plate-free learning* that estimates vGRF during walking using an insole instrumented with a small number of force sensors. This method uses limited data that consists of only the insole measurements and the user's body weight. The system learns a linear regression model between the insole measurements during a single leg stance (SLS) and the body weight by the least squares method, which is based on biomechanics that vGRF during the SLS approximately matches the body weight. In the regression, linear constraints for the upper/lower bounds based on the biomechanics that the magnitudes of peak/trough vGRFs and

stance durations during natural walking are linearly related are added to prevent overfitting.

Chapter 3: One-step Learning for Estimation of Vertical Ground Reaction Force Using Instrumented Insole

Chapter 3 presents data-efficient *one-step learning* for deriving insole-based vGRF estimation. It requires only one walking step to be performed, which is useful for users who struggle to perform SLS or multiple-step walking because of decreased motor abilities. The system probabilistically augments the actual insole measurements and vGRF obtained from a low-cost body scale for one step to a virtual dataset for multiple steps. This augmentation is based on the biomechanical assumption that the insole measurements and vGRF obtained from the scale vary between multiple walking steps owing to inconsistencies in walking behaviors. The system then learns a Gaussian process regression model that can avoid overfitting on small datasets.

Chapter 4: Shift-adaptive Estimation of Joint Angle Using Instrumented Brace with Two Stretch Sensors

Chapter 4 presents a *shift-adaptive estimation* to obtain the joint angle from a knee brace instrumented with two stretch sensors. This method involves learning multiple models and performing adaptive estimation to changes in the relationship between the sensor strains and the joint angle due to the brace shift. The system induces changes in the relationship between the strains of the two stretch sensors, which are placed above and below the patella hole of the brace, utilizing biomechanics that the skin strain is high in the patella area and rapidly decreases further from the joint. The relationship between the two sensor strains and the joint angle at varying brace shift positions is then learned using user-specific GMMs. In the estimation, an ML GMM (i.e., the brace shift position) is identified by referring to the relationship between the two sensor strains. The angle is then calculated adaptively to the brace shift using the ML GMM.

Chapter 5: Learning-based Occlusion Compensation for Leg Tracking Based on Fusion of Laser Range Sensor and Instrumented Insoles

Chapter 5 presents a *learning-based occlusion compensation* for leg position based upon the interlimb coordination for one walking cycle. This facilitates LRS-based tracking of complicated dynamic motions of both legs during walking on circular paths. The system measures straight walking and turning under different curvatures/directions in advance, and then learns the relationship between the trajectory and traveling direction of each leg during one cycle of each walking type, using user-specific GMMs. In the tracking, an ML GMM (i.e., the walking type) is identified using a joint probability of both legs' trajectories during the walking cycle,

in accordance with the biomechanics that both legs move in a coordinated manner. The ML GMM then estimates the traveling direction and position of the hidden leg during occlusion.

Chapter 6: Conclusion

Chapter 6 summarizes the findings obtained from the aforementioned investigations, presents conclusions, and suggests directions for future research.

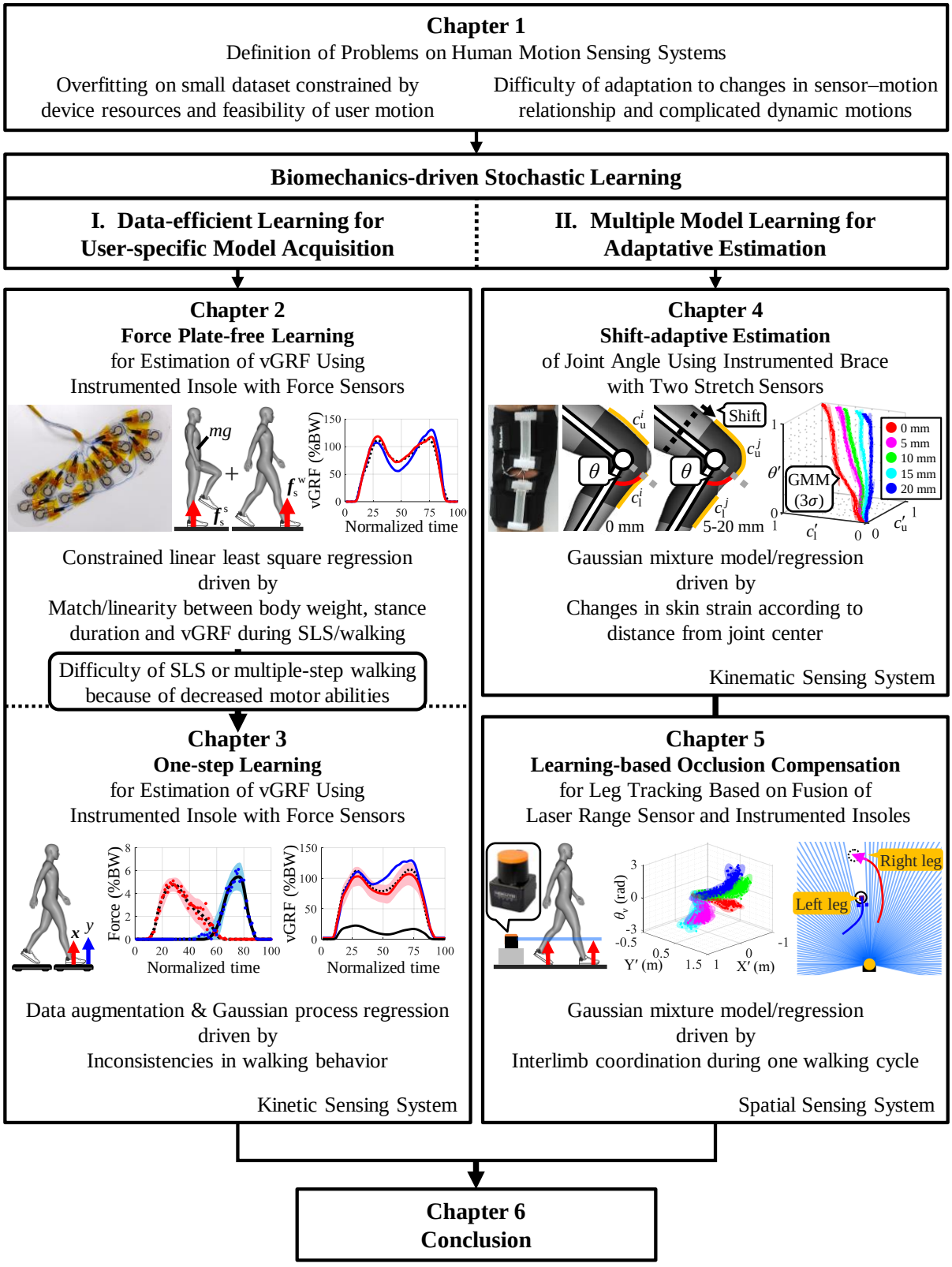

Figure 1.2. Configuration of this dissertation.

Chapter 2

Force Plate-free Learning for Estimation of Vertical Ground Reaction Force Using Instrumented Insole

2.1 Chapter Overview

This chapter presents *force plate-free learning* that estimates vGRF during walking using an insole instrumented with a small number of force sensors. This method uses limited data that consists of only the insole measurements and the user's body weight. The system learns a linear regression model between the insole measurements during SLS and the body weight by the least squares method, which is based on biomechanics that vGRF during the SLS approximately matches the body weight. In the regression, linear constraints for the upper/lower bounds based on the biomechanics that the magnitudes of peak/trough vGRFs and stance durations during natural walking are linearly related are added to prevent overfitting.

2.2 Force Plate-free Learning

2.2.1 Hardware

This study designed an insole instrumented with 15 force sensing resistors (FlexiForce Standard Model A301, Tekscan, South Boston, US), as shown in Figure 2.1(a). The sensors were fixed on an insole-shaped overhead projector (OHP) sheet using a polytetrafluoroethylene (PTFE) tape.

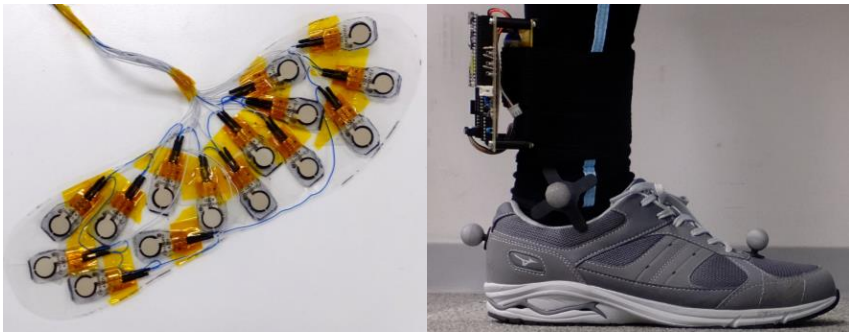

(a) (b)

Figure 2.1. (a) The insole was instrumented with 15 force sensors. (b) The electric circuit board was placed on the back of the user's lower leg.

Three sizes of the insole were developed corresponding to the differences in shoe sizes between users. The small size was men's size 6 (women's 6.5), the middle size was men's size 7 (women's 7.5), and the large size was men's size 9 (women's 9.5). The sensor positions were determined from [23] to cover a typical pressure distribution on the foot anatomical areas [79]. The sensor measures the force applied to the sensing area using an inversely proportional relationship with changes in resistance. All sensors were calibrated using a load cell (Press Force Sensor 9313AA2, Kistler, Winterthur, CH) prior to installation. The instrumented insoles were inserted into shoes (LD AROUND M, Mizuno, Tokyo, JP) according to correct sizes and were covered with an insole, which is a stainless-steel sheet of 0.45 mm thickness sandwiched by ethylene-vinyl acetate (EVA) copolymer sheets. In addition, a circuit board comprising a microcontroller, op-amps, analog-to-digital (A/D) converters, a microSD card, and a radio module was developed to record sensor measurements through a voltage divider with a buffer amplifier and synchronize the system with external devices. As shown in Figure 2.1(b), the board was fixed to the back of the user's lower leg and connected to the insole using a ribbon cable.

2.2.2 Learning Flow

To estimate vGRF during walking from the insole measurements, a linear least squares regression with constraints and a bound is used to learn a model. The flow of the force plate-free learning is shown in Figure 2.2.

(1) Measurement of SLS and Walking

First, SLS including standing on a heel and a toe, and natural walking are measured only by the insoles. SLS is used because vGRF during SLS approximately matches the body weight, which can be clearly defined as the output value of learning and easily obtained using a low-cost body

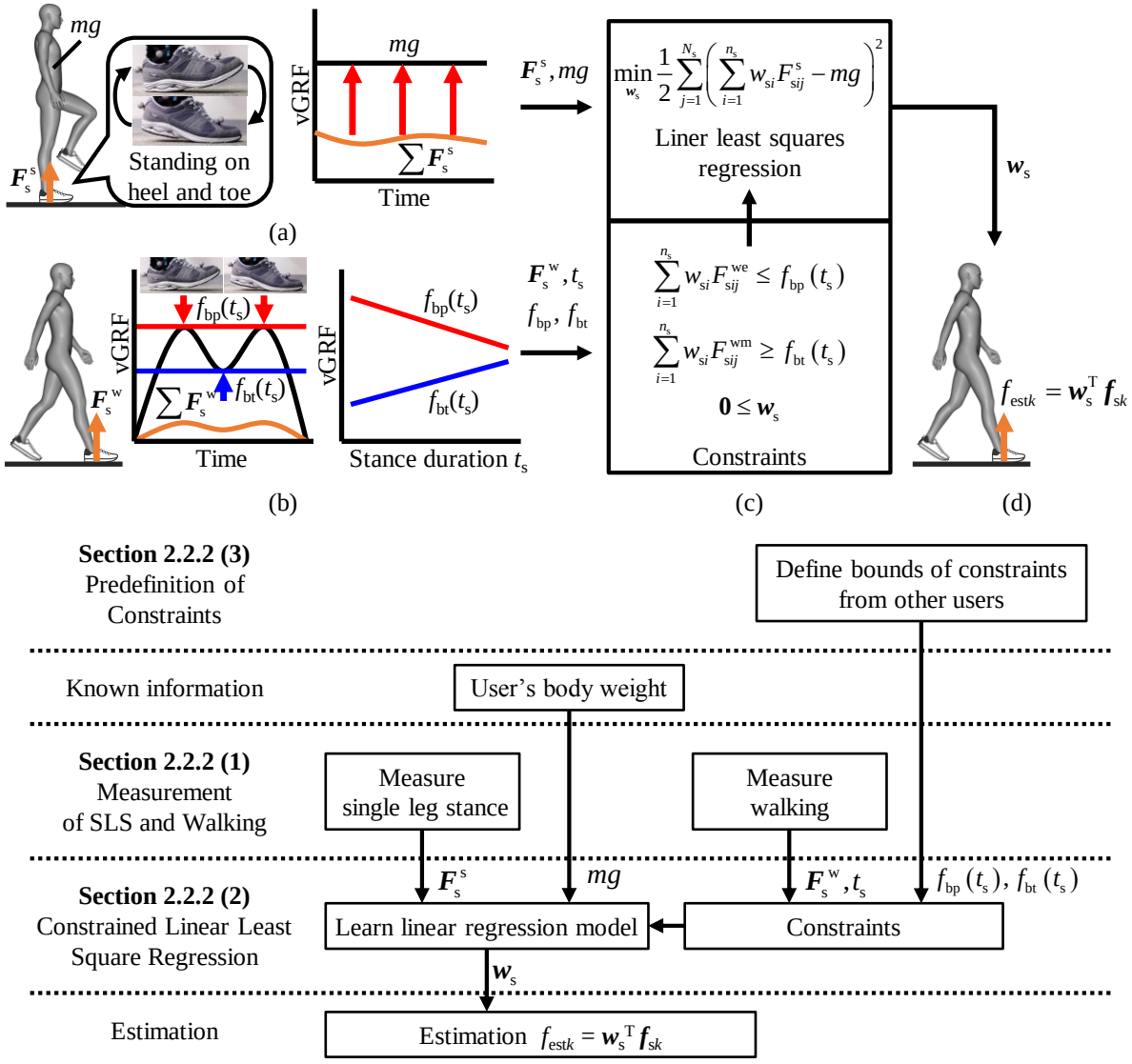

Figure 2.2. (Top) Flow of the insole-based estimation of vGRF using the force plate-free learning from SLS and natural walking. (a) SLS including standing on a heel and a toe is measured by only the insoles. (b) Natural walking is also measured by only the insoles. (c) A linear least squares regression fits the insole measurements during SLS to the body weight. This learns a model while avoiding overfitting using constraints that peak/trough vGRFs estimated during natural walking are of proper magnitude. (d) The insole estimates vGRF during walking using the learned model. (Bottom) Data flow of the force plate-free learning.

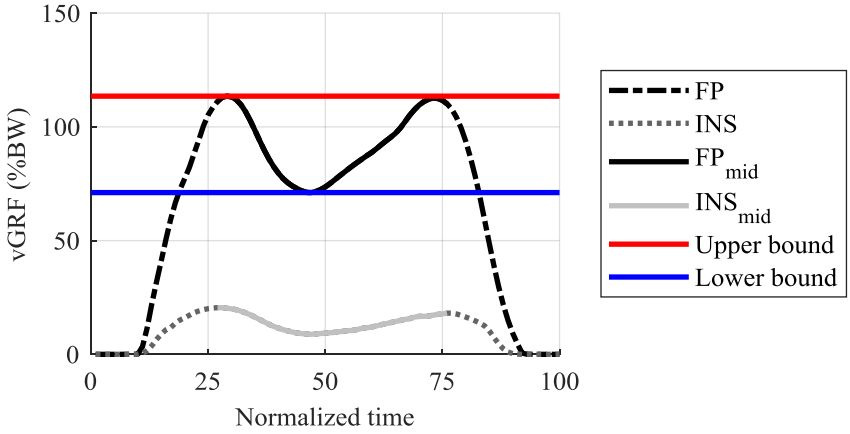

Figure 2.3. A vGRF measured using force plate (black line) and the total force of the insole sensors (gray line) during one walking step. Solid lines represent the forces in mid-stance between two peaks of the insole force. Red and blue lines indicate the upper/lower bounds to peak/trough vGRFs, respectively.

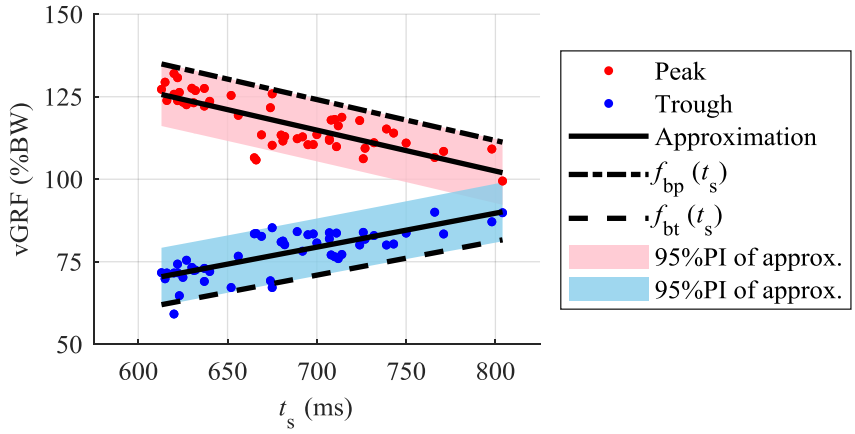

Figure 2.4. Relationships between peak/trough vGRFs (red/blue dots) and stance duration. Black lines are linear approximations to each dataset. The dash-dot (f_{bp}) and dot lines (f_{bt}) are upper/lower bounds defined as linear functions of stance duration (t_s), considering 95% prediction intervals of the approximations.

scale. The standing on the heel and toe aims to reenact foot contacts close to walking.

(2) Constrained Linear Least Squares Regression

To learn the estimation model, a linear least squares regression then fits the insole measurements during SLS to the body weight. To prevent overfitting to the constant value (i.e., the body weight), constraints are added to the regression so that peak/trough vGRFs estimated from the insole measurements during natural walking are of proper magnitude. These constraints are based on the biomechanics that vGRF typically has two peaks corresponding to weight acceptance and push-off impulse in a stance [80], whose magnitude changes proportionally to walking velocity that ranges from 0.75 to 2.00 m/s [81] and up to 3.5 m/s [82]. Referring to

these features, this study defines the upper bound for estimated peak vGRFs as a linear function of stance duration as an alternative to walking velocity. This is because stance duration can be directly captured by the insole [83, 84] unlike walking velocity, and its percentage to the gait cycle linearly reduces as the velocity increases [85, 86]. In addition, as shown in Figure 2.3, a lower bound for the trough vGRF in mid-stance is added as the constraint to enhance the estimation performance. This constraint is also defined as a linear function of stance duration.

From the above, the regression form is given as follows:

$$\min_{\boldsymbol{w}_\mathrm{s}} \frac{1}{2} \sum_{j=1}^{N_\mathrm{s}^\mathrm{s}} \left(\sum_{i=1}^{n_\mathrm{s}} w_{\mathrm{s}i} F_{\mathrm{s}ij}^\mathrm{s} - mg \right)^2 \tag{2.1}$$

$$\text{subject to} \begin{cases} \sum_{i=1}^{n_\mathrm{s}} w_{\mathrm{s}i} F_{\mathrm{s}ij}^\mathrm{we} \leq f_\mathrm{bp}(t_\mathrm{s}) \quad (j = 1, \ldots, N_\mathrm{s}^\mathrm{we}) \\ \sum_{i=1}^{n_\mathrm{s}} w_{\mathrm{s}i} F_{\mathrm{s}ij}^\mathrm{wm} \geq f_\mathrm{bt}(t_\mathrm{s}) \quad (j = 1, \ldots, N_\mathrm{s}^\mathrm{wm}) \\ \mathbf{0} \leq \boldsymbol{w}_\mathrm{s} \end{cases} \tag{2.2}$$

where $\boldsymbol{w}_\mathrm{s}$ is the coefficient weight vector for the insole forces, N_s^s is a size of the force data obtained from the insole during SLS, n_s is the number of insole sensors, $\boldsymbol{F}_\mathrm{s}^\mathrm{s}$ is the input data matrix obtained from the insole during SLS, and mg is the user's body weight. In the linear inequality constraints, $\boldsymbol{F}_\mathrm{s}^\mathrm{we}$ and $\boldsymbol{F}_\mathrm{s}^\mathrm{wm}$ are the data matrices obtained from the insole in entire stance phase and mid-stance during walking, respectively. The mid-stance is defined as a period between the two peaks of the insole total force, as depicted in Figure 2.3. Sizes of these data matrices are N_s^we and N_s^wm. The bounds f_bp and f_bt, which are defined as functions of stance duration t_s, are the upper and lower bounds for peak/trough vGRFs, respectively. The lower bound of the weight vector was set to $\mathbf{0}$ to ensure that the weights remain positive because a negative force would be unnatural. This study assumed that the effect of horizontal GRF during SLS and walking was negligible in accordance with the report that the total plantar pressure measured by a commercial insole-type sensor approximately matched the vGRF (the difference was less than 4% [12]).

(3) Predefinition of Constraints

To define the upper/lower bounds of constraints as linear functions of stance duration, five healthy adults with no gait abnormalities (age: 22.8 ± 1.2 years, height: 1.70 ± 0.05 m, body mass: 60.5 ± 4.5 kg) were recruited for a pre-experiment. The experiment was approved by Keio University Research Ethics Committee (reference number 30–68). All participants provided informed consent. The participants were asked to perform straight walking, and vGRF in their fourth and fifth steps were measured using force plates (Kistler, Winterthur, CH) at 1000 Hz.

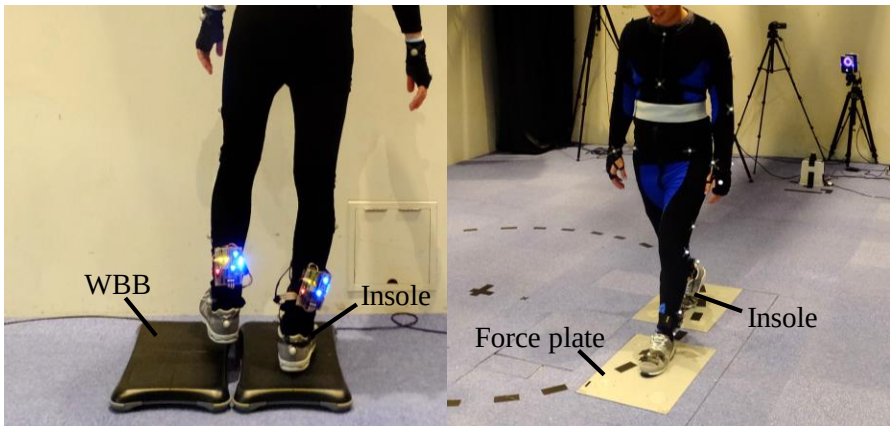

Figure 2.5. Task executions and walkway of the experiment A. (a) Participants performed SLS on the WBB. (b) Participants walked straight at a self-selected pace with their fourth and fifth steps contacting the force plates.

The task was repeated 10 times and the data from 20 steps were collected per participant. Stance duration was obtained as a period from heel contact to toe-off, which were detected from the threshold of 50 N. The peak/trough vGRFs and stance duration in each step were collected from all participants and then applied linear approximations, as shown in Figure 2.4.

The stance durations were ranged from 613 to 804 ms, and coefficients of determination for the approximations were $R^2 = 0.633$ and $R^2 = 0.586$ for the peaks and trough, respectively. The results show that the vGRF decreased at the peaks and increased at the trough as the stance duration extended. From these results, the upper/lower bounds for the peak/trough vGRFs were defined as linear functions of the stance duration considering 95% prediction intervals using standard errors of the approximations ($\mathrm{SE}_{\mathrm{bp/bt}}$), as follows:

$$f_{\mathrm{bp}}(t_{\mathrm{s}}) = (-1.24t_{\mathrm{s}} + 2.11 + 1.96\mathrm{SE}_{\mathrm{bp}})mg \tag{2.3}$$

$$f_{\mathrm{bt}}(t_{\mathrm{s}}) = (1.03t_{\mathrm{s}} - 0.01 - 1.96\mathrm{SE}_{\mathrm{bt}})mg \tag{2.4}$$

2.3 Evaluation of Force Plate-free Learning

2.3.1 Experiment A: Validation for Healthy Young Adults

(1) Study Procedure

Four healthy males (age: 25.3 ± 2.9 years, height: 1.71 ± 0.07 m, body mass: 68.6 ± 7.3 kg, shoe size: L) differed from the subjects in the pre-experiment participated in this experiment. All participants provided informed consent. The participants wore shoes with the instrumented

insoles inserted. Their task executions were measured using the insoles, two scales (the Nintendo Wii Balance Board, Nintendo, Kyoto, JP), and two force plates (Kistler, Winterthur, CH). The Nintendo Wii Balance Board (WBB) is a portable scale and can measure vGRF with an error of 3% [87]. The WBBs were used to obtain vGRF during SLS. The measurements were collected from the insoles and the WBBs at 100 Hz and the force plates at 1000 Hz. All devices were synchronized via voltage inputs and radio communications.

As shown in Figure 2.5, the participants were asked to perform the following tasks:

A. As shown in Figure 2.5(a), the participants performed SLS on the WBB and alternatively stood on their heel and toe three times at their selected pace. During the SLS, participants were allowed to put their hands on the wall to maintain balance. This task was repeated five times.

B. The participants walked straight and naturally eight steps on the floor at their selected pace. This task was repeated four times.

C. As shown in Figure 2.5(b), the participants walked straight and naturally at a self-selected pace with their fourth and fifth steps contacting the force plates. This task was repeated 10 times.

Data analysis was executed using MATLAB (MathWorks, Natick, MA, US). The measurements of all devices for the right foot were used for the analysis. Noise and data loss of the insole measurements were handled using a fifth-order one-dimensional median filter. In task A, the participants' body weight was measured during standing on both feet before starting SLS. The SLS phases were obtained as the duration from the lifting to the landing of the foot opposite to the supporting side, and the first and last 1 s were excluded as transient states. In task B, the fourth walking step was used for the constraints of learning. Using these data, MATLAB Optimization Toolbox solved the constrained linear least squares problem, as described in (2.1), to learn a regression model based on the interior-point method.

To evaluate the learned model, a dataset of the insole and force plate in a stance phase and 100 ms before/after that during walking was obtained from 10 trials in task C. Measurements of the force plate were resampled at 100 Hz according to the insole. The accuracies of vGRF estimated by the learned model were evaluated by comparison with ground truth obtained from the force plate, using a normalized root mean squared error (nRMSE), which is calculated as a

Table 2.1. Mean (± SD) of vGRF during SLS for five trials and overall.

ID	Trial 1 (%BW)	Trial 2 (%BW)	Trial 3 (%BW)	Trial 4 (%BW)	Trial 5 (%BW)	Overall (%BW)
A	99.2 (2.2)	99.5 (2.7)	99.2 (2.3)	99.1 (2.9)	99.1 (2.9)	99.2 (2.6)
B	99.1 (2.0)	99.3 (1.7)	99.4 (2.5)	99.3 (2.6)	99.4 (2.2)	99.3 (2.2)
C	99.9 (3.3)	99.8 (3.4)	100.1 (5.0)	100.1 (3.6)	100.1 (3.6)	100.0 (3.8)
D	99.8 (4.5)	99.5 (3.8)	99.8 (4.2)	99.8 (4.1)	99.8 (3.9)	99.8 (4.1)

Table 2.2. Stance duration and accuracy of estimated vGRF during walking.

ID	SD_{LEARN} (ms)	SD_{EVAL} (ms)	nRMSE (%BW)					
			W/O	UP_{CONST}	UP_{LIN}	$UL_{LIN}^{90\%}$	$UL_{LIN}^{95\%}$	$UL_{LIN}^{99\%}$
A	665 (10)	647 (12)	13.8 (2.4)	13.4 (2.6)	14.7 (2.6)	8.7 (1.5)	8.4 (2.3)	9.3 (2.4)
B	670 (8)	652 (11)	24.2 (13.3)	17.9 (4.4)	15.1 (3.1)	9.2 (3.5)	9.8 (2.6)	10.6 (3.2)
C	670 (18)	644 (11)	21.4 (5.8)	14.7 (1.9)	11.6 (2.0)	10.6 (4.4)	10.4 (3.6)	10.9 (2.5)
D	705 (21)	678 (12)	13.3 (1.7)	13.3 (1.7)	12.3 (1.6)	7.1 (1.1)	6.6 (0.9)	7.2 (1.3)
Overall	678 (18)	655 (16)	18.2 (8.7)	14.8 (3.4)	13.4 (4.2)	8.9 (3.2)	8.8 (2.9)	9.5 (2.8)
p						0.011	0.016	0.028
$1-\beta$						0.445	0.516	0.398

percentage of the body weight (%BW) as follows:

$$\text{nRMSE (\%BW)} = \frac{100\sqrt{\frac{1}{N_\text{t}}\sum_{k=1}^{N_\text{t}}\left(f_{\text{fp}k}-f_{\text{est}k}\right)^2}}{mg} \tag{2.5}$$

$$f_{\text{est}k} = \boldsymbol{w}_\text{s}^\top \boldsymbol{f}_{\text{s}k} \tag{2.6}$$

where k is the time step, N_t is a size of the test dataset in stance phases and 100 ms before/after them, $f_{\text{fp}k}$ is the ground truth obtained from the force plate at k, and $f_{\text{est}k}$ is vGRF estimated by the learned model from the insole forces $\boldsymbol{f}_{\text{s}k}$ at the same time step.

To evaluate the effect of prediction intervals of $f_\text{bp}(t_\text{s})$ and $f_\text{bt}(t_\text{s})$ on the proposed method ($UL_{LIN}^{95\%}$), the nRMSE of the methods using linear constraints with 90/99% prediction intervals ($UL_{LIN}^{90\%}$/$UL_{LIN}^{99\%}$) were also calculated. In addition, comparative methods, using linear regressions with no constraints (W/O), a fixed upper constraint with 140% of the body weight (UP_{CONST}) [88,89], and an upper constraint as a linear function of stance duration (UP_{LIN}), were examined using the same datasets with the proposed method. Their estimation accuracies were also evaluated using nRMSEs for 10 trials in task C. The accuracy criteria were set to 12% since its validity for capturing pathological gaits has been reported. This includes mild to moderate knee osteoarthritis (OA), which decreases push-off forces by 18% and total impulse by 12% compared with healthy controls [1].

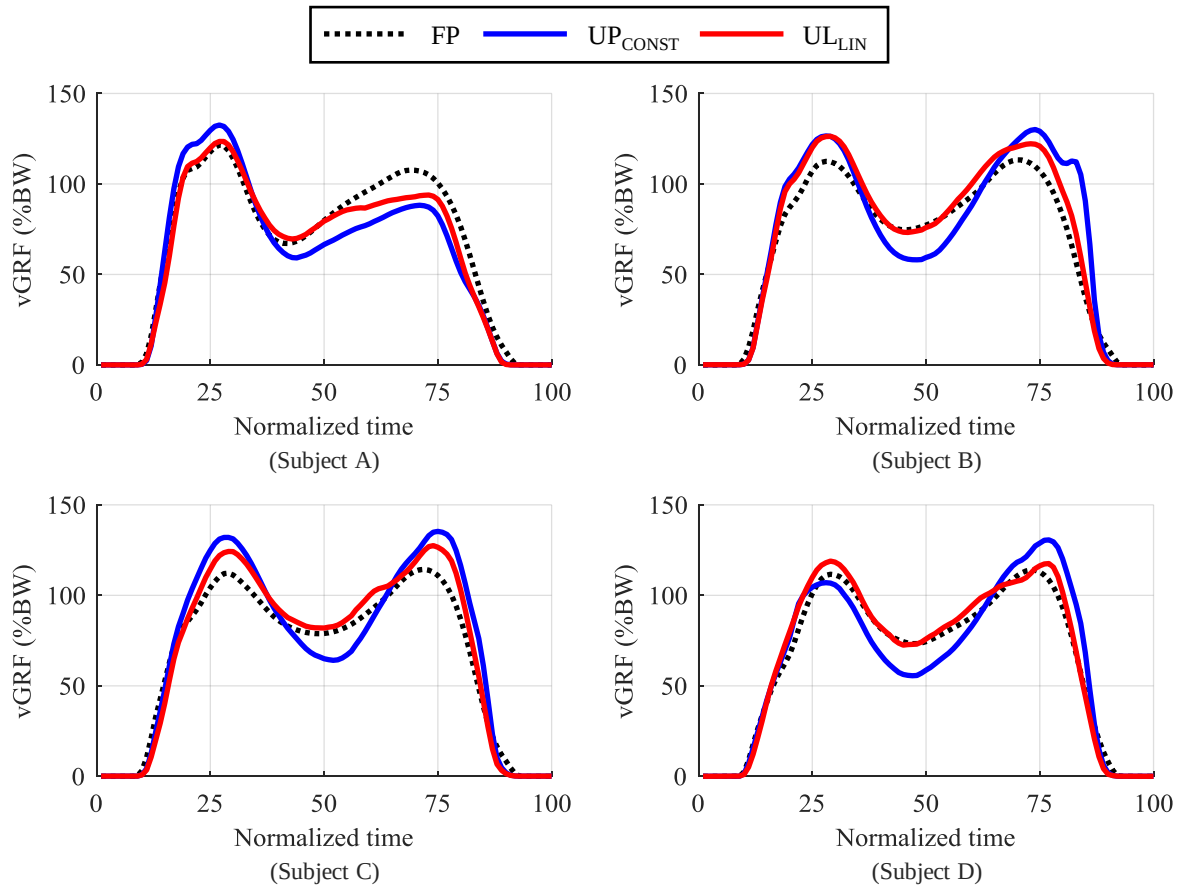

Figure 2.6. vGRF lines estimated by the comparative (UP_{CONST}) and proposed (UL_{LIN}) methods and ground truth obtained from the force plate (FP) in a stance are illustrated for each participant. Each plot is the mean of 10 trials in task C.

(2) Results

The results of vGRF during SLS measured by the WBB are listed in Table 2.1. The mean (± SD: standard deviation) is given for each participant and overall. The results show that the mean vGRF during SLS exceeded 99% of the body weight for all participants, which indicates that every participant did not extremely lean against the wall.

Stance duration of walking steps for constraints (SD_{LEARN}) and evaluation (SD_{EVAL}), and nRMSE of the comparative (W/O, UP_{CONST}, UP_{LIN}) and proposed ($UL_{LIN}^{90\%}$, $UL_{LIN}^{99\%}$, $UL_{LIN}^{95\%}$) methods are listed in Table 2.2. The mean (± SD) is given for each participant and overall.

The results show that stance durations for both constraints and evaluation for all participants were within the range obtained from the pre-experiment (600–800 ms). The mean differences between stance duration for the constraints and evaluation were under 30 ms. The proposed methods ($UL_{LIN}^{90\%}$, $UL_{LIN}^{99\%}$, $UL_{LIN}^{95\%}$) enhanced the estimation accuracies for overall participants when compared to the other methods. The accuracies of the proposed methods were evaluated

(a) (b) (c)

Figure 2.7. Task executions and walkway of experiment B. (a, b) Participants performed SLS on the WBB. (c) The participants walked straight at a self-selected pace with their fourth and fifth steps contacting the WBB.

by one-sample t-tests. The null hypothesis was that the accuracy of these methods came from a population with a mean of 12%, and was against the alternative that the mean was under 12%. As listed in Table 2.2, the tests for all methods rejected the null hypothesis at the 5% significance level and supported the alternate hypothesis ($p < 0.05$). Meanwhile, the powers of the tests ($1 - \beta$) were less than 0.8 and did not provide strong statistical support for the results.

The vGRF lines estimated by the comparative and proposed methods ($\mathrm{UP}_{\mathrm{CONST}}, \mathrm{UL}_{\mathrm{LIN}}^{95\%}$) are presented in Figure 2.6. Each line is the mean of all trials in task C. These results show that the proposed method using upper/lower bounds as linear functions of stance duration improved estimation accuracies at the two peaks and the trough when compared with the method using the fixed upper bound.

2.3.2 Experiment B: Validation for Elderly and Patients with Gait Disorders

(1) Study Procedure

To examine the validity of the force plate-free learning for the elderly and patients with mild gait disorders, the experiment recruiting 13 elder women was conducted at a local healthcare center. All participants provided informed consent prior to the experiments. The participants wore shoes with the instrumented insoles (S size). Their task executions were measured using the insoles and the two WBBs at 100 Hz. Both devices were synchronized via radio communications. The participants were asked to perform the following tasks, as shown in Figure 2.7:

A. As shown in Figure 2.7(a,b), the participants performed SLS on the WBB and alternatively stood on their heel and toe three times at their selected pace. During the SLS, participants

Table 2.3. Characteristics of participants in experiment B.

ID	Age (years)	Height (m)	Weight (kg)	BMI	KL	NRS	HV angle (°)
E	70	1.52	55.2	23.9	1	0	1
F	77	1.58	57.2	22.9	2	3	10
G	76	1.52	51.8	22.4	0	0	9
H	67	1.58	48.1	19.3	1	2	5
I	73	1.53	45.0	19.2	1	3	15
J	75	1.53	38.8	16.6	0	0	11
K	74	1.53	52.1	22.3	1	0	6
L	83	1.48	54.0	24.7	2	0	9
M	77	1.53	48.0	20.5	1	0	5
N	82	1.40	41.7	21.3	2	1	5
O	79	1.52	52.1	22.6	2	3	0
P	79	1.50	42.8	19.0	2	0	19
Q	69	1.57	49.9	20.2	1	0	34
Overall	75.5 (4.8)	1.52 (0.05)	49.0 (5.6)	21.1 (2.2)	1.2 (0.7)	0.9 (1.3)	9.9 (8.9)

were allowed to put their hands on the wall to maintain balance.

B. The participants walked straight and naturally eight steps on the floor at their selected pace.

C. As shown in Figure 2.7(c), the participants walked straight and naturally at a self-selected pace with their fourth and fifth steps contacting the WBBs. The participants walked on the WBB with a small step up owing to a little height (53.2 mm).

Measurements of both devices for the right foot were used for data analysis using MATLAB. In task A, the participant's body weight and data during SLS were obtained through the same process as experiment A. In task B, two steps after the fifth step of the straight walking were used for constraints of the proposed learning method. Using these data, the linear least squares regression (2.1) was executed to learn a model to estimate vGRF during walking.

To evaluate the models, a dataset of the insole and the WBB in a stance phase and 100 ms before/after that was obtained from the 10 trials in task C. The estimation accuracy of vGRF was evaluated by comparison with ground truth obtained from the WBB using nRMSE.

(2) Results

Characteristics of the participants are described in Table 2.3. As the indexes related to gait disorders, the KL grade for classifying the severity of knee OA, numerical rating scale (NRS) reflecting the intensity of knee pain, and hallux valgus (HV) angle are given for the right foot of each participant. The participants included five patients with knee OA (KL grade 2), five participants with knee pain symptoms in the last month (NRS ≥ 1), and three patients with an HV (HV angle $\geq 15°$).

Table 2.4. vGRF during SLS, stance duration, and accuracy of estimated vGRF during walking.

ID	$vGRF_{SLS}$(%BW)	SD_{LEARN}(ms)	SD_{EVAL}(ms)	SD_{DIF}(ms)	nRMSE (%BW)
E	100.2 (4.7)	650 (14)	810	160 (14)	7.6
F	93.8 (8.3)	620 (0)	800	180 (0)	8.4
G	95.7 (6.3)	700 (28)	870	170 (28)	7.7
H	91.0 (6.0)	780 (14)	1160	380 (14)	12.4
I	94.7 (12.1)	650 (14)	820	170 (14)	6.1
J	91.0 (8.4)	660 (0)	1010	350 (0)	17.1
K	88.0 (5.5)	690 (0)	800	110 (0)	13.2
L	95.0 (6.7)	695 (35)	930	235 (35)	14.9
M	89.6 (7.0)	675 (7)	760	85 (7)	18.4
N	95.8 (6.7)	670 (14)	1260	590 (14)	18.1
O	96.2 (3.1)	690 (42)	730	40 (42)	5.3
P	95.0 (5.9)	625 (7)	710	85 (7)	6.9
Q	93.6 (5.6)	655 (7)	730	75 (7)	15.4
Overall	93.8 (3.2)	674 (41)	876 (171)	202 (155)	11.6 (4.8)

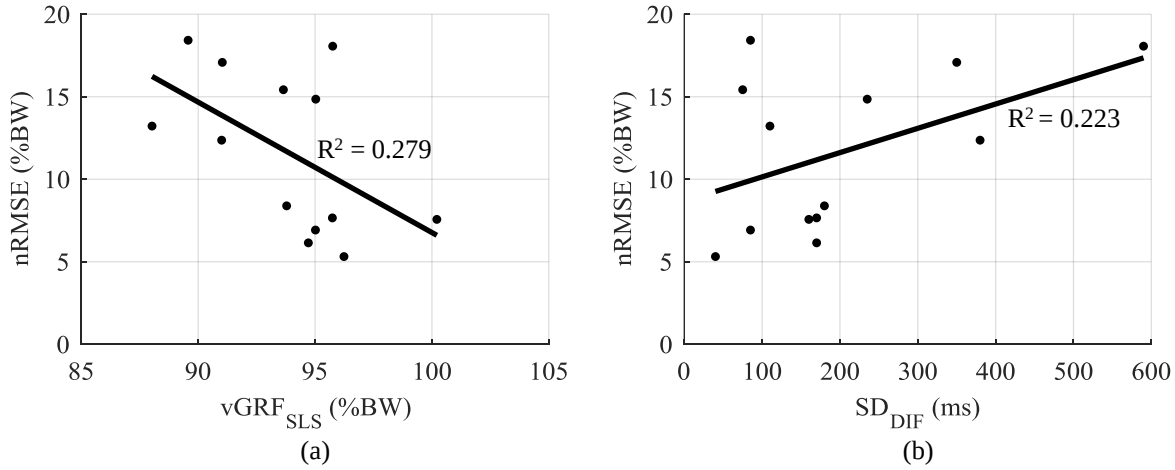

Figure 2.8. (a) The relationship between mean vGRF during SLS ($vGRF_{SLS}$) and estimation accuracy of vGRF during walking (nRMSE). (b) The relationship between difference in stance duration for the constraints and evaluations (SD_{DIF}) and nRMSE. Both relationships indicate moderate correlations.

The mean (± SD) of the vGRF during SLS measured by the WBB in task A ($vGRF_{SLS}$), stance durations for the constraints (SD_{LEARN}) and evaluation (SD_{EVAL}), and accuracies of the vGRF estimated by the proposed method (nRMSE) are summarized in Table 2.4. SD_{LEARN} was within the range obtained from the pre-experiment (600–800 ms) for all participants. Meanwhile, mean $vGRF_{SLS}$ was 93.8% of the body weight and SD_{EVAL} was 876 ms (200 ms longer than SD_{LEARN}), and the accuracy of estimated vGRF varied between participants (11.6% ± 4.8%).

Thus, this study investigated relationships between $vGRF_{SLS}$, the differences in stance durations between the constraints and evaluation ($SD_{DIF} = SD_{EVAL} - SD_{LEARN}$), and the estimation accuracy of vGRF. As shown in Figure 2.8, the estimation accuracy improved as $vGRF_{SLS}$ approached the body weight without leaning against the wall and SD_{DIF} became small. The

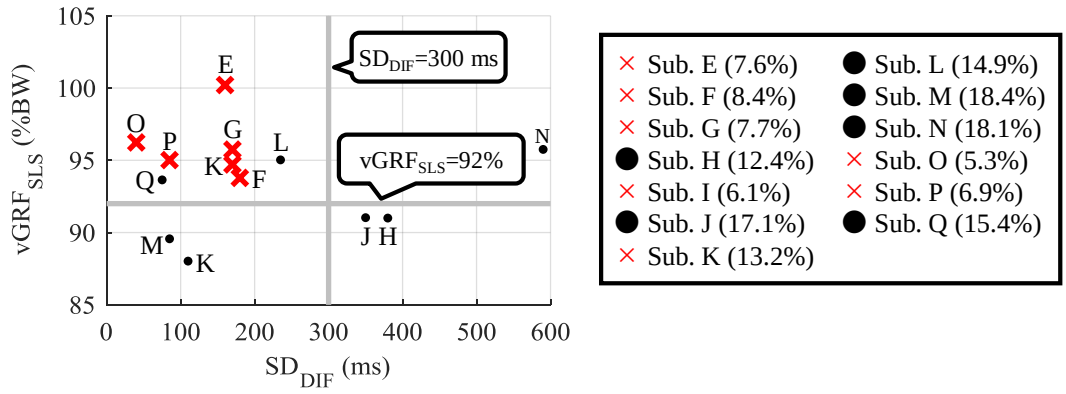

Figure 2.9. The relationship between mean vGRF during SLS ($vGRF_{SLS}$) and the difference between stance duration for the constraints and evaluations (SD_{DIF}). Red cross plots indicate participants with nRMSE under 12%. Gray lines represent cutoffs for $vGRF_{SLS}$ (dot line) and SD_{DIF} (dash-dot line), respectively.

relationships between mean $vGRF_{SLS}$ and SD_{DIF} for all participants are illustrated in Figure 2.9. Given these results, cutoffs for applicable conditions of the proposed method were defined as 92% of the body weight for $vGRF_{SLS}$ and 300 ms for SD_{DIF}. According to Table 2.3 and Figure 2.9, nine of the participants, including four patients with knee OA, three participants with knee pain symptoms in the last month, and three patients with an HV, were selected by these cutoffs. The nRMSEs for the selected participants were under 12% except for subject L with an HV (34°) and Q with knee OA (KL grade 2), and the mean (± SD) was 9.0% ± 3.9%. One-sample t-test rejected the null hypothesis that the accuracy of the proposed method came from a population with a mean of 12% at the 5% significance level ($p = 0.034$). Meanwhile, the power of the test ($1 - \beta$) was 0.618 and did not provide strong statistical support for the alternate hypothesis that the mean was under 12%. The vGRF lines estimated by the proposed method are presented for each participant in Figure 2.10.

2.3.3 Discussion

(1) General Discussion

In experiment A for healthy subjects, although the results did not provide strong statistical support ($1 - \beta < 0.8$), the proposed learning method ($UL_{LIN}^{95\%}$) and the methods with stricter/looser constraints ($UL_{LIN}^{90\%}$, $UL_{LIN}^{99\%}$) estimated vGRF with valid accuracy (under 12%, $p < 0.05$), which were enhanced when compared to all other methods. The results indicate that the proposed force plate-free learning is robust to the approximation error of the linear constraints and is valid for clinical assessment. In addition, Figure 2.6 shows that the accuracies of the estimated peak/trough vGRFs were improved when compared with the method using the fixed upper bound. These results indicate that the proposed method, which defines upper and lower bounds

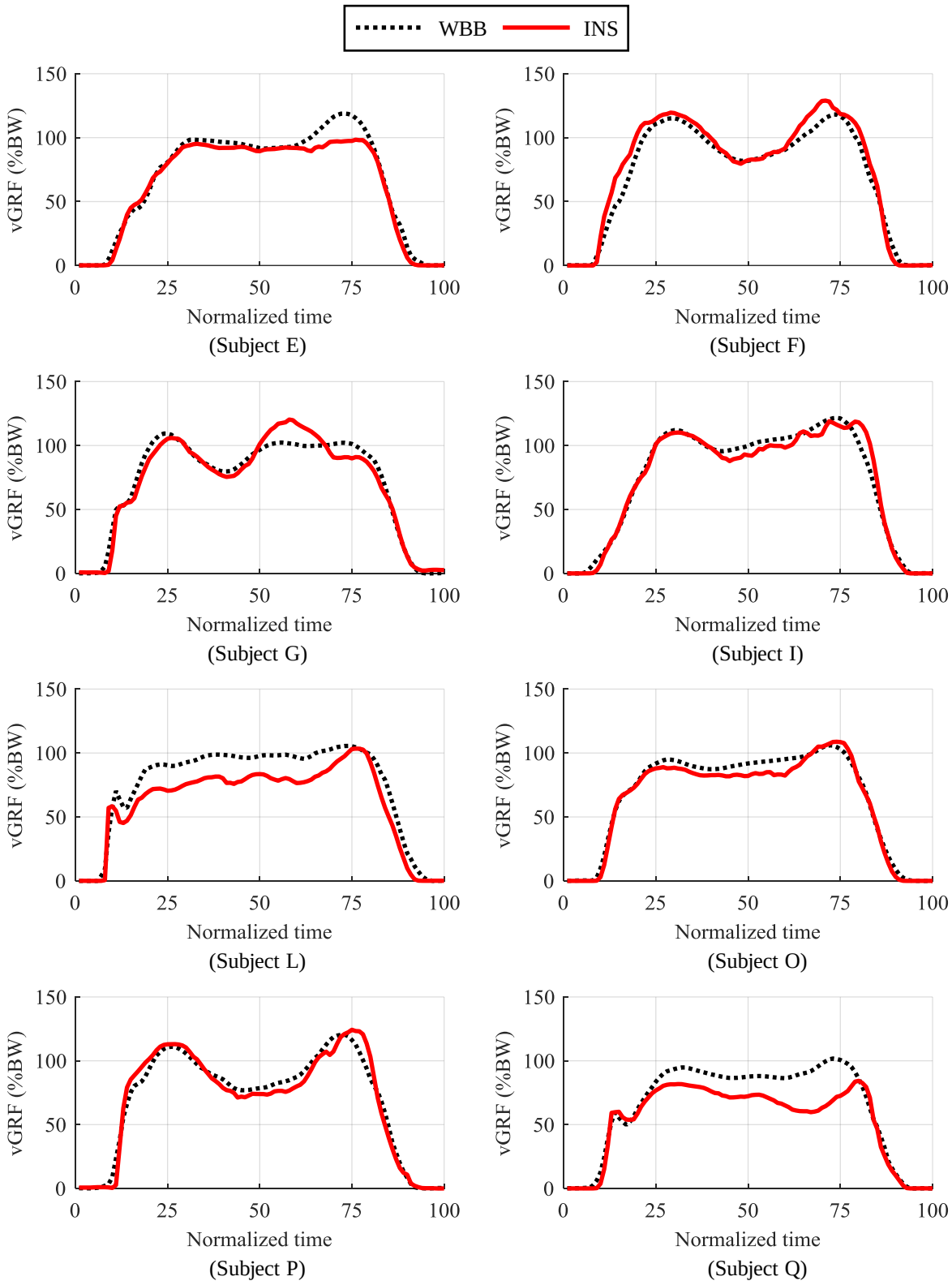

Figure 2.10. vGRF lines estimated from the insole (red) and ground truth obtained from the WBB (black dash) in a stance are illustrated for each participant.

of the constraints as linear functions of stance duration, can prevent overfitting to the limited dataset.

In experiment B for the elderly including patients with gait disorders, the mean vGRF during SLS was smaller (93.8%) than experiment A. Moreover, the mean difference between stance duration for the constraints and evaluations was longer than 200 ms, and the nRMSE varied between participants (11.6% ± 4.8%). Given these results, cutoffs in Figure 2.9 were provided and the mean nRMSE was 9.0% for the selected eight participants shown in Figure 2.10. Although the results did not provide strong statistical support ($1 - \beta = 0.618$), the accuracy overall was under 12% ($p = 0.034$).

From the above results, the validity of the force plate-free learning was verified in the following conditions:

A. vGRF during SLS needs to exceed 92% of the body weight without extreme leaning against a wall.

B. Stance duration for both the constraints and evaluation requires to be within a certain range, in which linear relationships between vGRF magnitudes at peak/trough and stance duration are verified (e.g., 600–800 ms in this study). In addition, the difference between the stance durations for the constraints and evaluation should be small (under 300 ms).

The key finding of this study is that the validity of the proposed learning method under the aforementioned conditions was verified for not only healthy adults but also the elderly and patients with various mild to moderate gait disorders, including knee OA, knee pain, and valgus hallux.

(2) Limitations

This study tested the proposed method for only four healthy young and nine older adults, which did not provide strong statistical support. Thus, the method needs to be tested for more people in future research. The system may have difficulty in adapting to patients with abnormal plantar pressure distribution. The user-specific model handles individual differences in foot size and pressure distribution to a certain extent by adjusting the coefficient weight for the sensors. However, estimation accuracy may decrease in some cases; for example, flat feet wherein pressure concentrates on the arch area where the sensors are not located on the insole. Thus, the robustness of the sensor locations should be investigated for various plantar pressure distribution. In addition, the validity of the proposed method was examined for walking on a relatively hard floor, which is widely used in small clinics. Therefore, the applicability of the system to softer floors such as carpets used at home needs to be examined in future work. In

addition, this study focused on assessing the natural walking of patients with mild to moderate musculoskeletal disease and did not consider the effect of asymmetrical upper body posture and specific upper limb motion on vGRF. A different learning method may need to be applied to patients with severe musculoskeletal disease presenting these postures or motions.

2.4 Conclusion

This chapter presented the force plate-free learning that estimates vGRF during walking using the insole instrumented with a small number of force sensors. This method uses limited data that consists of only the insole measurements and the user's body weight. The system learns a linear regression model between the insole measurements during SLS and the body weight by the least squares method, which is based on biomechanics that vGRF during the SLS approximately matches the body weight. In the regression, linear constraints for the upper/lower bounds based on the biomechanics that the magnitudes of peak/trough vGRFs and stance durations during natural walking are linearly related are added to prevent overfitting. Through the experiments, the proposed method showed a valid accuracy (a nRMSE under 12%) for healthy young and elderly adults with stance durations within a certain range (600–800 ms).

Chapter 3

One-step Learning for Estimation of Vertical Ground Reaction Force Using Instrumented Insole

3.1 Chapter Overview

This chapter presents data-efficient *one-step learning* for deriving insole-based vGRF estimation. It requires only one walking step to be performed, which is useful for users who struggle to perform SLS or multiple-step walking because of decreased motor abilities. The system probabilistically augments the actual insole measurements and vGRF obtained from a low-cost body scale for one step to a virtual dataset for multiple steps. This augmentation is based on the biomechanical assumption that the insole measurements and vGRF obtained from the scale vary between multiple walking steps owing to inconsistencies in walking behavior. The system then learns a Gaussian process regression model that can avoid overfitting on small datasets.

3.2 One-step Learning

3.2.1 Hardware

This study used the insole with 15 force sensors, as described in Chapter 2. To learn a model to estimate vGRF from the insole, the Nintendo Wii Balance Boards (WBBs) shown in Figure 3.1 were used as low-cost alternatives to force plates for obtaining vGRF during walking. The device can measure the vertical force applied to the usable surface using four strain gauge load cells (MinebeaMitsumi, Nagano, JP) located near each of four corners. Previous studies have

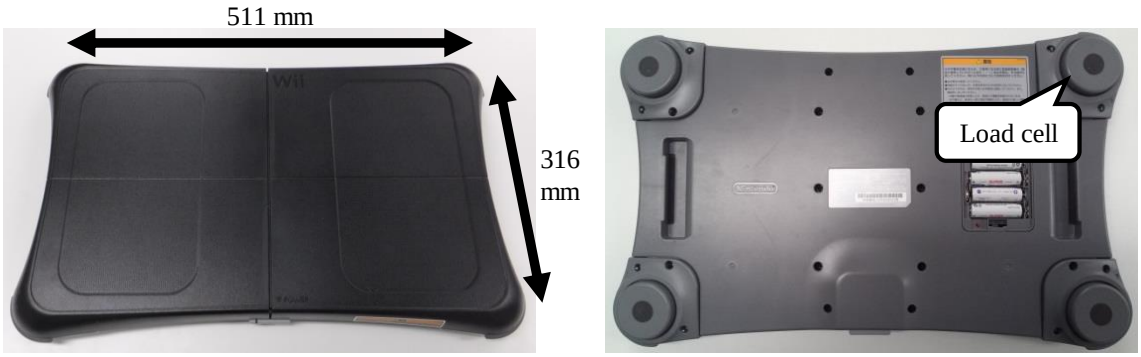

Figure 3.1. Appearance of the Nintendo Wii Balance Board (WBB): (a) usable surface, and (b) four load cells located near the four corners (bottom view).

used the WBB to assess postural instability [90–98] and measure weight-bearing asymmetry or vGRF during sit-to-stand (squat) [99,100], ski-jumping [101], and walking [87]. In this study, the WBBs were connected to a laptop computer through a Bluetooth connection and collected their measurements using custom C++ software. The obtained data were filtered using a moving average with a window size of 30 ms [87] because the measurements were corrupted by an inconsistent sample rate and a low signal-to-noise ratio [102].

3.2.2 Learning Flow

A model estimating vGRF from the insole is learned using measurements of the insole and the WBB during walking on the WBB. Although increasing the size of the dataset for learning could enhance the performance of the model, measuring many walking steps is often difficult at clinical sites because of the consultation time limitations and fall risks, and because it physically taxes elder people and patients with musculoskeletal disease. Meanwhile, the WBB has a measurement error, and the performance of the deterministic model (e.g., a linear regression model and neural networks) decreases owing to overfitting when using a dataset of a small number of walking steps. To overcome these problems, this study proposes data-efficient learning shown in Figure 3.2, which uses measurements of a minimum (just one) step, probabilistic data augmentation, and a GPR model.

(1) Probabilistic Data Augmentation

First, one walking step is measured by the insole and the WBB, and the dataset is time normalized to 100 equally spaced data points. Datasets for an arbitrary number of walking steps are then randomly generated at each sampling time point. This data augmentation is based on the biomechanical assumption that the insole measurements and vGRF obtained from the

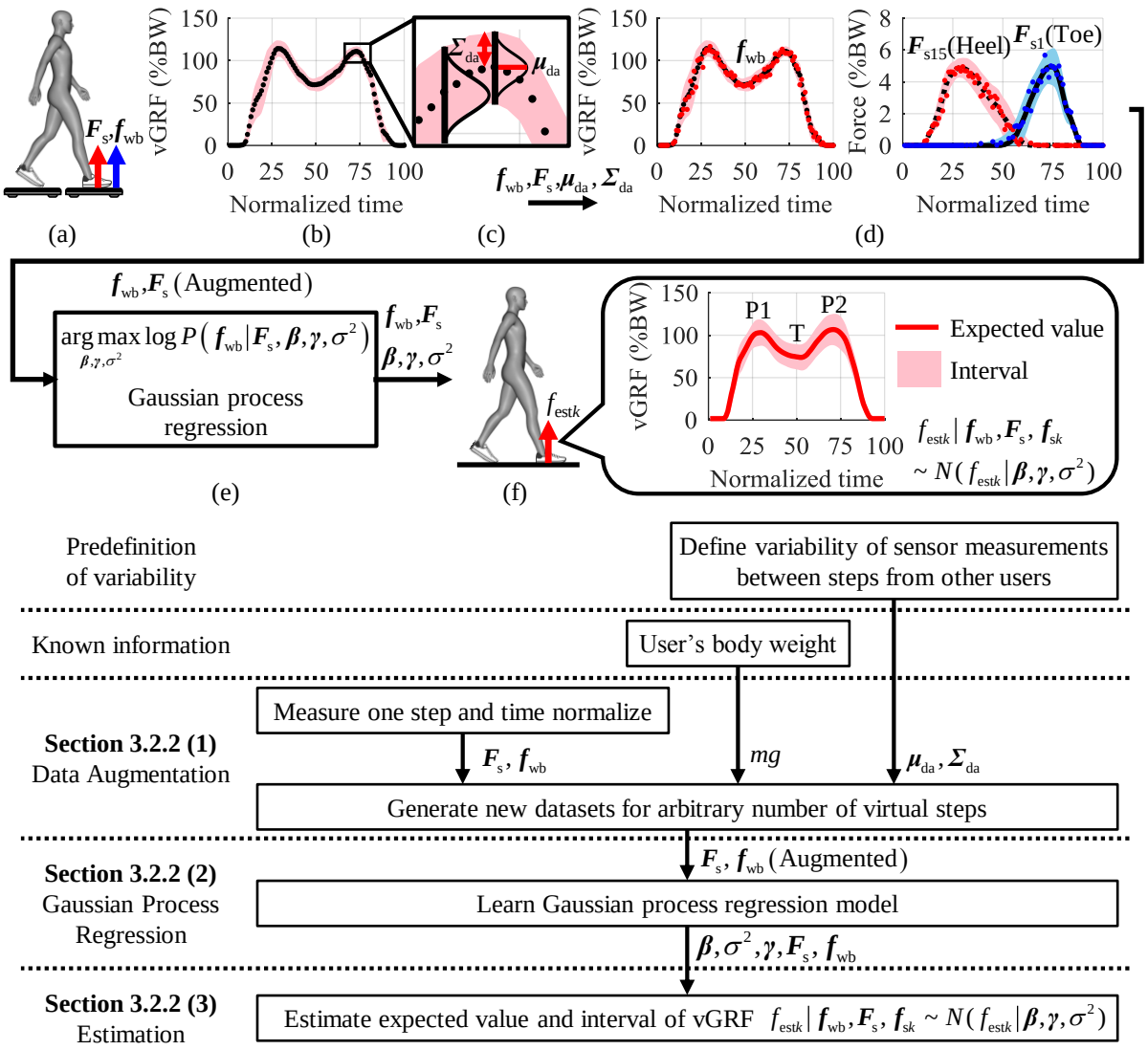

Figure 3.2. (Top) Flow of the one-step learning for the insole-based vGRF estimation during walking. (a) Measurements of the insole ($\boldsymbol{f}_{\mathrm{s}}$) and the WBB ($f_{\mathrm{wb}}$) are obtained from one walking step on the WBB. (b) The dataset is time normalized to 100 spaced equally data points. (c) Variability of measurements between steps is defined using a multivariate normal distribution. (d) Datasets for an arbitrary number of steps are randomly generated at each sampling time. (e) GPR model is learned using the augmented dataset. (f) vGRF during walking is estimated from insole measurements using the learned GPR model. The vGRF typically has two peaks (P1 and P2) and a trough (T) in a stance. (Bottom) Data flow of the one-step learning.

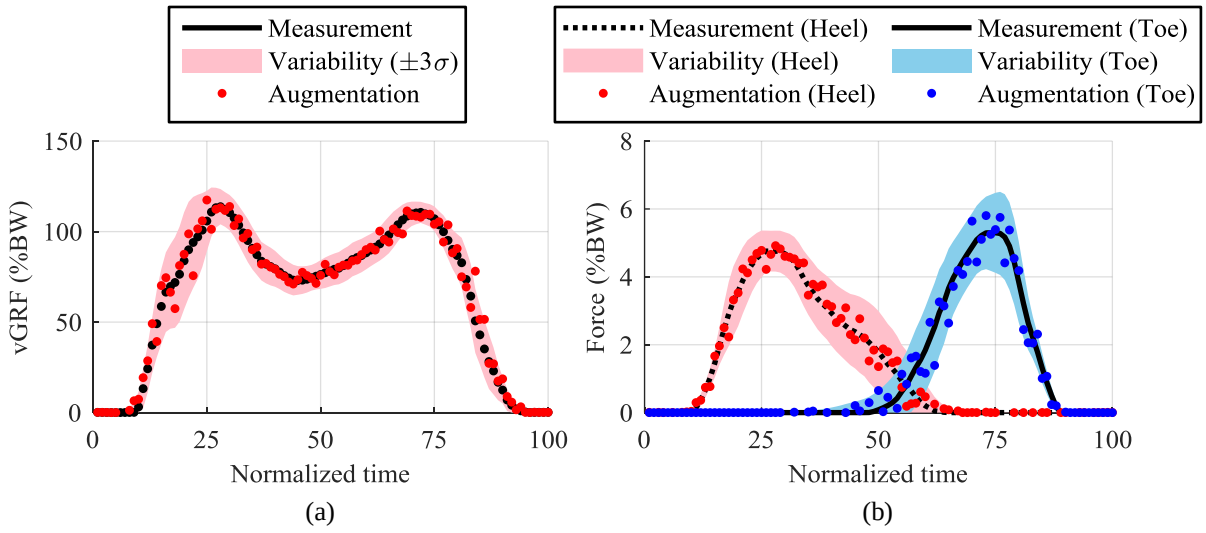

Figure 3.3. Examples of the probabilistic data augmentation. (a) Measurements in one walking step (black line) are augmented for virtual steps (red dots) using variability of vGRF measured by the WBB between steps (pink band). (b) The insole forces are augmented at the same sampling time points (red/blue dots).

WBB vary between multiple walking steps, owing to inconsistencies in walking behaviors. The variability is defined as a multivariate normal distribution with the probability density function as follows:

$$f(\boldsymbol{d}, \boldsymbol{\mu}_{\mathrm{da}}, \boldsymbol{\Sigma}_{\mathrm{da}}) = \frac{1}{(2\pi)^{\frac{s}{2}}} \frac{1}{|\boldsymbol{\Sigma}_{\mathrm{da}}|^{\frac{1}{2}}} \exp\left(-\frac{1}{2}(\boldsymbol{d} - \boldsymbol{\mu}_{\mathrm{da}})\boldsymbol{\Sigma}_{\mathrm{da}}{}^{-1}(\boldsymbol{d} - \boldsymbol{\mu}_{\mathrm{da}})'\right) \tag{3.1}$$

where $\boldsymbol{d}$ is the vector of dataset (insole measurements $\boldsymbol{f}_{\mathrm{s}}$ and outputs of the WBB f_{wb}), s is the summed number of these sensor measurements, the mean vector $\boldsymbol{\mu}_{\mathrm{da}}$ is their actual measurement during one walking step, and the covariance matrix $\boldsymbol{\Sigma}_{\mathrm{da}}$ is their variability between steps defined from measurements for other users in advance. Taking Figure 3.3 as an example, vGRF obtained from the WBB and the insole forces vary between 10 steps (bands) for a user. The data augmentation generates new datasets (dots) of both devices for an arbitrary number of virtual steps at the same sampling time points, using the measurements in the actual one step (lines) as the means and their variability as covariance.

(2) Gaussian Process Regression

GPR [103] is used to learn a model using actual/augmented datasets of the insole measurements and vGRF obtained from the WBB. GPR is a nonparametric kernel-based probabilistic regression method and can prevent overfitting on the small dataset. In addition, the learned model can estimate not only a true value but also its standard deviation as the uncertainty of the

estimate.

The GPR model using a dataset $\boldsymbol{D} = \{(\boldsymbol{f}_{\mathrm{s}i}, f_{\mathrm{wb}i}); i = 1, 2, ...N_{\mathrm{s}}\}$ is described as the following form:

$$f_{\mathrm{wb}} = \boldsymbol{h}(\boldsymbol{f}_{\mathrm{s}})^{\top}\boldsymbol{\beta} + f_{\mathrm{l}}(\boldsymbol{f}_{\mathrm{s}}), \quad \text{where } f_{\mathrm{l}}(\boldsymbol{f}_{\mathrm{s}}) \sim GP(0, k(\boldsymbol{f}_{\mathrm{s}}, \boldsymbol{f}'_{\mathrm{s}})) \tag{3.2}$$

$$f_{\mathrm{wb}}|\, f_{\mathrm{l}}(\boldsymbol{f}_{\mathrm{s}}), \boldsymbol{f}_{\mathrm{s}} \sim N(\, f_{\mathrm{wb}}|\, \boldsymbol{h}(\boldsymbol{f}_{\mathrm{s}})^{\top}\boldsymbol{\beta} + f_{\mathrm{l}}(\boldsymbol{f}_{\mathrm{s}}), \sigma^2) \tag{3.3}$$

where the input vector $\boldsymbol{f}_{\mathrm{s}}$ is measurements of the insole, the output f_{wb} is vGRF obtained from the WBB, N_{s} is the number of sampled time steps, $\boldsymbol{h}$ is constant basis function (N_{s}-by-1 vector of 1 s), $\boldsymbol{\beta}$ is a coefficient vector of $\boldsymbol{h}$, and σ^2 is a noise variance. The latent variable $f_{\mathrm{l}}(\boldsymbol{f}_{\mathrm{s}})$ is a Gaussian process and covariance function $\boldsymbol{K}(\boldsymbol{F}_{\mathrm{s}}, \boldsymbol{F}_{\mathrm{s}}); \boldsymbol{F}_{\mathrm{s}} = (\boldsymbol{f}_{\mathrm{s}1}, \boldsymbol{f}_{\mathrm{s}2}, \cdots, \boldsymbol{f}_{\mathrm{s}N_{\mathrm{s}}})^{\top}$ is set to the exponential kernel as follows:

$$\boldsymbol{K}(\boldsymbol{F}_{\mathrm{s}}, \boldsymbol{F}_{\mathrm{s}}) = \begin{pmatrix} k(\boldsymbol{f}_{\mathrm{s}1}, \boldsymbol{f}_{\mathrm{s}1}) & k(\boldsymbol{f}_{\mathrm{s}1}, \boldsymbol{f}_{\mathrm{s}2}) & \cdots & k(\boldsymbol{f}_{\mathrm{s}1}, \boldsymbol{f}_{\mathrm{s}N_{\mathrm{s}}}) \\ k(\boldsymbol{f}_{\mathrm{s}2}, \boldsymbol{f}_{\mathrm{s}1}) & k(\boldsymbol{f}_{\mathrm{s}2}, \boldsymbol{f}_{\mathrm{s}2}) & \cdots & k(\boldsymbol{f}_{\mathrm{s}2}, \boldsymbol{f}_{\mathrm{s}N_{\mathrm{s}}}) \\ \vdots & \vdots & \vdots & \vdots \\ k(\boldsymbol{f}_{\mathrm{s}N_{\mathrm{s}}}, \boldsymbol{f}_{\mathrm{s}1}) & k(\boldsymbol{f}_{\mathrm{s}N_{\mathrm{s}}}, \boldsymbol{f}_{\mathrm{s}2}) & \cdots & k(\boldsymbol{f}_{\mathrm{s}N_{\mathrm{s}}}, \boldsymbol{f}_{\mathrm{s}N_{\mathrm{s}}}) \end{pmatrix} \tag{3.4}$$

$$k(\boldsymbol{f}_{\mathrm{s}i}, \boldsymbol{f}_{\mathrm{s}j}\,|\boldsymbol{\gamma}) = \sigma_{\mathrm{f}}^2 \exp\left(-\frac{r}{\sigma_{\mathrm{l}}}\right), \quad r = \sqrt{(\boldsymbol{f}_{\mathrm{s}i} - \boldsymbol{f}_{\mathrm{s}j})^{\top}(\boldsymbol{f}_{\mathrm{s}i} - \boldsymbol{f}_{\mathrm{s}j})} \tag{3.5}$$

where kernel functions $k(\boldsymbol{f}_{\mathrm{s}i}, \boldsymbol{f}_{\mathrm{s}j}\,|\boldsymbol{\gamma})$ are based on the signal standard deviation σ_{f} and the characteristic length scale σ_{l}, and r is the Euclidean distance between $\boldsymbol{f}_{\mathrm{s}i}$ and $\boldsymbol{f}_{\mathrm{s}j}$. The exponential kernel was chosen by referring to the fitting results to datasets in an experiment. σ_{l} defines how far the input vector $\boldsymbol{f}_{\mathrm{s}i}$ parts to become uncorrelated for $\boldsymbol{f}_{\mathrm{s}j}$. Both σ_{l} and σ_{f} need to be greater than 0, and this can be enforced by the unconstrained parametrization vector $\boldsymbol{\gamma} = (\log\sigma_{\mathrm{l}}, \log\sigma_{\mathrm{f}})^{\top}$.

To learn a GPR model, the coefficient vector $\boldsymbol{\beta}$, the noise variance σ^2 and hyperparameters $\boldsymbol{\gamma}$ are estimated from the dataset $(\boldsymbol{F}_{\mathrm{s}}, \boldsymbol{f}_{\mathrm{wb}})$. These parameters are calculated to maximize the marginal log-likelihood function formed as follows:

$$\begin{aligned} \log P(\,\boldsymbol{f}_{\mathrm{wb}}|\,\boldsymbol{F}_{\mathrm{s}}, \boldsymbol{\beta}, \boldsymbol{\gamma}, \sigma^2) = &-\frac{1}{2}(\boldsymbol{f}_{\mathrm{wb}} - \boldsymbol{H}\boldsymbol{\beta})^{\top}[\boldsymbol{K}(\boldsymbol{F}_{\mathrm{s}}, \boldsymbol{F}_{\mathrm{s}}|\boldsymbol{\gamma}) + \sigma^2\boldsymbol{I}_{N_{\mathrm{s}}}]^{-1}(\boldsymbol{f}_{\mathrm{wb}} - \boldsymbol{H}\boldsymbol{\beta}) \\ &- \frac{1}{2}\log\left|\boldsymbol{K}(\boldsymbol{F}_{\mathrm{s}}, \boldsymbol{F}_{\mathrm{s}}|\boldsymbol{\gamma}) + \sigma^2\boldsymbol{I}_{N_{\mathrm{s}}}\right| - \frac{N_{\mathrm{s}}}{2}\log 2\pi \end{aligned} \tag{3.6}$$

where $\boldsymbol{H} = (\boldsymbol{h}_1, \boldsymbol{h}_2, \cdots, \boldsymbol{h}_{N_{\mathrm{s}}})^{\top}$, the initial value of σ_{l} is the mean of standard deviations of the input $\boldsymbol{F}_{\mathrm{s}}$, and the initial values of σ_{f} and σ are the standard deviation of the output $\boldsymbol{f}_{\mathrm{wb}}$ divided by $\sqrt{2}$. This study assumed that the effect of horizontal GRF during walking was negligible in accordance with the report that the total plantar pressure measured by a commercial insole-type

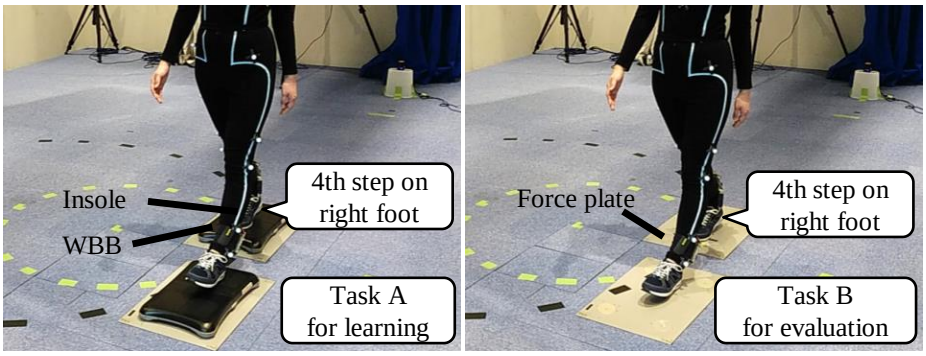

(a) (b)

Figure 3.4. Experimental walkways. (a) Participants wearing the insole walked on the WBB with a small step up. (b) The participants walked on the force plates. In both tasks, the participants walked straight at a self-selected pace.

sensor approximately matched the vGRF (the difference was less than 4% [12]).

(3) Estimation

The learned GPR model probabilistically estimates vGRF during walking. The probability density of estimated vGRF $f_{\mathrm{est}k}$ given $\boldsymbol{f}_{\mathrm{wb}}$, $\boldsymbol{F}_{\mathrm{s}}$, parameters $(\boldsymbol{\beta}, \boldsymbol{\gamma}, \sigma^2)$, and an input $\boldsymbol{f}_{\mathrm{s}k}$ at time step k is as follows:

$$f_{\mathrm{est}k} | \, \boldsymbol{f}_{\mathrm{wb}}, \boldsymbol{F}_{\mathrm{s}}, \boldsymbol{f}_{\mathrm{s}k} \sim N(f_{\mathrm{est}k} | \, \boldsymbol{h}(\boldsymbol{f}_{\mathrm{s}k})^{\top} \boldsymbol{\beta} + \boldsymbol{\mu}_{\mathrm{gp}}, \sigma^2 + \boldsymbol{\Sigma}_{\mathrm{gp}}) \tag{3.7}$$

$$\boldsymbol{\mu}_{\mathrm{gp}} = \boldsymbol{K}(\boldsymbol{f}_{\mathrm{s}k}^{\top}, \boldsymbol{F}_{\mathrm{s}})(\boldsymbol{K}(\boldsymbol{F}_{\mathrm{s}}, \boldsymbol{F}_{\mathrm{s}}) + \sigma^2 \boldsymbol{I}_{N_{\mathrm{s}}})^{-1}(\boldsymbol{f}_{\mathrm{wb}} - \boldsymbol{H}\boldsymbol{\beta}) \tag{3.8}$$

$$\boldsymbol{\Sigma}_{\mathrm{gp}} = \boldsymbol{k}(\boldsymbol{f}_{\mathrm{s}k}, \boldsymbol{f}_{\mathrm{s}k}) - \boldsymbol{K}(\boldsymbol{f}_{\mathrm{s}k}^{\top}, \boldsymbol{F}_{\mathrm{s}})(\boldsymbol{K}(\boldsymbol{F}_{\mathrm{s}}, \boldsymbol{F}_{\mathrm{s}}) + \sigma^2 \boldsymbol{I}_{N_{\mathrm{s}}})^{-1} \boldsymbol{K}(\boldsymbol{F}_{\mathrm{s}}, \boldsymbol{f}_{\mathrm{s}k}^{\top}) \tag{3.9}$$

The expected value of estimation $f_{\mathrm{est}k}$ is as follows:

$$\begin{aligned} \mathrm{E}(f_{\mathrm{est}k} | \, \boldsymbol{f}_{\mathrm{wb}}, \boldsymbol{F}_{\mathrm{s}}, \boldsymbol{f}_{\mathrm{s}k}) &= \boldsymbol{h}(\boldsymbol{f}_{\mathrm{s}k})^{\top} \boldsymbol{\beta} + \boldsymbol{K}(\boldsymbol{f}_{\mathrm{s}k}, \boldsymbol{F}_{\mathrm{s}} | \boldsymbol{\gamma}) \boldsymbol{\alpha} \\ &= \boldsymbol{h}(\boldsymbol{f}_{\mathrm{s}k})^{\top} \boldsymbol{\beta} + \sum_{i=1}^{N_{\mathrm{s}}} \boldsymbol{\alpha}_i k(\boldsymbol{f}_{\mathrm{s}k}, \boldsymbol{f}_{\mathrm{s}i} | \boldsymbol{\gamma}) \end{aligned} \tag{3.10}$$

where $\boldsymbol{\alpha} = (\boldsymbol{K}(\boldsymbol{F}_{\mathrm{s}}, \boldsymbol{F}_{\mathrm{s}} | \boldsymbol{\gamma}) + \sigma^2 \boldsymbol{I}_{N_{\mathrm{s}}})^{-1}(\boldsymbol{f}_{\mathrm{wb}} - \boldsymbol{H}\boldsymbol{\beta})$.

3.3 Evaluation of One-step Learning

3.3.1 Study Procedure

Six healthy adults (five males, age: 24.0 ± 3.6 years, height: 1.70 ± 0.07 m, body mass: 65.6 ± 7.2 kg) were recruited for this study. Ethical approval was obtained from Keio University Research Ethics Committee (reference number 30–68) prior to the experiments. All participants provided informed consent. The participants wore shoes with the instrumented insoles inserted. Their task executions were measured using the insoles, the two WBBs, and two force plates (Kistler, Winterthur, CH). Measurements were collected from the insoles and the WBB at 100 Hz, and from the force plates at 1000 Hz. All devices were synchronized via voltage inputs and radio communications. The participants were asked to perform the following tasks in walkways, as shown in Figure 3.4:

A. For learning the model, the participants walked straight and naturally at a self-selected pace with their fourth–fifth steps (right–left) contacting the WBBs. At the fourth step, the participants walked on the WBB with a small step up. This task was repeated 10 times.

B. For evaluating the learned models, the participants walked straight and naturally at a self-selected pace with their fourth–fifth steps (right–left) contacting the force plates. This task was repeated 10 times.

3.3.2 Acquisition of Datasets for Learning and Evaluation

In both tasks A and B, measurements of all devices for the fourth steps (right foot) were used for data analysis. For learning the model, a dataset of the insole and the WBB in a stance phase during walking was obtained from task A. In addition, the measurements during 100 ms before/after the stance phase were contained to the dataset in order to suppress estimation offsets in a swing phase. The datasets for 10 steps were acquired from 10 trials in task A.

For evaluating the models, a dataset of the insole and the force plate in a stance phase and 100 ms before/after that was obtained from task B. The measurements of the force plate were resampled at 100 Hz to match the insole. The datasets for 10 steps were acquired from 10 trials in task B.

3.3.3 Evaluation of Probabilistic Data Augmentation

(1) Data Analysis

For evaluating the effectiveness of the data augmentation, each dataset of 10 walking steps in task A was augmented with a different number of virtual steps ($n_{\mathrm{da}} = 0, 1, ..., 8$), following Section 3.2.2(1). For the augmentation, a variability of the insole measurements and vGRF obtained from the WBB at each sampling time point (1–100) in a step was determined from datasets of five participants except for each participant. A multivariate normal distribution was fitted to the datasets of the five participants at the same sampling time points in 10 steps of task A using the expectation-maximization algorithm, and a mean and covariances of them were then calculated at each point. Using the dataset from one measured step (10 steps) and the data augmentation ($n_{\mathrm{da}} = 0, 1, ..., 8$) based on the variabilities defined from the other five participants in task A, a total of 80 GPR models were constructed. The models were learned using the MATLAB Statistics and Machine Learning Toolbox.

The performance of learned models was evaluated through their estimation accuracy of vGRF compared with ground truth obtained from the force plate in 10 steps of task B. To assess the accuracy of the estimated vGRF in the entire step, the normalized root mean squared error (nRMSE) was calculated as follows:

$$\mathrm{nRMSE}\ (\%\mathrm{BW}) = \frac{100\sqrt{\frac{1}{N_{\mathrm{t}}}\sum_{k=1}^{N_{\mathrm{t}}}\left(f_{\mathrm{fp}k} - f_{\mathrm{est}k}\right)^2}}{mg} \tag{3.11}$$

where k is the time step, N_{t} is the size of the dataset, $f_{\mathrm{fp}k}$ is the ground truth obtained from the force plate, $f_{\mathrm{est}k}$ is the expected estimate of the model, and mg is the participants' body weight. In addition, their accuracies at peaks (P1 and P2) and a trough (T) in the stance described in Figure 3.2 (f), which were examined as evaluation indexes of gait abnormalities at clinical sites [1], were assessed using the normalized Error (nError) calculated as follows:

$$\mathrm{nError}\ (\%\mathrm{BW}) = \frac{100\left(f_{\mathrm{fp}}^{i} - f_{\mathrm{est}}^{i}\right)}{mg} \quad (i = \mathrm{P1,T,P2}) \tag{3.12}$$

To evaluate both nRMSE and nError, estimation accuracy criteria were set to 12% similar to Chapter 2.

Table 3.1. Accuracy of vGRF estimated by GPR models using data augmentation.

	nRMSE in each number of augmented steps for learning n_{da} (%BW)								
ID	$n_{da}=0$	$n_{da}=1$	$n_{da}=2$	$n_{da}=3$	$n_{da}=4$	$n_{da}=5$	$n_{da}=6$	$n_{da}=7$	$n_{da}=8$
A	7.0 (4.0)	5.7 (2.2)	5.5 (1.9)	5.8 (2.1)	5.2 (1.5)	5.3 (1.7)	4.9 (1.4)	5.2 (1.5)	5.0 (1.1)
B	8.4 (3.3)	6.7 (2.2)	6.6 (1.9)	6.4 (2.2)	6.3 (1.9)	6.2 (1.9)	6.1 (2.0)	6.2 (1.9)	6.2 (2.1)
C	6.9 (2.1)	5.9 (1.5)	5.8 (1.4)	5.9 (1.3)	5.7 (1.4)	5.8 (1.2)	5.8 (1.4)	6.0 (1.6)	6.0 (1.4)
D	6.7 (2.4)	5.3 (1.7)	5.4 (1.6)	5.0 (1.4)	5.1 (1.6)	5.1 (1.8)	5.1 (1.7)	5.0 (1.6)	4.7 (1.4)
E	13.1 (3.8)	11.6 (2.7)	11.5 (2.5)	10.8 (2.3)	11.4 (2.5)	10.9 (2.4)	11.1 (2.5)	10.7 (2.3)	10.7 (2.4)
F	9.3 (2.6)	8.0 (2.2)	7.9 (2.2)	7.5 (2.1)	7.6 (2.5)	7.9 (2.3)	7.7 (2.4)	7.8 (2.4)	7.8 (2.3)
All	8.6 (3.8)	7.2 (3.0)	7.1 (2.9)	6.9 (2.7)	6.9 (2.9)	6.9 (2.8)	6.8 (2.9)	6.8 (2.7)	6.7 (2.8)
p	0.009	0.002	0.002	<0.001	0.002	0.001	0.001	<0.001	0.001
$1-\beta$	0.602	0.951	0.968	0.988	0.977	0.985	0.982	0.990	0.989

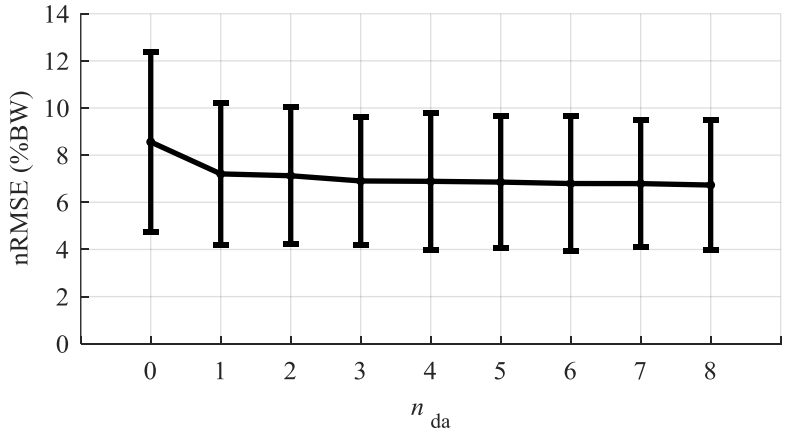

Figure 3.5. The nRMSE (for overall) of GPR models learned using the different number of augmented steps ($n_{da}=0,1,...,8$).

(2) Results

The nRMSE of the GPR models learned using datasets consisting of one measured step and the different number of augmented steps ($n_{da}=0,1,...,8$) are summarized in Table 3.1 and Figure 3.5. The nErrors of the GPR models with data augmentation at peaks/trough are shown in Table 3.2. The mean (± SD) of nRMSE and nError are given for each participant and overall. The nRMSE and nError for overall were evaluated by one-sample t-tests. The null hypothesis was that the accuracy of the proposed method came from a population with a mean of 12%, against the alternative that the mean was under 12%. In addition, vGRF lines estimated by the GPR models with/without augmentation ($n_{da}=0$ and 8), their estimation intervals, and the ground truth from the force plate are presented in Figure 3.6. Each plot is the mean of 10 steps in task B.

As shown in Table 3.1, although the model without data augmentation ($n_{da}=0$) had mean nRMSE under 12%, the result did not provide strong statistical support ($1-\beta=0.602$). Meanwhile, the data augmentation ($n_{da}\geq 1$) showed accuracy with statistical validity ($p=0.002$,

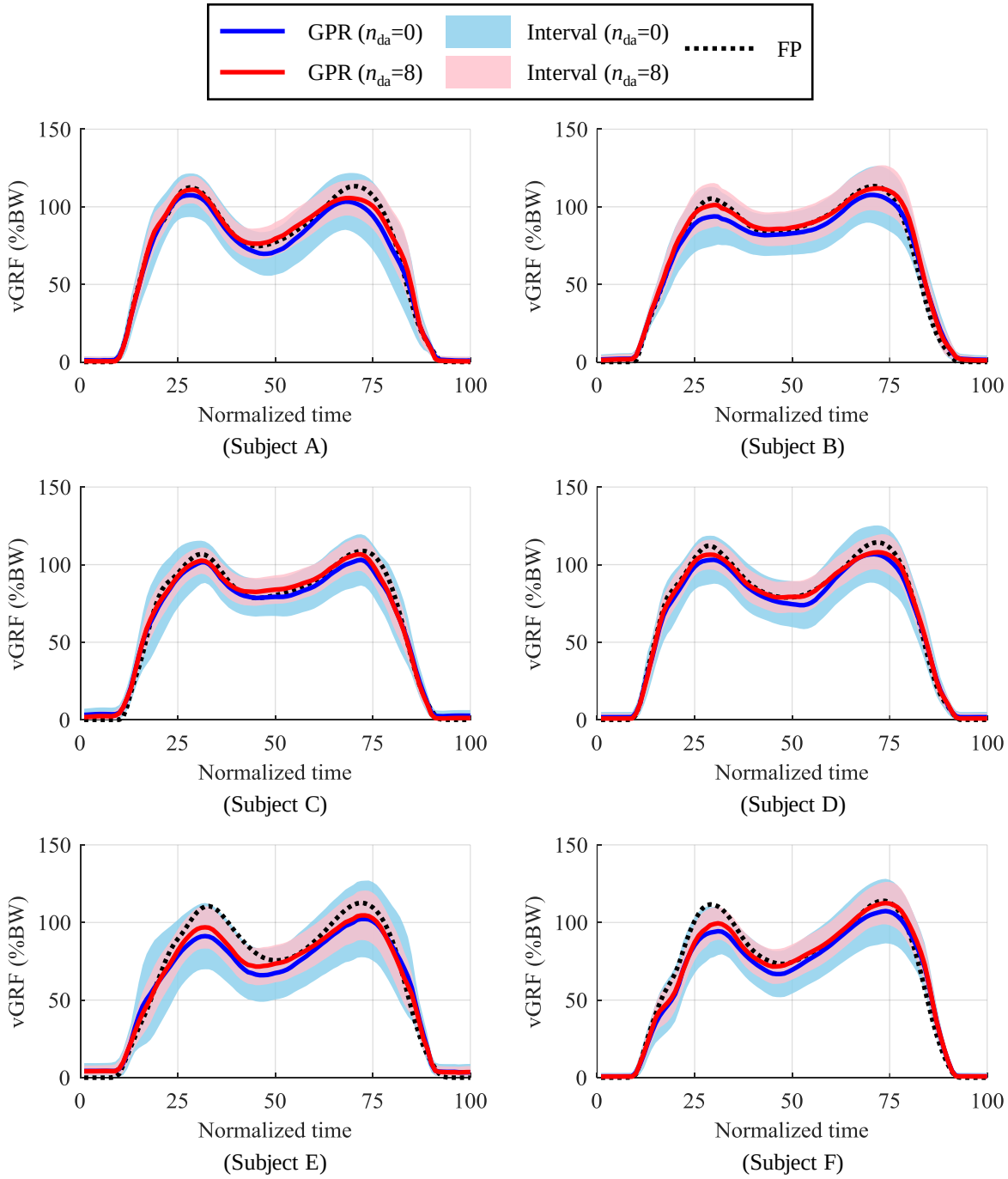

Figure 3.6. vGRF lines estimated by GPR models learned using datasets with the different number of data augmentation ($n_{\mathrm{da}} = 0$ and 8 as blue and red lines), the estimation intervals of the GPR models (Interval), and the ground truth from the force plate (FP) in a stance are illustrated for each subject. Each plot is a mean of 10 steps in task B.

Table 3.2. Accuracy of vGRF at P1/T/P2 estimated by GPR models using data augmentation.

		nError in each number of augmented steps for learning n_{da} (%BW)								
ID	Part	$n_{da}=0$	$n_{da}=1$	$n_{da}=2$	$n_{da}=3$	$n_{da}=4$	$n_{da}=5$	$n_{da}=6$	$n_{da}=7$	$n_{da}=8$
	P1	-4.7 (2.8)	-3.7 (2.5)	-2.1 (3.1)	-2.8 (3.0)	-1.8 (2.6)	-2.1 (3.2)	-1.4 (2.9)	-2.0 (2.8)	-1.1 (3.0)
A	T	-6.0 (8.0)	-2.7 (4.2)	-1.1 (3.8)	-0.4 (3.5)	-0.3 (3.5)	0.1 (2.8)	0.6 (3.0)	0.7 (3.3)	0.7 (3.1)
	P2	-9.7 (9.2)	-7.5 (6.8)	-7.2 (5.6)	-8.3 (6.2)	-6.6 (6.2)	-7.0 (5.4)	-7.3 (6.2)	-6.8 (4.6)	-7.7 (6.2)
	P1	-12.7 (14.7)	-6.0 (5.3)	-4.6 (4.7)	-3.1 (3.6)	-4.0 (3.5)	-3.1 (4.6)	-3.0 (4.7)	-3.0 (4.7)	-3.4 (4.5)
B	T	-6.7 (14.5)	-2.4 (7.5)	-0.9 (6.7)	-0.8 (7.0)	-0.1 (6.4)	-0.2 (6.6)	-0.4 (6.3)	-0.1 (6.2)	0.1 (6.4)
	P2	-10.7 (19.2)	-5.1 (10.2)	-5.4 (10.3)	-5.1 (10.2)	-3.8 (9.9)	-2.9 (8.4)	-3.6 (10.1)	-3.5 (9.4)	-3.5 (8.6)
	P1	-4.6 (3.8)	-3.7 (3.2)	-3.7 (3.8)	-3.6 (3.9)	-3.5 (3.4)	-4.0 (3.8)	-3.4 (3.7)	-3.1 (3.9)	-3.0 (3.9)
C	T	-1.1 (5.7)	1.1 (3.4)	1.5 (3.7)	2.0 (3.0)	2.2 (3.3)	1.9 (3.1)	2.4 (2.9)	2.6 (3.2)	2.7 (3.0)
	P2	-10.1 (12.3)	-5.9 (10.4)	-5.7 (10.0)	-5.1 (9.7)	-5.2 (9.6)	-5.6 (10.1)	-5.2 (10.2)	-6.3 (10.3)	-5.9 (9.8)
	P1	-9.0 (4.3)	-5.9 (3.4)	-6.1 (3.3)	-5.2 (3.4)	-5.7 (3.3)	-5.4 (3.0)	-5.6 (3.8)	-5.8 (3.3)	-5.7 (3.4)
D	T	-6.6 (6.9)	-3.6 (3.9)	-3.3 (4.1)	-2.4 (3.4)	-2.2 (3.2)	-2.1 (3.1)	-2.0 (3.2)	-1.7 (3.0)	-1.5 (2.4)
	P2	-8.7 (8.0)	-10.5 (10.5)	-9.0 (8.3)	-9.9 (8.9)	-9.6 (10.3)	-9.4 (9.2)	-8.4 (7.8)	-9.6 (9.7)	-8.6 (9.1)
	P1	-17.8 (8.7)	-14.6 (6.5)	-14.5 (7.1)	-13.4 (6.8)	-13.8 (7.5)	-13.1 (6.3)	-11.8 (6.9)	-11.9 (6.8)	-11.8 (6.7)
E	T	-10.8 (7.8)	-8.5 (6.9)	-7.4 (6.5)	-6.6 (6.3)	-7.3 (6.8)	-6.7 (6.7)	-6.1 (6.2)	-5.3 (6.3)	-5.4 (6.9)
	P2	-9.3 (8.9)	-7.4 (8.5)	-8.0 (8.4)	-7.0 (7.5)	-7.5 (9.1)	-6.5 (7.7)	-8.0 (9.5)	-7.8 (9.3)	-9.1 (10.7)
	P1	-15.3 (5.7)	-12.7 (5.8)	-12.9 (6.6)	-11.4 (7.2)	-11.0 (6.5)	-11.8 (6.6)	-11.1 (7.3)	-10.9 (8.0)	-10.5 (8.1)
F	T	-7.2 (6.1)	-4.3 (5.0)	-3.2 (4.9)	-2.7 (5.0)	-3.0 (5.3)	-2.6 (5.2)	-2.5 (4.8)	-1.8 (4.8)	-2.5 (4.7)
	P2	-7.5 (8.8)	-3.8 (8.8)	-4.5 (9.6)	-4.4 (8.0)	-3.7 (8.5)	-3.4 (6.8)	-3.9 (9.5)	-3.6 (9.5)	-2.3 (6.9)
	P1	-10.7 (9.3)	-7.8 (6.3)	-7.3 (6.9)	-6.6 (6.5)	-6.6 (6.5)	-6.6 (6.4)	-6.1 (6.5)	-6.1 (6.6)	-5.9 (6.6)
All	T	-6.4 (9.1)	-3.4 (6.1)	-2.4 (5.8)	-1.8 (5.6)	-1.8 (5.8)	-1.6 (5.6)	-1.4 (5.3)	-0.9 (5.3)	-1.0 (5.4)
	P2	-9.4 (11.7)	-6.7 (9.5)	-6.6 (8.9)	-6.6 (8.7)	-6.1 (9.2)	-5.8 (8.3)	-6.1 (9.2)	-6.3 (9.2)	-6.2 (9.0)
	P1	0.293	0.039	0.038	0.017	0.019	0.018	0.011	0.010	0.009
p	T	0.004	<0.001	<0.001	<0.001	<0.001	<0.001	<0.001	<0.001	<0.001
	P2	0.001	0.001	<0.001	<0.001	<0.001	<0.001	<0.001	<0.001	0.002
	P1	0.090	0.408	0.422	0.546	0.545	0.555	0.610	0.597	0.618
$1-\beta$	T	0.368	0.906	0.965	0.984	0.979	0.987	0.994	0.997	0.995
	P2	0.123	0.321	0.355	0.369	0.389	0.471	0.392	0.371	0.388

$1-\beta = 0.602$). Improvements in the accuracy for overall participants were found until $n_{da} = 3$ and the accuracy did not change when $n_{da} \geq 4$. Table 3.2 shows that the model without data augmentation did not show valid accuracy for P1 of nError. Although valid accuracy (under 12% and $p < 0.05$) for all parts (P1, T, P2) were found when $n_{da} = 2$, statistical support ($1-\beta > 0.8$) was provided for only trough (T). Figure 3.6 shows that the GPR models with data augmentation ($n_{da} = 8$) estimated the vGRF lines more accurately than the models without augmentation ($n_{da} = 0$). The estimation intervals of the GPR models became smaller when $n_{da} = 8$ than $n_{da} = 0$, indicating that the GPR model estimated the vGRF more deterministically by the data augmentation.

Table 3.3. Accuracy of vGRF estimated by LIN and GPR models.

		nRMSE in each number of walking steps for learning n_{st} (%BW)								
ID	Model	$n_{st}=1$	$n_{st}=2$	$n_{st}=3$	$n_{st}=4$	$n_{st}=5$	$n_{st}=6$	$n_{st}=7$	$n_{st}=8$	$n_{st}=9$
A	LIN	20.8 (16.1)	9.4 (5.2)	7.9 (3.9)	7.4 (2.8)	7.1 (3.0)	6.7 (1.6)	6.5 (1.4)	6.3 (1.1)	6.3 (1.1)
	GPR	7.0 (4.0)	5.9 (2.7)	5.8 (2.4)	5.3 (2.4)	5.0 (1.9)	4.6 (1.8)	4.6 (1.7)	4.4 (1.7)	4.3 (1.5)
B	LIN	19.6 (13.9)	12.8 (6.3)	9.4 (3.9)	8.5 (3.4)	9.1 (3.3)	8.1 (3.1)	8.2 (3.0)	8.1 (3.0)	7.9 (3.1)
	GPR	8.4 (3.3)	6.6 (2.4)	5.5 (1.7)	5.3 (1.7)	5.4 (1.6)	5.1 (1.4)	5.0 (1.2)	5.1 (1.3)	5.0 (1.1)
C	LIN	16.3 (6.8)	12.0 (4.5)	9.0 (3.0)	8.4 (3.1)	8.7 (2.9)	7.7 (2.4)	7.6 (2.4)	7.6 (2.4)	7.4 (2.3)
	GPR	6.9 (2.1)	6.1 (1.8)	5.8 (1.5)	5.6 (1.5)	5.3 (1.4)	5.2 (1.3)	5.1 (1.3)	5.1 (1.3)	5.0 (1.3)
D	LIN	20.4 (19.5)	9.2 (7.0)	6.8 (2.3)	6.2 (1.6)	6.3 (2.1)	6.0 (1.5)	6.0 (1.5)	5.9 (1.5)	5.9 (1.4)
	GPR	6.7 (2.4)	5.0 (1.6)	4.4 (1.4)	3.7 (1.1)	3.7 (1.0)	3.4 (1.0)	3.3 (0.9)	3.2 (0.9)	3.1 (0.9)
E	LIN	39.9 (38.7)	26.4 (26.0)	16.1 (7.2)	15.5 (6.3)	16.3 (11.5)	13.5 (3.9)	13.0 (3.7)	12.9 (3.9)	12.6 (3.6)
	GPR	13.1 (3.8)	10.4 (2.6)	9.7 (2.1)	9.1 (2.0)	9.0 (1.9)	8.8 (1.7)	8.8 (1.5)	8.8 (1.4)	8.8 (1.3)
F	LIN	25.6 (16.3)	10.0 (5.1)	12.7 (9.7)	8.5 (2.6)	8.0 (2.0)	7.9 (2.0)	7.7 (1.9)	7.6 (1.9)	7.5 (1.9)
	GPR	9.3 (2.6)	7.6 (2.2)	7.6 (2.3)	7.5 (2.0)	7.4 (2.0)	7.6 (2.0)	7.5 (2.0)	7.5 (2.0)	7.5 (1.9)
All	LIN	23.8 (22.3)	13.3 (13.2)	10.3 (6.4)	9.1 (4.7)	9.3 (6.2)	8.3 (3.5)	8.2 (3.4)	8.1 (3.4)	7.9 (3.2)
	GPR	8.6 (3.8)	6.9 (2.8)	6.5 (2.6)	6.1 (2.5)	6.0 (2.4)	5.8 (2.4)	5.7 (2.4)	5.7 (2.4)	5.6 (2.4)
p	LIN	–	–	0.144	0.041	0.060	0.010	0.007	0.006	0.004
	GPR	0.009	<0.001	<0.001	<0.001	<0.001	<0.001	<0.001	<0.001	<0.001
$1-\beta$	LIN	–	–	0.139	0.370	0.241	0.705	0.774	0.789	0.838
	GPR	0.602	0.982	0.997	0.999	1.000	1.000	1.000	1.000	1.000

3.3.4 Evaluation of GPR

(1) Data Analysis

For assessing the advantage of GPR for small data learning, GPR models were learned from a different number of walking steps ($n_{st} = 1, 2, ..., 9$) of task A. When $n_{st} = 1$, each step of 10 trials was used to learn 10 models individually. In each of $n_{st} = 2, ..., 9$, 10 models were learned using 10 datasets combining the steps taken randomly and equally from 10 steps. In addition, a linear regression model (LIN) proposed in [23] was constructed as a comparative approach using the same datasets. The estimation accuracy of the learned models was evaluated by comparison with the force plate using nRMSE and nError for 10 steps of task B similar to the evaluation of probabilistic data augmentation in Section 3.3.3.

(2) Results

The nRMSE of the LIN and GPR models learned from the different number of steps ($n_{st} = 1, 2, ..., 9$) are summarized in Table 3.3 and Figure 3.7. Overall nRMSEs of both models were tested by one-sample t-tests. The null hypothesis was that the accuracy of the proposed method came from a population with a mean of 12%, against the alternative that the mean was under 12%. The nError of the GPR models at peaks/trough are summarized in Table 3.4. The mean ($\pm$ SD) of nRMSE and nError are given for each participant and overall. Overall nErrors were evaluated by one-sample t-tests similar to nRMSE. In addition, vGRF lines estimated by the

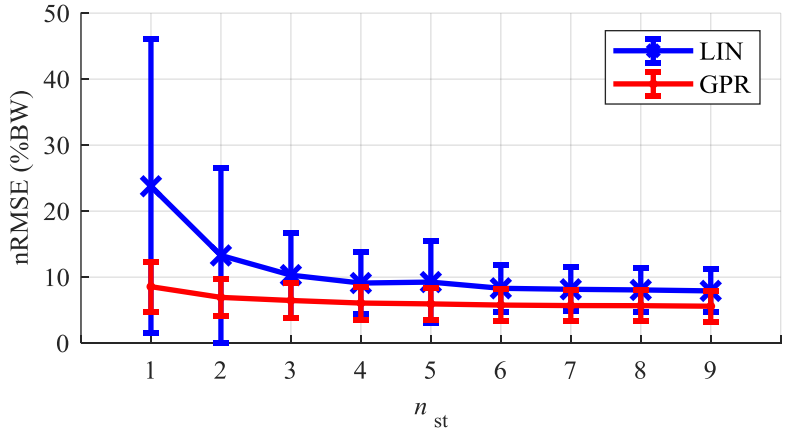

Figure 3.7. The nRMSE (for overall) of the LIN and GPR models, which were learned using a different number of steps ($n_{\mathrm{st}} = 1, 2, ..., 9$).

LIN and GPR models learned from the different number of steps (n_{st}=1 and 9), their estimation intervals, the ground truth obtained from the force plate, and the total force of the 15 insole sensors in a stance are illustrated in Figure 3.8. Each plot is the mean of 10 steps in task B.

As shown in Figure 3.7 and Table 3.3, both the LIN and GPR models enhanced their estimation accuracies as the number of steps for learning increased. The LIN models learned from small numbers of steps ($n_{\mathrm{st}} = 1$ and 2) had large estimation errors over 12% and showed valid accuracy ($p < 0.05$, $1-\beta > 0.8$) only when $n_{\mathrm{st}} = 9$. Meanwhile, the GPR showed the valid accuracy ($p < 0.05$, $1-\beta > 0.8$) for overall when $n_{\mathrm{st}} = 2$ and enhanced the overall mean until $n_{\mathrm{st}} = 9$. The GPR models exhibited better performance when compared with the LIN models for every number of walking steps for learning. Table 3.4 shows that the accuracy of all three parts estimated by the GPR models improved as the number of steps for learning increased, and the nEorror of all parts for overall participants became under 12% with statistical support when $n_{\mathrm{st}} \geq 2$ ($p < 0.05$) and $n_{\mathrm{st}} \geq 7$ ($1-\beta > 0.8$). Figure 3.7 shows that the GPR models estimated the lines of vGRF more accurately and deterministically than the LIN models when both n_{st} =1 and 9. The intervals of GRF became smaller when $n_{\mathrm{st}} = 9$ than $n_{\mathrm{st}} = 1$, indicating that the GPR model estimated vGRF more deterministically by increasing the size of the datasets for learning.

3.3.5 Discussion

(1) General Discussion

As shown in Table 3.1, the model with data augmentation ($n_{\mathrm{da}} \geq 1$) showed valid estimation accuracy (nRMSE under 12%, $p < 0.05$, $1-\beta > 0.8$), which was enhanced when compared with no augmentation ($n_{\mathrm{da}} = 0$). In addition, Table 3.2 illustrates that the mean nError at

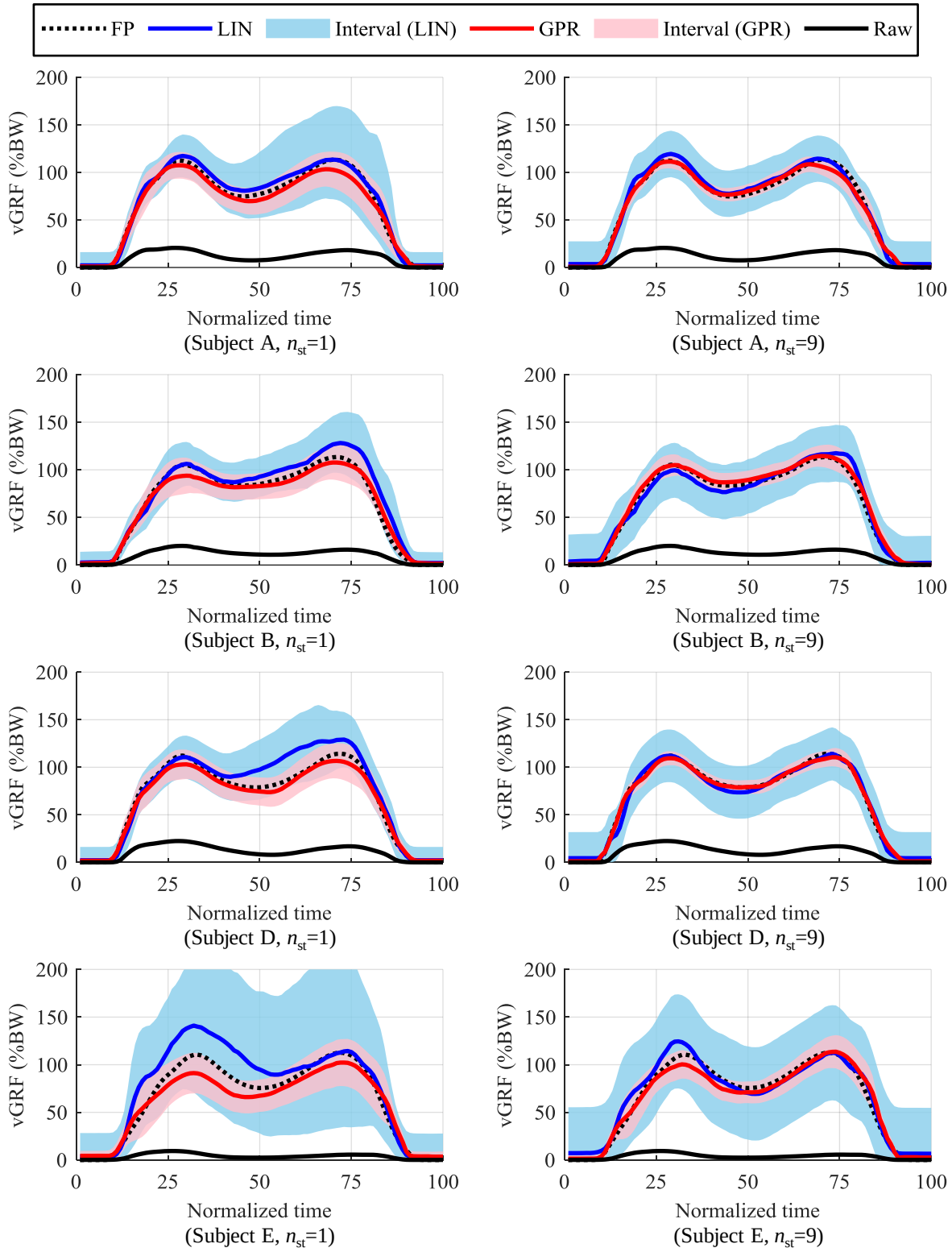

Figure 3.8. vGRF lines estimated by two models (LIN, GPR), the estimation intervals of the GPR model (Interval), the ground truth from the force plate (FP) and the total force of the insole (Raw) in a stance are illustrated. Each plot is the mean of 10 steps in task B. The results are of the models learned using a different number of steps (n_{st} = 1 and 9) in four subjects (A, B, D, E).

Table 3.4. Accuracy of vGRF at P1/T/P2 estimated by GPR models using single/multiple walking steps.

		nError in each number of walking steps for learning n_{st} (%BW)								
ID	Part	$n_{st}=1$	$n_{st}=2$	$n_{st}=3$	$n_{st}=4$	$n_{st}=5$	$n_{st}=6$	$n_{st}=7$	$n_{st}=8$	$n_{st}=9$
	P1	-4.7 (2.8)	-2.6 (2.6)	-2.8 (2.3)	-1.4 (1.9)	-1.4 (2.0)	-1.4 (1.5)	-1.3 (1.6)	-1.2 (1.4)	-1.1 (1.4)
A	T	-6.0 (8.0)	-2.6 (4.8)	-1.7 (3.6)	-1.1 (3.2)	0.1 (2.2)	0.3 (1.7)	0.9 (1.4)	1.2 (1.5)	1.4 (1.4)
	P2	-9.7 (9.2)	-7.0 (6.4)	-5.7 (5.9)	-6.4 (5.6)	-4.4 (4.1)	-5.4 (4.5)	-4.1 (4.0)	-4.4 (3.7)	-4.4 (3.7)
	P1	-12.7 (14.7)	-8.6 (11.1)	-6.0 (3.5)	-4.6 (4.1)	-3.4 (3.2)	-2.0 (3.1)	-1.5 (2.8)	-0.7 (2.6)	-0.1 (2.4)
B	T	-6.7 (14.5)	-2.9 (10.7)	-0.9 (5.8)	-0.2 (5.7)	0.7 (5.6)	1.3 (5.5)	1.7 (5.4)	2.1 (5.6)	2.5 (5.5)
	P2	-10.7 (19.2)	-5.1 (15.3)	-1.7 (8.3)	-1.7 (8.2)	0.4 (6.6)	-1.0 (8.2)	0.5 (6.0)	0.3 (6.5)	-0.1 (6.9)
	P1	-4.6 (3.8)	-4.0 (3.8)	-4.4 (4.0)	-4.6 (4.2)	-4.1 (4.1)	-5.2 (4.1)	-5.1 (4.1)	-5.3 (4.3)	-5.5 (4.5)
C	T	-1.1 (5.7)	-0.1 (4.8)	0.4 (3.9)	0.7 (3.2)	0.9 (3.3)	0.8 (2.9)	0.9 (2.9)	0.9 (2.9)	1.0 (2.7)
	P2	-10.1 (12.3)	-7.6 (10.1)	-4.5 (8.8)	-7.6 (11.1)	-6.2 (10.3)	-5.4 (10.1)	-3.5 (8.6)	-4.4 (9.2)	-4.1 (9.1)
	P1	-9.0 (4.3)	-6.7 (3.9)	-4.5 (2.6)	-4.1 (2.6)	-3.9 (2.8)	-3.6 (2.6)	-3.4 (2.3)	-3.2 (2.3)	-2.9 (2.1)
D	T	-6.6 (6.9)	-3.2 (4.6)	-2.4 (3.4)	-1.2 (1.6)	-1.4 (2.2)	-1.0 (1.5)	-1.0 (1.4)	-0.9 (1.4)	-0.7 (1.1)
	P2	-8.7 (8.0)	-6.9 (4.9)	-7.5 (6.8)	-5.4 (4.8)	-5.8 (5.2)	-5.7 (6.0)	-5.9 (6.8)	-6.2 (7.5)	-6.2 (7.8)
	P1	-17.8 (8.7)	-14.1 (7.1)	-13.8 (6.7)	-11.3 (6.2)	-11.7 (5.7)	-10.5 (5.2)	-10.8 (4.9)	-9.9 (4.5)	-10.0 (4.3)
E	T	-10.8 (7.8)	-7.3 (5.6)	-6.0 (4.9)	-5.6 (4.8)	-5.7 (4.6)	-5.6 (4.7)	-5.5 (4.6)	-5.6 (4.6)	-5.7 (4.6)
	P2	-9.3 (8.9)	-4.9 (6.8)	-2.6 (6.5)	-2.9 (8.9)	-1.0 (9.2)	-1.2 (9.0)	1.2 (6.4)	0.6 (9.8)	2.1 (8.1)
	P1	-15.3 (5.7)	-12.0 (5.4)	-11.2 (6.0)	-11.4 (5.5)	-10.6 (5.1)	-10.6 (5.4)	-10.1 (5.3)	-10.1 (5.2)	-9.8 (4.9)
F	T	-7.2 (6.1)	-4.8 (4.9)	-5.2 (5.5)	-3.9 (4.4)	-4.0 (5.2)	-3.6 (4.6)	-3.7 (4.9)	-3.4 (4.7)	-3.2 (4.6)
	P2	-7.5 (8.8)	-2.7 (5.5)	-3.1 (7.2)	-0.6 (5.4)	0.2 (3.2)	-0.4 (7.0)	0.2 (5.4)	-0.8 (9.4)	0.2 (7.2)
	P1	-10.7 (9.3)	-8.0 (7.5)	-7.1 (6.0)	-6.2 (5.7)	-5.9 (5.6)	-5.6 (5.4)	-5.4 (5.3)	-5.1 (5.3)	-4.9 (5.3)
All	T	-6.4 (9.1)	-3.5 (6.6)	-2.6 (5.1)	-1.9 (4.6)	-1.6 (4.8)	-1.3 (4.5)	-1.1 (4.6)	-1.0 (4.7)	-0.8 (4.7)
	P2	-9.4 (11.7)	-5.7 (9.1)	-4.2 (7.5)	-4.1 (8.1)	-2.8 (7.4)	-3.2 (8.0)	-1.9 (6.9)	-2.5 (8.3)	-2.1 (7.9)
	P1	0.293	0.040	0.020	0.009	0.008	0.006	0.006	0.005	0.005
p	T	0.004	<0.001	<0.001	<0.001	<0.001	<0.001	<0.001	<0.001	<0.001
	P2	0.001	<0.001	<0.001	<0.001	<0.001	<0.001	<0.001	<0.001	<0.001
	P1	0.090	0.306	0.532	0.684	0.748	0.803	0.831	0.867	0.879
$1-\beta$	T	0.368	0.851	0.984	0.998	0.998	0.999	0.999	0.999	0.999
	P2	0.123	0.431	0.703	0.661	0.829	0.749	0.920	0.772	0.840

peaks/trough for overall participants was lower than 12% ($p < 0.05$) when $n_{da} \geq 2$. These results indicate that the data augmentation from one walking step contributes to the valid estimation of vGRF during walking.

As can be seen in Figure 3.7 and Table 3.3, both the LIN and GPR models enhanced the estimation accuracy as the number of walking steps for learning increased. This result is natural because the generalization performance of the learned models can be enhanced as the size of the dataset increases and becomes more diverse. Meanwhile, while the LIN models decreased the accuracy when the size of the dataset was small, the GPR model showed better performance than LIN. In addition, GPR exhibits better performance when compared with LIN for every number of steps for overall participants. These were because GPR is a probabilistic learning technique based on Bayesian inference and does not induce overfitting on the small dataset corrupted by measurement noise and the inconsistency of walking. Table 3.4 shows that the nError at peaks/trough of the GPR models for overall participants were under 12% ($p < 0.05$) when $n_{st} \geq 2$.

From the above results, this study found that the one-step learning, which augments a dataset for one walking step to virtual datasets for multiple steps, could estimate vGRF during walking with valid accuracy for clinical use. In addition, GPR can evaluate the uncertainty of each estimate based on the similarity between datasets for learning and evaluation, and estimate vGRF deterministically as the size of the dataset increased, as shown in Figures 3.6 and 3.8. This could be beneficial for determining the reliability of the estimates in clinical diagnosis.

(2) Limitations

Similar to Section 2, robustness to abnormal plantar pressure distribution, the validity for walking on a softer floor at home, and the effect of asymmetrical upper body posture and specific upper limb motion on vGRF should be examined in future research.

3.4 Conclusion

This chapter described data-efficient one-step learning for the insole-based estimation of vGRF by measuring a minimum (just one) walking step, probabilistic data augmentation, and Gaussian process regression avoiding overfitting on a small dataset. In experiments, the data augmentation enhanced the estimation accuracy, and the GPR models learned from two walking steps estimated vGRF with valid accuracy for clinical use (under 12% for entire/local magnitudes). From the above, this study found that the proposed learning is beneficial for assessment in small clinics, where measuring multiple steps is difficult due to limitations to therapy time, fall risks, and physical burden on patients.

Chapter 4

Shift-adaptive Estimation of Joint Angle Using Instrumented Brace with Two Stretch Sensors

4.1 Chapter Overview

This chapter presents a *shift-adaptive estimation* to obtain the joint angle from a knee brace instrumented with stretch sensors. This method involves learning multiple models and performing adaptive estimation to changes in the relationship between the sensor strains and the joint angle due to the brace shift. The system induces changes in the relationship between the strains of the two stretch sensors, which are placed above and below the patella hole of the brace, utilizing biomechanics that the skin strain is high in the patella area and rapidly decreases further from the joint. The relationship between the two sensor strains and the joint angle at varying brace shift positions is then learned using user-specific GMMs. In the estimation, an ML GMM (i.e., the brace shift position) is identified by referring to the relationship between the two sensor strains. The angle is then calculated adaptively to the brace shift using the ML GMM.

4.2 Shift-adaptive Estimation of Knee Joint Angle

4.2.1 Instrumented Knee Brace with Two Stretch Sensors

The flow of shift-adaptive estimation of the knee joint angle is shown in Figure 4.1. First, an instrumented brace measuring the knee flexion/extension angle was developed, as shown in Figure 4.1(a). Flexion/extension is the primary movement of the knee joint and is informative

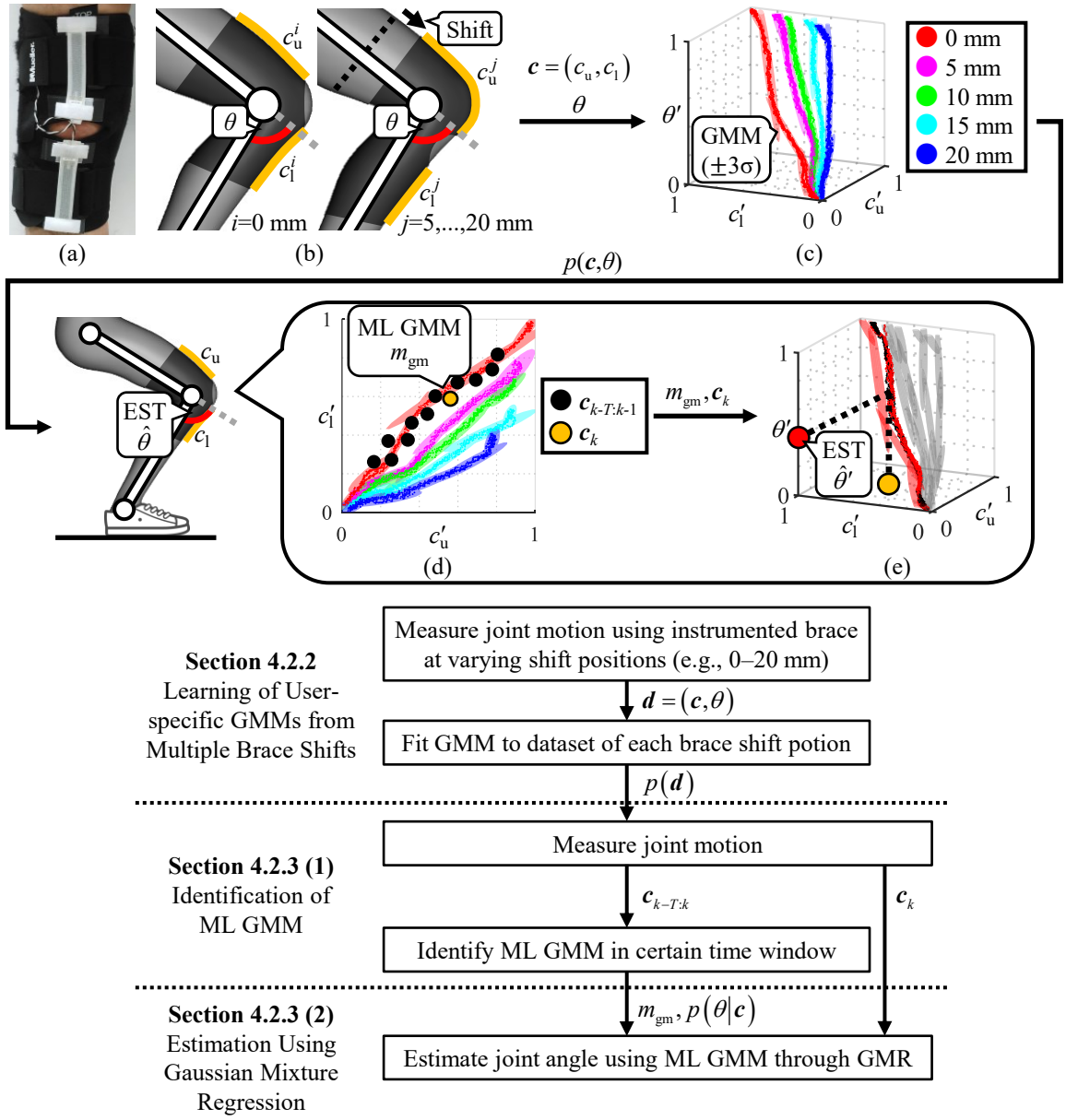

Figure 4.1. (Top) (a) A wrap-style brace is instrumented with two stretch sensors placed above and below the patella hole. (b) The capacitance (proportional to the sensor strain) decreases more significantly in the lower sensor than the upper sensor ($|c_l^i - c_l^j| > |c_u^i - c_u^j|$) at the same joint angle when the brace shifts downward. Consequently, the relationship between the two sensor capacitances and the joint angle varies depending on the brace shift position. (c) The system learns the different capacitance–angle relationships at varying brace shift positions using user-specific GMMs based on the iterative expectation-maximization (EM) algorithm with scaling to [0, 1] ($\boldsymbol{c}', \theta'$) and k-means clustering. (d) An ML GMM is identified by referring to the two sensor capacitances in a fixed time window. (e) The system estimates the joint angle adaptively to the brace shift through Gaussian mixture regression, using ML GMM and present sensor capacitances. (Bottom) Data flow of the shift-adaptive estimation of knee joint angle.

for monitoring a progressive joint disorder (e.g., osteoarthritis [2]). This study used a commercial wrap-style brace (Open Patella Knee Stabilizer, Mueller Sports Medicine, Wisconsin, US). This type of brace is easily donned/doffed, adjustable to achieve a comfortable restraint, and effective for the treatment of disorders associated with degenerative cartilage [104]. by stabilizing the patella [104].

Two electro capacitive stretch sensors (C-STRETCH®, Bando Chemical Industries, Kobe, JP) were placed above and below the patella hole of the brace. The sensor capacitance is proportional to the strain. The sensors installation is aimed at recognizing brace shifts by referring to the relationship between the two sensor capacitances while avoiding artifacts from the physical contact of the sensors and the skin. The mechanism of changes in the relationship between the two sensor capacitances is illustrated in Figure 4.1(b). The capacitance decreases more significantly in the lower sensor than the upper sensor at the same joint angle when the brace shifts downward. This is induced by the biomechanics that the skin strain is high in the patella area and rapidly decreases away from this region [105].

4.2.2 Learning of User-specific GMMs from Multiple Brace Shifts

The learning flow of user-specific GMMs is shown in Figure 4.1(b). First, a user wears the instrumented brace at the appropriate position on the knee. Next, the user performs knee flexion/extension (e.g., squatting) with the maximum executable range. The motions are measured by the brace in synchronization with the ground truth device. The measurement provides a dataset $\boldsymbol{d} \in \mathbb{R}^3$ consisting of the capacitance of the two stretch sensors $\boldsymbol{c} = (c_{\mathrm{u}}, c_{\mathrm{l}}) \in \mathbb{R}^2$ and the ground truth of the joint angle $\theta \in \mathbb{R}$. A GMM of L components is then fitted to the dataset $\boldsymbol{d}$ using the iterative expectation-maximization (EM) algorithm with scaling to [0, 1] $(\boldsymbol{c}', \theta')$ and k-means clustering. The model is defined as the following probability density function:

$$p\left(\boldsymbol{d}\right) = \sum_{l=1}^{L} \pi_l N\left(\boldsymbol{d}\,|\boldsymbol{\mu}_l, \boldsymbol{\Sigma_l}\right), \quad \sum_{l=1}^{L} \pi_l = 1 \tag{4.1}$$

$$N\left(\boldsymbol{d}|\boldsymbol{\mu}_l, \boldsymbol{\Sigma}_l\right) = \frac{1}{(2\pi)^{\frac{3}{2}}} \frac{1}{|\boldsymbol{\Sigma}_l|^{\frac{1}{2}}} \exp\left\{-\frac{1}{2}\left(\boldsymbol{d} - \boldsymbol{\mu}_l\right)^{\top} \boldsymbol{\Sigma}_l^{-1}\left(\boldsymbol{d} - \boldsymbol{\mu}_l\right)\right\} \tag{4.2}$$

where π_l indicates the prior probabilities and $N\left(\boldsymbol{z}\,|\boldsymbol{\mu}_l, \boldsymbol{\Sigma}_l\right)$ is the Gaussian distributions defined by the mean vector $\boldsymbol{\mu}_l$ and covariance matrix $\boldsymbol{\Sigma}_l$, whose components can be represented separately as follows:

$$\boldsymbol{\mu}_l = \begin{bmatrix} \boldsymbol{\mu}_{\boldsymbol{c},l} & \mu_{\theta,l} \end{bmatrix}, \quad \boldsymbol{\Sigma}_l = \begin{pmatrix} \boldsymbol{\Sigma}_{\boldsymbol{cc},l} & \boldsymbol{\Sigma}_{\boldsymbol{c}\theta,l} \\ \boldsymbol{\Sigma}_{\theta\boldsymbol{c},l} & \Sigma_{\theta\theta,l} \end{pmatrix} \tag{4.3}$$

Following collecting data at the appropriate position, the user migrates the brace to anticipated shift positions (e.g., every 5 mm up to 20 mm) and measure knee flexion/extension again. A GMM is fitted to the dataset of each shift position, and the GMMs at all shifts are then integrated with equal mixing proportions.

4.2.3 Shift-adaptive Estimation

(1) Identification of ML GMM

The system estimates the joint angle from the two sensor capacitances according to the brace shift, using the ML GMM identified from the integrated GMMs. This identification may be affected by the measurement error and sensor noise when the relationships between the two sensor capacitances of the GMMs proximate. Therefore, this study proposes to identify the ML GMM by referring to the two sensor capacitances in a fixed time window.

When given the capacitance of the two sensors $\boldsymbol{c}$, the probability of each component l of the integrated GMMs is defined as follows:

$$\beta_l = \frac{p\left(l\right)p\left(\boldsymbol{c}\left|l\right.\right)}{\sum_{i=1}^{n_{\mathrm{gm}}L} p\left(i\right)p\left(\boldsymbol{c}\left|i\right.\right)} = \frac{\pi_l p\left(\boldsymbol{c}\left|\boldsymbol{\mu}_{\boldsymbol{c},l},\boldsymbol{\Sigma}_{\boldsymbol{cc},l}\right.\right)}{\sum_{i=1}^{n_{\mathrm{gm}}L} \pi_i p\left(\boldsymbol{c}\left|\boldsymbol{\mu}_{\boldsymbol{c},i},\boldsymbol{\Sigma}_{\boldsymbol{cc},i}\right.\right)} \tag{4.4}$$

where n_{gm} is the number of learned GMMs (five in this study). Using β_l, the system identifies the ML GMM by referring to the summed probabilities of L components of each GMM averaged in a certain time window T as follows:

$$\begin{gathered}\arg\max_{m_{\mathrm{gm}}} \frac{1}{T}\sum_{i=k-T}^{k}\sum_{l=n_{\mathrm{gm}}(m_{\mathrm{gm}}-1)+1}^{n_{\mathrm{gm}}m_{\mathrm{gm}}} \beta_{l,m_{\mathrm{gm}}} \\ m_{\mathrm{gm}} = \left\{1,2,...,n_{\mathrm{gm}}\right\},\quad \hat{\theta}\left(i\right) < \theta_{\mathrm{ub}}\end{gathered} \tag{4.5}$$

where m_{gm} denotes each GMM and k is the last frame. The time window T includes only frames in which the estimated joint angle is lower than θ_{ub}. This condition aims to exclude datasets of larger joint angles when the sensor strains are close to the maximum, in which capacitances of the GMMs are proximate despite their differing angles.

(2) Estimation Using ML GMM through Gaussian Mixture Regression

Using the identified ML GMM, the system estimates the joint angle from the present two sensor capacitances through Gaussian mixture regression (GMR) [106]. GMR probabilistically blends the estimates of GMM components. For each component l of the GMM, the expected distribution

of joint angle $\hat{\theta}_l$ given the capacitances of the two stretch sensors $\boldsymbol{c}$ is defined as follows:

$$p\left(\theta \left| \boldsymbol{c}, l \right.\right) = N\left(\theta \left| \hat{\theta}_l, \hat{\Sigma}_{\theta\theta,l} \right.\right) \tag{4.6}$$

$$\hat{\theta}_l = \mu_{\theta,l} + \boldsymbol{\Sigma}_{\theta\boldsymbol{c},l}\left(\boldsymbol{\Sigma}_{\boldsymbol{cc},l}\right)^{-1}\left(\boldsymbol{c} - \boldsymbol{\mu}_{\boldsymbol{c},l}\right) \tag{4.7}$$

$$\hat{\Sigma}_{\theta\theta,l} = \Sigma_{\theta\theta,l} - \boldsymbol{\Sigma}_{\theta\boldsymbol{c},l}\left(\boldsymbol{\Sigma}_{\boldsymbol{cc},l}\right)^{-1}\boldsymbol{\Sigma}_{\boldsymbol{c}\theta,l} \tag{4.8}$$

By considering the complete GMM, the expected distribution is defined by

$$p\left(\theta \left| \boldsymbol{c} \right.\right) = \sum_{l=n_{\mathrm{gm}}(m_{\mathrm{gm}}-1)+1}^{n_{\mathrm{gm}}m_{\mathrm{gm}}} \beta_l N\left(\theta \left| \hat{\theta}_l, \hat{\Sigma}_{\theta\theta,l} \right.\right) \tag{4.9}$$

where $\beta_l = p\left(l \left| \boldsymbol{c} \right.\right)$ is the probability of the component l responsible for $\boldsymbol{c}$, i.e.,

$$\beta_l = \frac{p\left(l\right)p\left(\boldsymbol{c} \left| l \right.\right)}{\sum_{i=n_{\mathrm{gm}}(m_{\mathrm{gm}}-1)+1}^{n_{\mathrm{gm}}m_{\mathrm{gm}}} p\left(i\right)p\left(\boldsymbol{c} \left| i \right.\right)} = \frac{\pi_l p\left(\boldsymbol{c} \left| \mu_{\boldsymbol{c},l}, \Sigma_{\boldsymbol{cc},l} \right.\right)}{\sum_{i=n_{\mathrm{gm}}(m_{\mathrm{gm}}-1)+1}^{n_{\mathrm{gm}}m_{\mathrm{gm}}} \pi_i p\left(\boldsymbol{c} \left| \mu_{\boldsymbol{c},i}, \Sigma_{\boldsymbol{cc},i} \right.\right)} \tag{4.10}$$

Using the linear transformation properties of Gaussian distributions, an estimation of the conditional expectation of θ given $\boldsymbol{c}$ is defined as follows:

$$p\left(\theta \left| \boldsymbol{c} \right.\right) = N\left(\hat{\theta}, \hat{\Sigma}_{\theta\theta}\right) \tag{4.11}$$

where the parameters of the Gaussian distribution are defined as

$$\hat{\theta} = \sum_{l=n_{\mathrm{gm}}(m_{\mathrm{gm}}-1)+1}^{n_{\mathrm{gm}}m_{\mathrm{gm}}} \beta_l \hat{\theta}_l, \quad \hat{\Sigma}_{\theta\theta} = \sum_{l=n_{\mathrm{gm}}(m_{\mathrm{gm}}-1)+1}^{n_{\mathrm{gm}}m_{\mathrm{gm}}} \beta_l^2 \hat{\Sigma}_{\theta\theta,l} \tag{4.12}$$

4.3 Evaluation of Shift-adaptive Estimation

4.3.1 Experimental Setup

Two healthy adults (male, age: 26 ± 1 years, height: 1.78 ± 0.5 m, body mass: 64.5 ± 2.5 kg) were recruited for this study. The experiment was approved by Keio University Research Ethics Committee (reference number 31–80). Informed consent was obtained from the participants prior to the experiments. The participants wore the instrumented brace on their right knee at a comfortable tightness. Hard thin CEM-3 plates (95 × 72 × 1.6 mm) incorporating three infrared reflective markers were then tightly attached to the right thigh and shank. The positions of the plates were chosen such that upper/lower markers on the thigh/shank were located along a line connecting the greater trochanter and the ankle joint. The capacitance of the two stretch

sensors was amplified and DA-converted using a dedicated module (KIT BT01, Bando Chemical Industries, Hyogo, JP) placed on the brace. A data logger (TSND151, ATR Promotions, Kyoto, JP) on the thigh plate then AD-converted the voltage outputs of the module and transmitted them to a laptop computer at 200 Hz through Bluetooth communication. Additional markers sets were attached to the front of the thigh and shank and the upper/lower edges of the brace for measuring the distances of brace shifts. Landmark stickers representing a 5 mm spacing from 0 to 20 mm also adhered to the thigh and shank for manual brace shifting. The positions of the reflective markers on the thigh and shank were obtained by a motion capture system (Nexus, Vicon, Oxford, UK) at 100 Hz. All devices were synchronized using a voltage input.

4.3.2 Generation of Virtual Knee Joint Marker

The ground truth of the knee joint angle can be calculated as the angle between two vectors from the knee joint to the greater trochanter and the ankle joint. However, the motion capture marker could not be directly attached to the knee joint because of the knee brace. Therefore, a virtual knee joint marker was generated from three markers on the plates attached to the thigh and shank.

The marker generation was executed through an optimization inspired by a gap-filling algorithm [107]. The algorithm fills a target marker unobservable at an interpolation frame k_i using the positions of the target marker observable at a reference frame k_r and a rotation matrix of three reference markers from k_r to k_i. At the reference frame k_r and the interpolation frame k_i, the relative positions of the reference markers $\bar{\boldsymbol{M}}_{\mathrm{r/i}}$ to their center $\boldsymbol{O}\mathrm{r/i}$ are defined as follows:

$$\bar{\boldsymbol{M}}_{\mathrm{r/i}} = \boldsymbol{M}_{\mathrm{r/i}} - \boldsymbol{O}_{\mathrm{r/i}} = \boldsymbol{M}_{\mathrm{r/i}} - \frac{1}{3}\sum_{j=1}^{3} \boldsymbol{M}_{\mathrm{r/i}j} \tag{4.13}$$

A rotation matrix $\boldsymbol{R}_\mathrm{i}$ from k_r to k_i can be generated by calculating a covariance matrix $\boldsymbol{C}_\mathrm{i}$ and by applying a singular value decomposition using the Kabsch algorithm as follows:

$$\boldsymbol{C}_\mathrm{i} = \bar{\boldsymbol{M}}_\mathrm{r}^\top \bar{\boldsymbol{M}}_\mathrm{i} = \boldsymbol{U}\boldsymbol{S}\boldsymbol{V}^\top \tag{4.14}$$

$$\boldsymbol{R}_\mathrm{i} = \boldsymbol{V}\begin{bmatrix} 1 & 0 & 0 \\ 0 & 1 & 0 \\ 0 & 0 & b \end{bmatrix}\boldsymbol{U}^\top,\ b = \begin{cases} -1 & (\det(\boldsymbol{V}\boldsymbol{U}^\top) < 0) \\ 1 & (otherwise) \end{cases} \tag{4.15}$$

The target marker positions $\boldsymbol{P}_\mathrm{i}$ at k_i are then calculated using the rotation matrix $\boldsymbol{R}_\mathrm{i}$, the

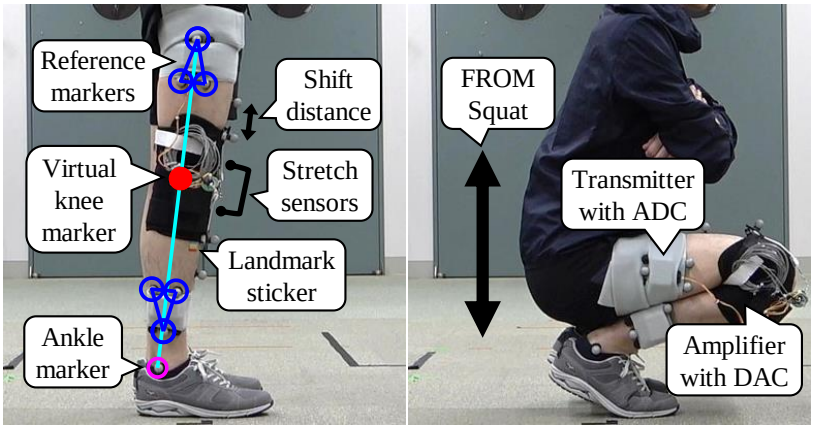

Figure 4.2. The participants were asked to perform two motions for each brace shift position. (a) Standing still for measuring brace shift distances. (b) FROM squat for generating a virtual knee joint marker shown in (a), learning the GMMs, and testing the estimation methods.

relative positions of the target marker at the reference frame $\bar{\boldsymbol{P}}_{\mathrm{r}}$, and $\boldsymbol{O}_{\mathrm{i}}$.

$$\begin{aligned} \boldsymbol{P}_{\mathrm{i}} &= \boldsymbol{R}_{\mathrm{i}}\bar{\boldsymbol{P}}_{\mathrm{r}} + \boldsymbol{O}_{\mathrm{i}} \\ &= \boldsymbol{R}_{\mathrm{i}}(\boldsymbol{P}_{\mathrm{r}} - \boldsymbol{O}_{\mathrm{r}}) + \boldsymbol{O}_{\mathrm{i}} \end{aligned} \tag{4.16}$$

Based on the above algorithm, the virtual knee joint marker positions $\boldsymbol{P}_{\mathrm{r}}$ were identified through a nonlinear optimization, that minimized the sum of the following two distances during knee flexion/extension. One was the error between the two virtual marker positions estimated from three reference marker sets on thigh and shank, respectively. The other was the distance from the upper marker on thigh to the lower marker on the shank through the virtual marker (assuming all markers to be located on the same plane). The optimization is defined as follows:

$$\min_{x} \|f(x)\|_2^2 = \min_{x} \left(f_1(x)^2 + f_2(x)^2 + \ldots + f_n(x)^2 \right) \tag{4.17}$$

$$\begin{aligned} f(\boldsymbol{P}_{\mathrm{r}}) =& \{\boldsymbol{R}_{\mathrm{i}}^{\mathrm{t}}(\boldsymbol{P}_{\mathrm{r}} - \boldsymbol{O}_{\mathrm{r}}^{\mathrm{t}}) + \boldsymbol{O}_{\mathrm{i}}^{\mathrm{t}}\} \\ &- \{\boldsymbol{R}_{\mathrm{i}}^{\mathrm{s}}(\boldsymbol{P}_{\mathrm{r}} - \boldsymbol{O}_{\mathrm{r}}^{\mathrm{s}}) + \boldsymbol{O}_{\mathrm{i}}^{\mathrm{s}}\} \\ &+ (\boldsymbol{P}_{\mathrm{r}} - \boldsymbol{O}_{\mathrm{r}}^{\mathrm{t}}) + (\boldsymbol{P}_{\mathrm{r}} - \boldsymbol{O}_{\mathrm{r}}^{\mathrm{s}}) \end{aligned} \tag{4.18}$$

where superscripts t and s indicate thigh and shank, respectively.

4.3.3 Study Procedure

To validate the shift-adaptive estimation of the knee joint angle, the participants were asked to perform the following tasks:

A. To generate the virtual knee joint marker, as shown in Figure 4.2(a), the participants performed a full range of motion (FROM) squat five times during a 20 s period.

B. To measure the brace position, the participants stood still for 10 s, as shown in Figure 4.2(a).

C. For the learning and testing of the proposed method, the participants performed a FROM squat five times within a 40 s period, as shown in Figure 4.2(b). During this motion, they took a 2 s rest after every squat-stand motion.

D. The participants migrated the brace manually to the anticipated shift positions (5, 10, 15, and 20 mm away from the initial position) according to the landmark stickers. They then repeated tasks B and C at each shift position.

E. The participants returned the brace to the initial position and repeated tasks B–D to reenact donning/doffing or position correction of the brace.

Tasks B–E indicate that standing still and the FROM squats were measured for two sets of brace shifts (every 5 mm from 0 to 20 mm) in total.

4.3.4 Data Analysis

(1) Preparation of Datasets for Learning and Testing

Using the marker positions obtained in task A, the virtual knee joint marker was generated through the optimization (4.17) using MATLAB Optimization Toolbox. The knee joint angle during the squat for tasks C–E was then calculated as the angle between two vectors, which are from the virtual knee joint marker to the upper marker on the thigh and the ankle marker. The AD-converted capacitances of the two stretch sensors were filtered by moving average with a time window of 20 ms for reducing noise and then resampled at 100 Hz to match the motion capture system.

The data sets consisting of the two sensor capacitances and the joint angle during the squat were then divided into the knee flexion (including rest) and extension motions by referring to the plus/minus sign of the derivative capacitance in the upper stretch sensor. This was aimed at modeling the capacitance–angle relationships, which differ between the stretch and relaxation owing to the different delay times for the capacitance-to-voltage conversion of the amplifier. The numerical differentiation was executed using the first-order derivatives and a moving average filter with a time window of 200 ms. All datasets were scaled to [0, 1] by referring to the measurement range for both sets of brace shifts, and then homogenized using a box grid filter.

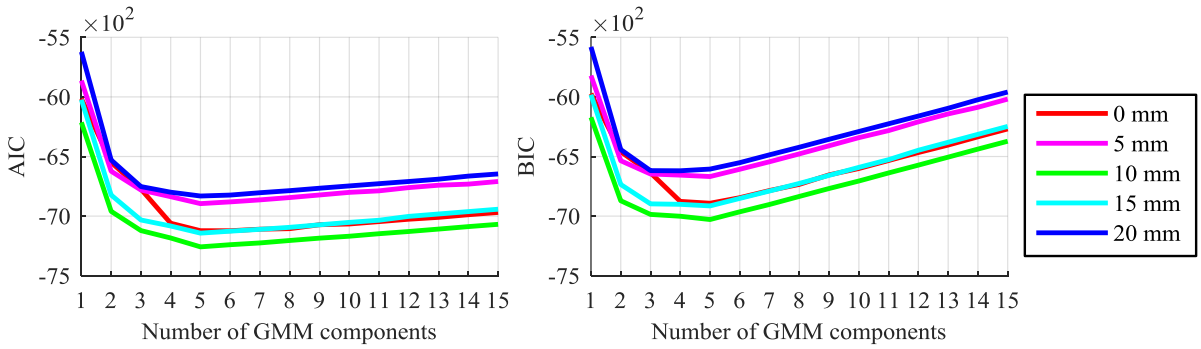

Figure 4.3. AIC and BIC for each number of GMM components.

(2) Training and Test of Proposed and Comparative Methods

Datasets of each brace shift set (every 5 mm from 0 to 20 mm) were used for training, and datasets of the other set were used for testing for cross-validation. For training, user-specific GMMs were fitted to the datasets of the five brace shift positions. The number of GMM components was set to five such that the AIC and BIC values were sufficiently small for the datasets of all shift positions, as shown in Figure 4.3. For testing, the proposed method estimated the joint angle of the datasets of each set using the GMMs trained by the other set. As described in Section 4.2.3, the ML GMM was identified by referring to the average probability of each GMM in a certain previous period of time. The time window T was set to 1 s, and the upper limit of data used for the identification was set to $\theta_{\mathrm{ub}} = 140°$. Using the identified ML GMM, the joint angle was estimated from the present two sensor capacitances through GMR. The estimation accuracy was evaluated using an RMSE during the test section, which excluded the first round of the squat as a sufficient period of time to identify the first ML GMM.

To assess the advantages of the proposed method using the previous ML model (PV), three comparative methods using the same datasets for learning and testing were examined as follows:

- Single Model (SM): The method learns the relationship between the two sensor capacitances and the joint angle at non-shift (0 mm) position as a single GMM.
- Single Sensor (SS): The method learns the relationships between only the upper sensor capacitance and the joint angle at five shift positions. The joint angle is estimated using the ML GMM identified by referring only to upper sensor capacitance.
- Present ML Model (PS): The method learns the relationships between the two sensor capacitances and the joint angle at five shift positions similar to PV. The joint angle is estimated using the ML GMM identified by referring to the present two sensor capacitances.

The effectiveness of the multiple shift models, multiple sensors, and the ML GMM in a fixed time

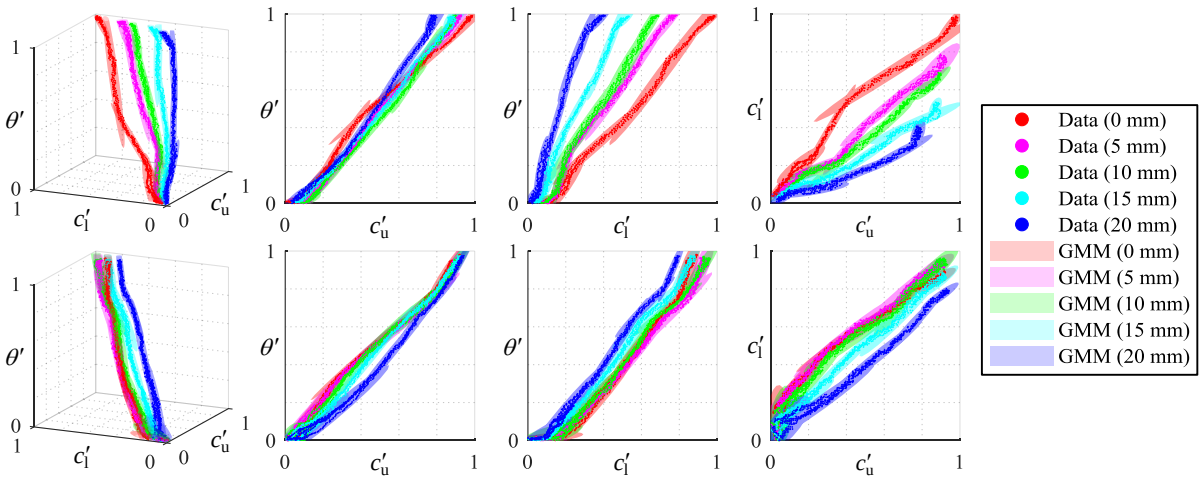

Figure 4.4. Relationships between the scaled capacitances of the two stretch sensors ($c'_{\mathrm{u}}, c'_{\mathrm{l}}$) and the joint angle θ', the same datasets plotted into each 2-D space, and the fitted GMMs ($\pm\, 3\sigma$) during knee extension at five brace shifts (0–20 mm) of the second set for both subjects A (top) and B (bottom).

window are assessed through comparisons between SM–PS, SS–PS, and PS–PV, respectively.

4.3.5 Results

The relationships between the scaled capacitances of the two stretch sensors and the joint angle during a knee extension at five brace shift positions, the same datasets plotted into each 2-D space, and the fitted GMMs are illustrated in Figure 4.4. The measured brace shift distances and the accuracy of the joint angles estimated by comparative and proposed methods during the squat motion are listed in Table 4.1. The method with the best performance at each shift position is highlighted in bold. The overall accuracy of PV at each shift position was evaluated by one-sample t-test. The null hypothesis was that the accuracy of the proposed method came from a population with a mean of 6.9°, against the alternative that the mean was under 6.9°. The criteria of 6.9° were chosen since its validity for capturing pathological gaits has been reported. This includes mild to moderate knee OA, which decreases maximum knee flexion angle by 6.9° in swing phase during walking [2]. The joint angles estimated by SS, PS, and PV, their absolute error, and ML models identified during two rounds of the squat motion are shown in Figure 4.5. The results are for two brace shift positions (5 and 20 mm) of the first set for both participants.

4.3.6 Discussion

(1) General Discussion

As illustrated in Figure 4.4, the relationship between the two sensor capacitances and the joint angle varied depending on the brace shift position. Specifically, the capacitance–angle relation-

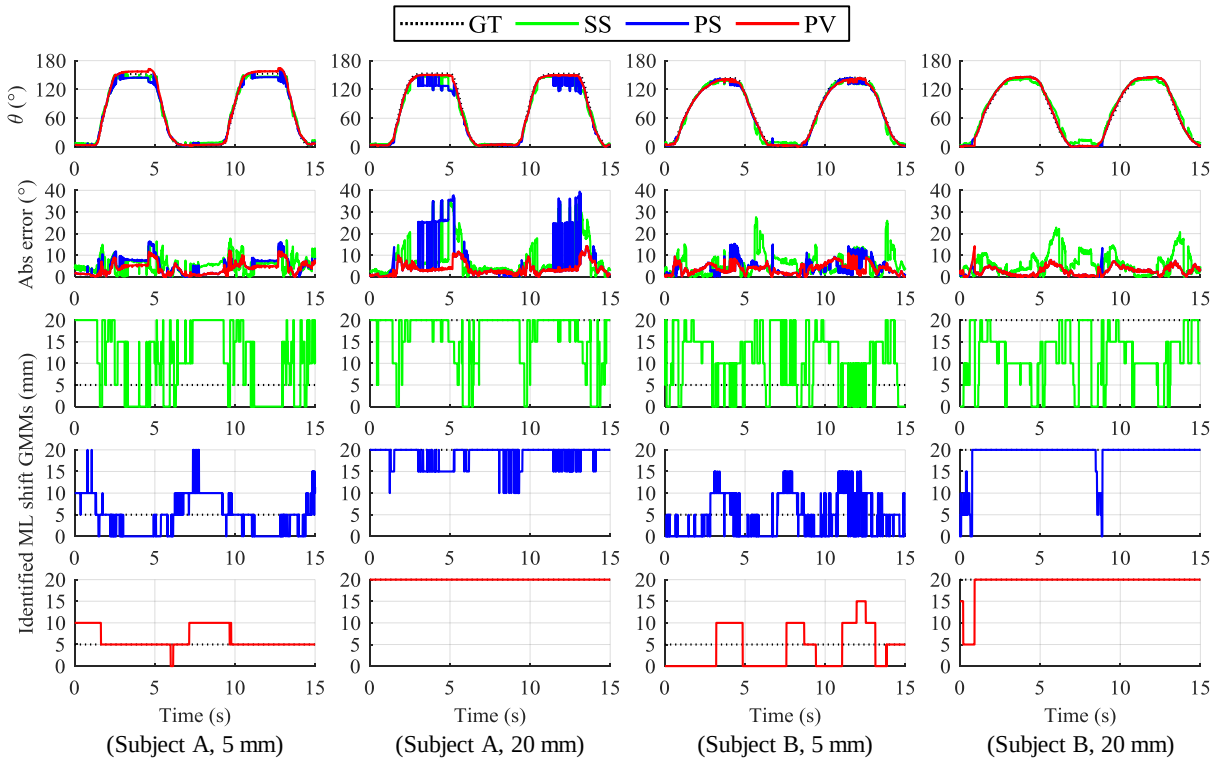

Figure 4.5. Ground truth of the joint angles (GT) and estimates of the comparative and proposed methods (SS, PS, PV) (top), their absolute error (the second row), and ML GMMs identified by each method during two rounds of the squat motion (the lower three). The results are for two brace shift positions (5 and 20 mm) of the first set for both subjects.

ship for each sensor changed according to the brace shift, and a more significant change in the lower sensor capacitance induced different relationships between the two sensor capacitances at varying shift positions. In addition, as indicated in Table 4.1, SM had lower accuracies at all brace shifts except for 0 mm of subject A when compared with PS. These results demonstrated that the learning of strain–angle relationships at multiple brace shift positions is required for the shift-adaptive estimation.

Table 4.1 also shows that SS had lower accuracies at most brace shifts when compared with PS. As shown in Figure 4.5, SS did not identify the correct ML GMM according to the brace shift even at larger joint angles, in which the relationship between two sensor capacitances clearly differed between GMMs, as shown in Figure 4.4. These results demonstrated that the two sensors placed above and below the patella hole are essential for recognizing the brace positions by identifying the correct GMM. From Table 4.1, PV exhibited an equivalent or higher performance to that of PS at most shift positions. As shown in Figure 4.5, PS switched the ML GMM frequently and decreased the accuracy due to the incorrect identification when the angle was close to the maximum. The switching of PS was due to the sensor noise and the proximity of the sensor capacitances between the GMMs near the maximum flexion angle, as shown in

Table 4.1. Brace shifts and RMSE of estimated knee joint angle.

ID (Set)	Brace shift (mm)		RMSE of knee angle (°)				t-test for PV	
	Target	Measured	SM	SS	PS	PV	p	$1-\beta$
A (1st)	0	–	**3.7**	4.5	**3.7**	**3.7**		
	5	8.8	6.3	6.7	5.9	**4.7**		
	10	13.2	10.3	7.4	**3.2**	4.2		
	15	17.6	15.0	5.8	4.4	**4.2**		
	20	26.9	23.6	9.7	10.5	**4.0**		
A (2nd)	0	2.9	**2.7**	4.6	5.0	3.1		
	5	10.3	19.6	4.3	**2.7**	3.2		
	10	18.0	36.0	4.9	4.1	**3.9**		
	15	19.1	39.3	6.3	5.4	**3.5**		
	20	29.9	23.9	9.3	4.0	**3.7**		
B (1st)	0	–	10.4	7.6	6.1	**5.8**		
	5	1.3	5.9	7.7	5.3	**4.8**		
	10	6.9	6.6	6.0	3.9	**3.2**		
	15	12.4	12.7	5.8	5.7	**3.1**		
	20	18.2	17.0	8.3	**3.3**	3.4		
B (2nd)	0	0.0	7.8	7.6	6.7	**6.5**		
	5	2.5	7.6	7.5	**5.9**	6.7		
	10	6.2	6.1	6.7	3.5	**2.8**		
	15	10.3	4.7	6.7	2.9	**2.8**		
	20	19.4	7.0	7.2	3.0	**2.9**		
Mean (± SD)	0	1.5 (2.1)	6.1 (4.2)	6.1 (2.2)	5.4 (1.4)	**4.8 (1.9)**	0.181	0.196
	5	5.7 (5.4)	9.8 (4.4)	6.6 (1.5)	**4.9 (0.9)**	**4.9 (1.3)**	0.131	0.281
	10	11.1 (6.4)	14.7 (11.9)	6.3 (0.1)	3.7 (0.1)	**3.5 (0.8)**	0.050	0.675
	15	14.8 (5.1)	17.9 (13.0)	6.2 (0.1)	4.6 (0.4)	**3.4 (0.6)**	0.041	0.769
	20	23.6 (6.8)	17.9 (8.4)	8.6 (1.2)	5.2 (2.9)	**3.5 (0.5)**	0.031	0.895

Figure 4.4. In contrast to PS, PV showed higher performance through stable identification of the correct ML GMM. These results indicate that identification of the ML GMM by referring to the two sensor capacitances in a fixed time window except for near the maximum angle enhances the estimation.

From the above results, it is found that the proposed method can estimate the joint angle with higher accuracy than previous methods when the brace shifts downward, and the three components are effective for the shift-adaptive estimation.

(2) Limitations

The t-test for PV provided strong statistical support only for the result at 20 mm ($p < 0.05$ and $1-\beta > 0.8$). Thus, the statistical validity of the proposed method at varying shift positions must be examined in future research with more participants. In addition, this study focused on flexion/extension as the dominant knee joint motion and adaptation to the distal brace shift as a common problem due to these motions. Meanwhile, the brace may rotate slightly in the horizontal plane owing to the rotation of the ankle joint or the donning/doffing of the brace.

Thus, future work should examine the applicability of the proposed method to joint motion around other axes and a rotational shift. Finally, although the time window for identifying ML GMM was set to 1 s, assuming sit-to-stand and walking, the window size should be adjusted according to the speed of the target motion because the brace shift may occur suddenly during fast motion.

4.4 Conclusion

This chapter presented the shift-adaptive estimation of the knee joint angle by combining the following: (i) a brace instrumented with two stretch sensors placed above and below the patella hole, (ii) learning the strain–angle relationships at multiple brace shift positions using user-specific GMMs, and (iii) estimation using an ML GMM in a previous 1 s period. Especially in (ii), changes in the relationship between two sensor strains utilized the biomechanics that the skin strain is high in the patella area and rapidly decreases further from the joint. Experimental results indicated that the proposed method estimates the joint angle at multiple shift positions (0–20 mm) with higher accuracy than methods using a single model, single sensor, or referring to the present sensor strains.

Chapter 5

Learning-based Occlusion Compensation for Leg Tracking Based on Fusion of Laser Range Sensor and Instrumented Insoles

5.1 Chapter Overview

Chapter 5 presents a *learning-based occlusion compensation* for leg position based upon the interlimb coordination for one walking cycle. This facilitates LRS-based tracking of both legs' complicated dynamic motions during walking on circular paths. The system measures straight walking and turning under different curvatures/directions in advance, and then learns the relationship between the trajectory and traveling direction of each leg during one cycle of each walking type using user-specific GMMs. In the tracking, the walking type is identified by a joint probability of both legs' trajectories during the walking cycle, in accordance with the biomechanics that both legs move in a coordinated manner. The ML GMM then estimates the traveling direction and position of the hidden leg during occlusion.

5.2 Learning-based Occlusion Compensation for Leg Tracking

5.2.1 Sensor Configuration

An overview of the measurement system is depicted in Figure 5.1. The system consists of the LRS (UST-10LX, Hokuyo Automatic Co., Osaka, JP) and the instrumented insoles using 15 force

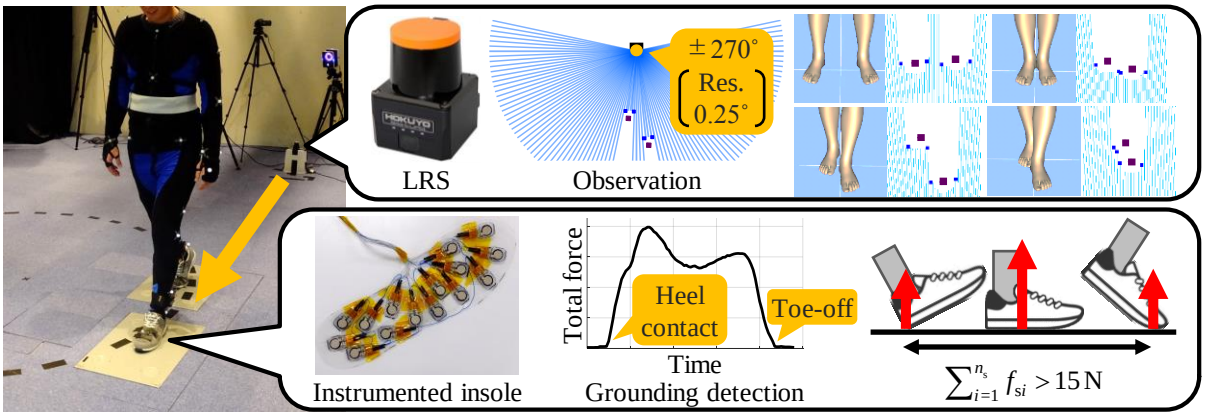

Figure 5.1. The measurement system consists of an LRS and the insoles instrumented with 15 force sensors. The LRS captures distance data over 270° of a horizontal plane at shin height, with a resolution of 0.25°. The insole detects each foot as grounded when the total force exceeds 15 N.

sensors (as described in Chapter 2). The LRS captures distance data over 270° of a horizontal plane at shin height (270 mm above the floor), with a resolution of 0.25°. The scanning speed is 25 ms (40 Hz) per round. The system then observes candidate positions of both legs from the distance data using geometrical observation patterns (as described in [66]). The instrumented insoles are inserted into the shoes of the subject and measure force applied to each sensor at 100 Hz. The insole detects each foot as being grounded when the total force exceeds the threshold, expressed as follows:

$$\sum_{i=1}^{n_s} f_{si} > 15 \text{ N} \tag{5.1}$$

where n_s is the number of insole force sensors, f_{si} is the measured force of each sensor. The threshold was set to 15 N, taking into account the sensitivity of the force sensors and their experimental noise. The LRS and insoles were synchronized through Ethernet cables and radio communications.

5.2.2 Pre-measurement Using Two LRSs without Occlusion

The flow of the leg tracking system with learning-based occlusion compensation is illustrated in Figures 5.2 and 5.3. The system tracks both legs in advance for straight walking and turning under different curvatures/directions. The measurement environment assumes that two LRSs (without occlusion) are available. The LRSs are installed facing each other and 6 m apart. The observations of both LRSs are merged through weighted averaging using the inverse distance from the sensor to the observation.

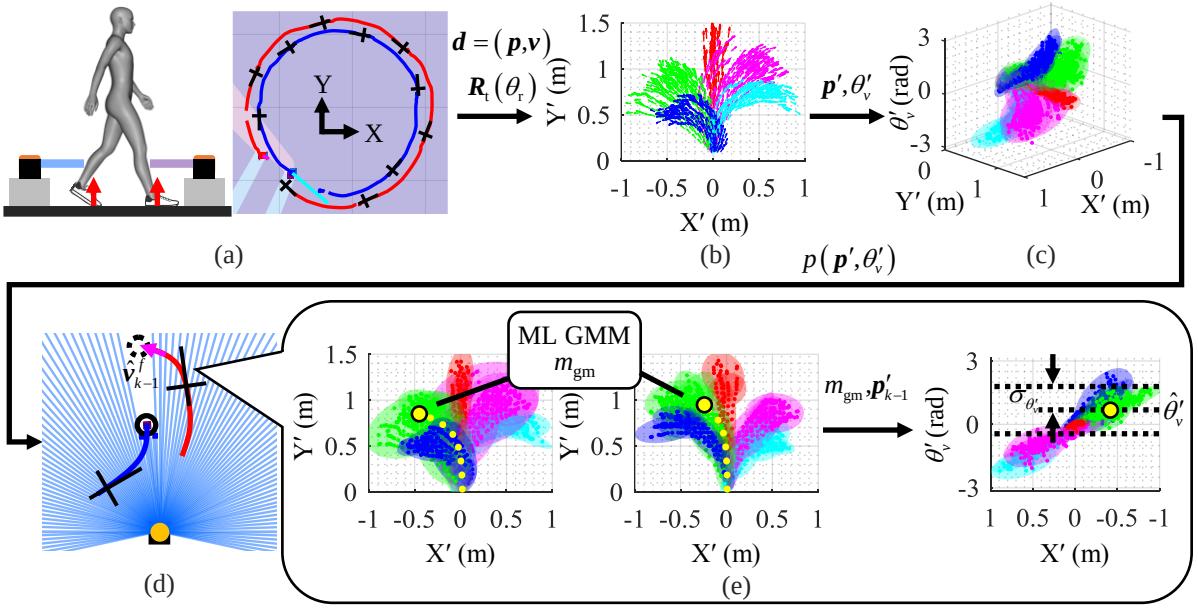

Figure 5.2. Flow of the leg tracking system with learning-based occlusion compensation: (a) The system tracks both legs during straight walking and turning under different curvatures/directions in advance, using two LRSs (without occlusion). (b) The time-series data of positions and velocities are divided by the walking cycle and transformed into a unified coordinate system. (c) The relationship between the leg trajectory and traveling direction during one walking cycle is modeled using the user-specific GMM for each walking type. (d) After learning the trajectory–direction relationships, the system tracks legs using only a single LRS and executes GMM-based compensation when occlusion occurs after the fifth step of the swing phase. (e) For occlusion compensation, the system identifies the ML GMM using the joint probabilities for the trajectories of both legs in accordance with interlimb coordination, and then estimates the traveling direction of the hidden leg at $k-1$.

(1) Gait Phase Detection

The system tracks both legs using the merged observations of the two LRSs in combination with the insole data. First, the gait phase [comprising stance and swing phases with acceleration/deceleration, as illustrated in Figure 5.4(a)] is identified for each leg. The stance/swing phase is identified by detecting foot grounding using the insole. The acceleration/deceleration of the swing phase is determined from the sign of the inner product between (i) the relative position vector from each leg to the opposite leg and (ii) the velocity vector of the target leg [66]. For example, the acceleration/deceleration of the left leg during the swing phase at discrete time step $k-1$ is calculated from the inner product as

$$(\boldsymbol{p}_{k-1}^{\mathrm{R}} - \boldsymbol{p}_{k-1}^{\mathrm{L}}) \cdot \boldsymbol{v}_{k-1}^{\mathrm{L}} \tag{5.2}$$

where $(\boldsymbol{p}_{k-1}^{\mathrm{R}} - \boldsymbol{p}_{k-1}^{\mathrm{L}})$ is the relative position vector of the right leg with respect to the left leg, and $\boldsymbol{v}_{k-1}^{\mathrm{L}}$ is the velocity vector of the left leg. As shown in Figure 5.4(b), the left leg accelerates when the inner product is positive and decelerates otherwise.

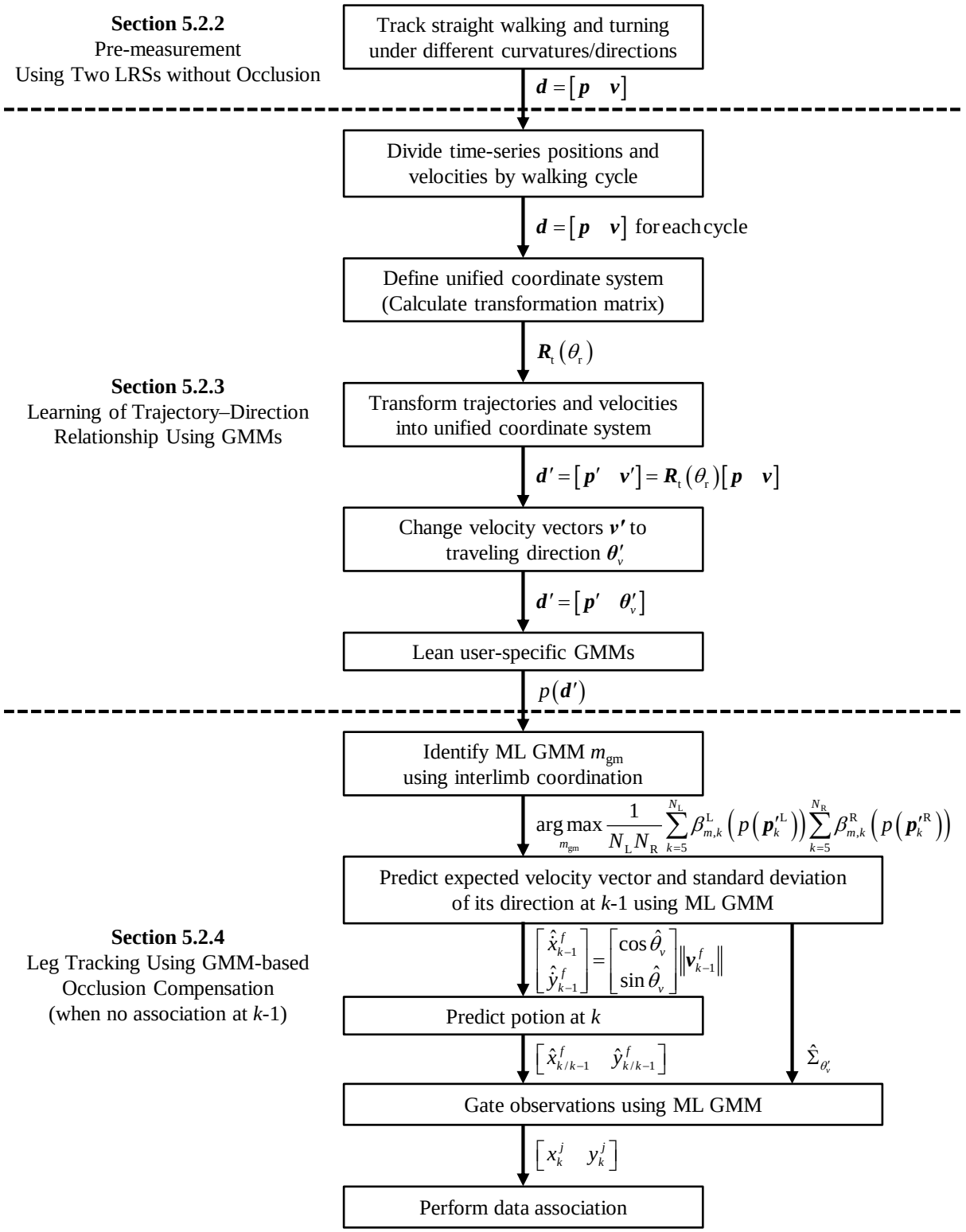

Figure 5.3. Data flow of the leg tracking system with learning-based occlusion compensation.

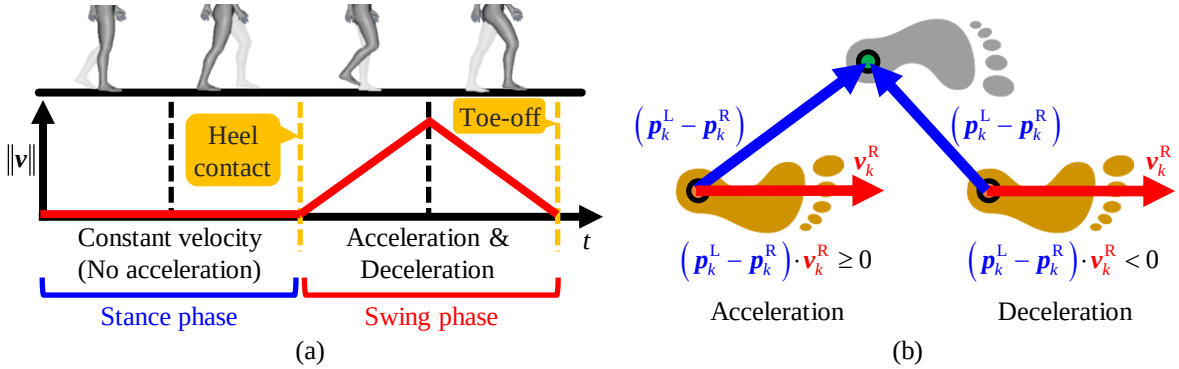

Figure 5.4. (a) Gait phase consisting of stance and swing phases with acceleration/deceleration. The stance/swing phases are recognized by detecting foot grounding using the insole. (b) The acceleration/deceleration of the swing phase is determined from the sign of the inner product between (i) the relative position vector from each leg to the opposite leg and (ii) the velocity vector of the target leg.

(2) Prediction of Leg Positions

The positions and velocities of both legs at the subsequent discrete time step k are predicted using a linear Kalman filter under the assumption of constant translational acceleration. The discrete motion model is given as

$$\boldsymbol{x}_k^f = \boldsymbol{A}\boldsymbol{x}_{k-1}^f + \boldsymbol{B}_\mathrm{u}\boldsymbol{u}_{k-1}^{f,p_\mathrm{g}} + \boldsymbol{B}\Delta\boldsymbol{x}_{k-1}^f \ (f = \mathrm{L,R}) \tag{5.3}$$

$$\boldsymbol{A} = \begin{bmatrix} 1 & 0 & \Delta t & 0 \\ 0 & 1 & 0 & \Delta t \\ 0 & 0 & 1 & 0 \\ 0 & 0 & 0 & 1 \end{bmatrix}, \ \boldsymbol{B}_\mathrm{u} = \boldsymbol{B} = \begin{bmatrix} \Delta t^2/2 & 0 \\ 0 & \Delta t^2/2 \\ \Delta t & 0 \\ 0 & \Delta t \end{bmatrix} \tag{5.4}$$

$$\boldsymbol{u}_k^{f,1} = \boldsymbol{0}, \ \ \boldsymbol{u}_k^{f,2} = g_{k-1}^f \frac{\boldsymbol{v}_{k-1}^f}{\left\|\boldsymbol{v}_{k-1}^f\right\|}, \ \ \boldsymbol{u}_k^{f,3} = -g_{k-1}^f \frac{\boldsymbol{v}_{k-1}^f}{\left\|\boldsymbol{v}_{k-1}^f\right\|} \tag{5.5}$$

where $\boldsymbol{x}_k^f = [\ \boldsymbol{p}_k^{f\top} \quad \boldsymbol{v}_k^{f\top}\ ] = [\ x_k^f \quad y_k^f \quad \dot{x}_k^f \quad \dot{y}_k^f\ ]^\top$ is predicted position and velocity of the leg, Δt is the sampling time, and $f = \mathrm{L,R}$ specifies the L/R leg. $\boldsymbol{u}_k^{f,m} = [\ \ddot{x}_k^{f,p_\mathrm{g}} \quad \ddot{y}_k^{f,p_\mathrm{g}}\ ]^\top (p_\mathrm{g} = 1,2,3)$ is the legs' acceleration input vector, which corresponds to their gait phase (e.g., $p_\mathrm{g} = 1$ is the stance phase, and $p_\mathrm{g} = 2,3$ are the acceleration/deceleration stages of the swing phase, respectively). g_k^f is the average norm of the acceleration vectors $(\Delta v_{x,k}^f/\Delta t, \Delta v_{y,k}^f/\Delta t) := \boldsymbol{a}_k^f$ for the swing leg during the last 20 time steps (0.5 s). $\Delta\boldsymbol{x}_k^f = [\ n^{\ddot{x}_k} \quad n^{\ddot{y}_k}\ ]^\top$ is the acceleration disturbance vector assuming a modeling error, which has zero mean and a white noise sequence with covariance $\boldsymbol{Q}$. This study proposes to change the covariance $\boldsymbol{Q}$ according to the gait phase

(by assuming that the modeling error reduces when the leg is in the stance phase) as follows:

$$\boldsymbol{Q} = \begin{cases} \mathrm{diag}\left(16.0^2, 16.0^2\right) & (\textit{Swing phase}) \\ \mathrm{diag}\left(4.0^2, 4.0^2\right) & (\textit{Stance phase}) \end{cases} \tag{5.6}$$

The measurement model is expressed as

$$\boldsymbol{y}_k^f = \boldsymbol{C}\boldsymbol{x}_k^f + \boldsymbol{w} \tag{5.7}$$

$$\boldsymbol{C} = \begin{bmatrix} 1 & 0 & 0 & 0 \\ 0 & 1 & 0 & 0 \end{bmatrix} \tag{5.8}$$

where $\boldsymbol{w}_k = \begin{bmatrix} n^{x_k} & n^{y_k} \end{bmatrix}^\top$ is the measurement noise, which is assumed to have a zero mean and a white noise sequence with covariance $\boldsymbol{R}$. The value was set to $\boldsymbol{R} = \mathrm{diag}(0.04^2, 0.04^2)$, in consideration of the measurement accuracy of the LRS.

Using the aforementioned motion model, the system predicts the position and velocity of both legs as

$$\hat{\boldsymbol{y}}_{k/k-1}^f = \boldsymbol{C}\hat{\boldsymbol{x}}_{k/k-1}^f = \boldsymbol{C}\left(\boldsymbol{A}\hat{\boldsymbol{x}}_{k-1/k-1}^f + \boldsymbol{B}_u\boldsymbol{u}_{k-1}^f\right) \tag{5.9}$$

where $\hat{\boldsymbol{y}}_{k/k-1}^f$ is the predicted position of the leg, and $\hat{\boldsymbol{x}}_{k/k-1}^f$ and $\hat{\boldsymbol{x}}_{k-1/k-1}^f$ express the *a priori* state estimate at time step k and *a posteriori* state estimate at $k-1$, respectively. The *a priori* covariance matrix $\boldsymbol{P}_{k/k-1}^f$ is then calculated as

$$\boldsymbol{P}_{k/k-1}^f = \boldsymbol{A}\boldsymbol{P}_{k-1/k-1}^f\boldsymbol{A}^\top + \boldsymbol{Q}\boldsymbol{B}\boldsymbol{Q}^\top \tag{5.10}$$

where $\boldsymbol{P}_{k-1/k-1}^f$ is the *a posteriori* covariance matrix at $k-1$.

(3) Gating and Data Association

After predicting the positions of the tracked legs and collecting observations, the system generates observation-to-track associations using the gating approach and GNN algorithm. The gating approach constructs a validation region around the predicted position of each leg $\hat{\boldsymbol{y}}_{k/k-1}^f$ and excludes all observations outside this region to prevent undesired associations. This region is defined as a threshold λ on the relation between the prediction $\hat{\boldsymbol{y}}_{k/k-1}^f$ and the j-th observation $\boldsymbol{y}_k^j$, which is calculated as the Mahalanobis distance $d_{f,j}$, expressed as

$$d_{f,j} = \begin{cases} \sqrt{\left(\boldsymbol{y}_k^j - \hat{\boldsymbol{y}}_{k/k-1}^f\right)^\top \left(\boldsymbol{S}_k^f\right)^{-1} \left(\boldsymbol{y}_k^j - \hat{\boldsymbol{y}}_{k/k-1}^f\right)} & (d_{f,j}^2 < \lambda) \\ \infty & (\textit{otherwise}) \end{cases} \tag{5.11}$$

where $\boldsymbol{S}_k^f$ is the covariance matrix of the innovation $\boldsymbol{y}_k^j - \hat{\boldsymbol{y}}_{k/k-1}^f$ calculated as follows:

$$\boldsymbol{S}_k^f = \boldsymbol{C}\boldsymbol{P}_{k/k-1}^f \boldsymbol{C}^\top + \boldsymbol{R} \tag{5.12}$$

The threshold is set to $\lambda = 13.82$ according to the probability $P_\mathrm{G} = 0.999$ (extracted from the χ^2 distribution with two degrees of freedom) that an observation generated by the leg is located inside the region.

The GNN then assigns each included observation to a maximum of one leg, by minimizing a cost function $c_{a,b}$ expressed as the sum of the Mahalanobis distances for each leg:

$$c_{a,b} = d_{\mathrm{L},a} + d_{\mathrm{R},b} \ (0 \leq a \leq J_k, 0 \leq b \leq J_k, a \neq b) \tag{5.13}$$

where J_k is the total number of observations at k.

(4) Filtering

When the observation corresponding to the predicted position is found, the system performs a filtering process using a Kalman filter. The *a posteriori* state estimate $\hat{\boldsymbol{x}}_k^f$ and Kalman gain $\boldsymbol{K}_k^f$ are calculated as follows:

$$\hat{\boldsymbol{x}}_{k/k}^f = \hat{\boldsymbol{x}}_{k/k-1}^f + \boldsymbol{K}_k^f \left(\boldsymbol{y}_k^f - \boldsymbol{C}\hat{\boldsymbol{x}}_{k/k-1}^f \right) \tag{5.14}$$

$$\boldsymbol{K}_k^f = \boldsymbol{P}_{k/k-1}^f \boldsymbol{C}^\top \left(\boldsymbol{C}\boldsymbol{P}_{k/k-1}^f \boldsymbol{C}^\top + \boldsymbol{R} \right)^{-1} \tag{5.15}$$

The *a posteriori* covariance matrix $\boldsymbol{P}_{k/k}^f$ is then calculated as follows:

$$\boldsymbol{P}_{k/k}^f = \left(\boldsymbol{I} - \boldsymbol{K}_k^f \boldsymbol{C} \right) \boldsymbol{P}_{k/k-1}^f \tag{5.16}$$

If the corresponding observation is not found (owing to occlusion), the filtering process is suppressed and the *a posteriori* state estimate and covariance matrix are set to the *a priori* ones.

Applying the above process to the fusion of the two LRSs and instrumented insoles allows the system to track both legs during straight walking and turning under different curvatures/directions.

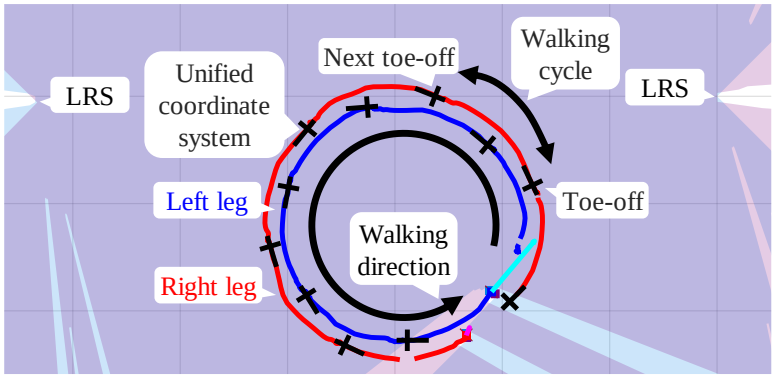

Figure 5.5. The time-series positions and velocities of each leg are divided by the walking cycle, which lasts from the start of one swing phase (toe-off) to the start of the next, as identified by the insole.

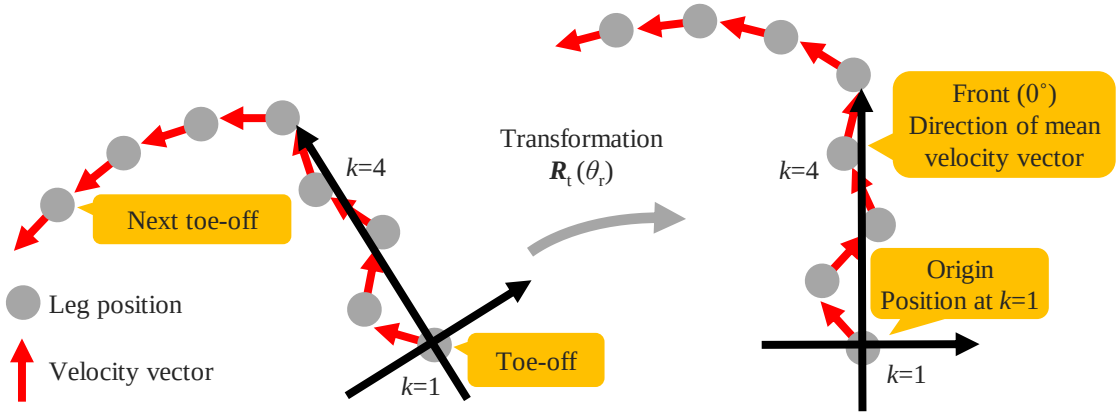

Figure 5.6. Definition of unified coordinate system. The origin denotes the leg position at the first time step, and the front-facing (0°) direction is set as the mean velocity vector's orientation for the four initial steps.

5.2.3 Learning of Trajectory–Direction Relationship Using GMMs

(1) Division of Time-series Positions and Velocities into Walking Cycle

After tracking different walking types, the relationship between the leg trajectory and traveling direction for one walking cycle is modeled for each type. First, the time-series positions and velocities of each leg are divided by the walking cycle, which lasts from the start of one swing phase to the start of the next (depicted in Figure 5.5), as identified by the insole.

(2) Transformation into Unified Coordinate System

Next, the unified coordinate system (shown in Figure 5.6) is defined for each cycle. The origin of the coordinate system is the leg's position at the first time step, and the front-facing (0°) direction is set as the mean velocity vector's orientation for the four initial steps (0.1 s). The

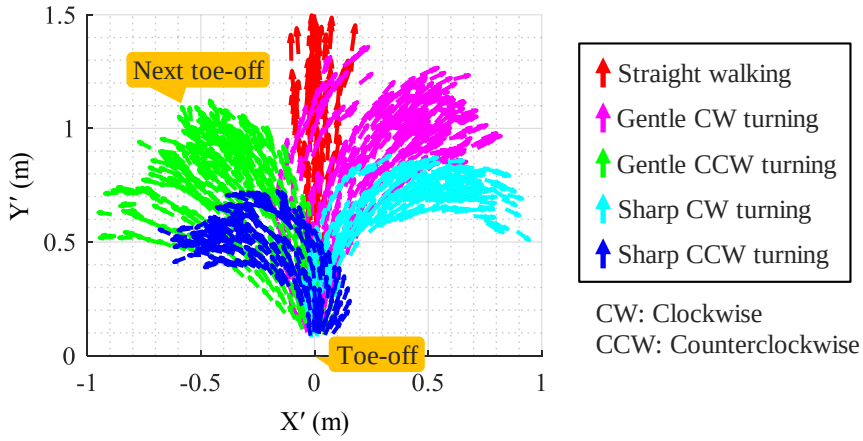

Figure 5.7. The positions and velocities after the fifth step are transformed into a unified coordinate system, and the traveling directions are calculated as the directions of the transformed velocity vectors.

transformation matrix is defined as follows:

$$\boldsymbol{R}_{\mathrm{t}}\left(\theta_{\mathrm{r}}\right)=\begin{bmatrix}\cos\theta_{\mathrm{r}} & -\sin\theta_{\mathrm{r}} & -p_{x,1}\\ \sin\theta_{\mathrm{r}} & \cos\theta_{\mathrm{r}} & -p_{y,1}\\ 0 & 0 & 1\end{bmatrix} \tag{5.17}$$

$$\theta_{\mathrm{r}}=\frac{\pi}{2}-\frac{1}{4}\sum_{k=1}^{4}\tan^{-1}\frac{v_{y,k}}{v_{x,k}} \tag{5.18}$$

The time-series positions and velocities after the fifth step are then transformed into a unified coordinate system, and the traveling directions are calculated as the direction of the transformed velocity vectors.

Through these processes, datasets describing the transformed leg's position $\boldsymbol{p}'$ and traveling direction θ'_v are obtained for each walking type, as shown in Figure 5.7.

(3) Fitting of User-specific GMMs

To model the relationship between the leg trajectory and the traveling direction for each walking type, the user-specific GMM is fitted to the transformed dataset $\boldsymbol{d}'=(\boldsymbol{p}',\theta'_v)$ using the EM algorithm, as demonstrated in Figure 5.8. The probability density function is described as

$$p(\boldsymbol{d}')=\sum_{l=1}^{L}\pi_l N\left(\boldsymbol{d}'|\boldsymbol{\mu}_l,\boldsymbol{\Sigma}_l\right)=\sum_{l=1}^{L}\pi_l N\left(\begin{bmatrix}\boldsymbol{p}' & \theta'_v\end{bmatrix}\middle|\begin{bmatrix}\boldsymbol{\mu}_{\boldsymbol{p}',l} & \mu_{\theta'_v,l}\end{bmatrix},\begin{bmatrix}\boldsymbol{\Sigma}_{\boldsymbol{p}'\boldsymbol{p}',l} & \boldsymbol{\Sigma}_{\theta'_v\boldsymbol{p}',l}\\ \boldsymbol{\Sigma}_{\boldsymbol{p}'\theta'_v,l} & \Sigma_{\theta'_v\theta'_v,l}\end{bmatrix}\right) \tag{5.19}$$

$$N\left(\boldsymbol{d}'|\boldsymbol{\mu}_l,\boldsymbol{\Sigma}_l\right)=\frac{1}{(2\pi)^{\frac{3}{2}}}\frac{1}{|\boldsymbol{\Sigma}_l|^{\frac{1}{2}}}\exp\left\{-\frac{1}{2}\left(\boldsymbol{d}'-\boldsymbol{\mu}_l\right)^{\top}\boldsymbol{\Sigma}_l^{-1}\left(\boldsymbol{d}'-\boldsymbol{\mu}_l\right)\right\} \tag{5.20}$$

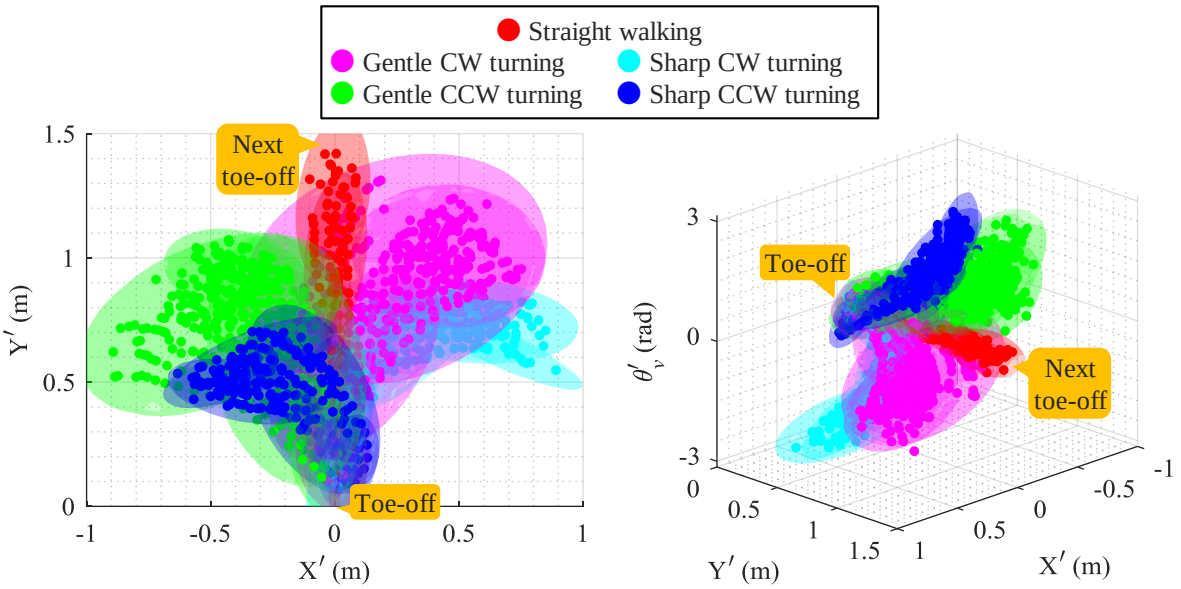

Figure 5.8. The relationships between the leg trajectory and traveling direction for straight walking and turning under different curvatures/directions are modeled by user-specific GMMs.

where L is the number of GMM components.

5.2.4 GMM-based Occlusion Compensation

After learning the trajectory–direction relationships, the system tracks legs using a single LRS and the insole data. Tracking is performed according to Section 5.2.2(1)–(4), and the compensation is executed when occlusion arises after the fifth step of the swing phase. Occlusion is defined as occurring when no observation is associated with the leg at $k-1$. The occlusion compensation procedure is described below.

(1) Identification of ML GMM based on Interlimb Coordination

The trajectories from the fifth step of the swing phase to the $k-1$ time step (for both legs) are transformed into the unified coordinate systems. Given the transformed leg position $\boldsymbol{p}'$, the probability of the GMM for each walking type m_{gm} is calculated as

$$\beta_{\mathrm{gm}} = \sum_{l=n_{\mathrm{gm}}(m_{\mathrm{gm}}-1)+1}^{n_{\mathrm{gm}}m_{\mathrm{gm}}} \beta_l \tag{5.21}$$

$$\beta_l = \frac{p(l)\,p(\boldsymbol{p}'\,|l)}{\sum_{i=1}^{n_{\mathrm{gm}}L} p(i)\,p(\boldsymbol{p}'\,|i)} = \frac{\pi_l p\left(\boldsymbol{p}'\,\middle|\boldsymbol{\mu}_{\boldsymbol{p}',l}, \boldsymbol{\Sigma}_{\boldsymbol{p}'\boldsymbol{p}',l}\right)}{\sum_{i=1}^{n_{\mathrm{gm}}L} \pi_i p\left(\boldsymbol{p}'\,\middle|\boldsymbol{\mu}_{\boldsymbol{p}',i}, \boldsymbol{\Sigma}_{\boldsymbol{p}'\boldsymbol{p}',i}\right)} \tag{5.22}$$

where n_{gm} is the number of walking types. The ML GMM, which maximizes the joint probability of bot legs' trajectories, is then defined as follow:

$$\arg\max_{m_{\mathrm{gm}}} \frac{1}{N_{\mathrm{L}} N_{\mathrm{R}}} \sum_{k=5}^{N_{\mathrm{L}}} \beta^{\mathrm{L}}_{m_{\mathrm{gm}},k} \sum_{k=5}^{N_{\mathrm{R}}} \beta^{\mathrm{R}}_{m_{\mathrm{gm}},k} \quad (m_{\mathrm{gm}} = 1, 2, ..., n_{\mathrm{gm}}) \tag{5.23}$$

This identification is based on the biomechanical assumption that the walking types for both legs match because legs move in a coordinated manner (interlimb coordination) during one walking cycle [108]. Note that the numbers of time steps differ between legs ($N_{\mathrm{L}} \neq N_{\mathrm{R}}$). When the opposite leg is performing the first four steps of the swing phase, an ML GMM that maximizes the probability of the target leg is used instead.

(2) Prediction Using ML GMM

Using the ML GMM, the expected value and standard deviation of the hidden leg's traveling direction at $k-1$ are calculated from its position, using Gaussian mixture regression:

$$\hat{\theta}'_v = \sum_{l=n_{\mathrm{gm}}(m_{\mathrm{gm}}-1)+1}^{n_{\mathrm{gm}} m_{\mathrm{gm}}} \beta_l \left\{ \mu_{\boldsymbol{p}',l} + \boldsymbol{\Sigma}_{\theta' \boldsymbol{p}',l} \boldsymbol{\Sigma}^{-1}_{\boldsymbol{p}'\boldsymbol{p}',l} \left(\boldsymbol{p}'_{k-1} - \boldsymbol{\mu}_{\boldsymbol{p}',l} \right) \right\} \tag{5.24}$$

$$\hat{\Sigma}_{\theta'_v \theta'_v} = \sum_{l=n_{\mathrm{gm}}(m_{\mathrm{gm}}-1)+1}^{n_{\mathrm{gm}} m_{\mathrm{gm}}} \beta_l^2 \left(\Sigma_{\theta'_v \theta'_v,l} - \boldsymbol{\Sigma}_{\theta'_v \boldsymbol{p}',l} \boldsymbol{\Sigma}^{-1}_{\boldsymbol{p}'\boldsymbol{p}',l} \boldsymbol{\Sigma}_{\boldsymbol{p}' \theta'_v,l} \right) \tag{5.25}$$

$$\beta_l = \frac{p(l)\, p(\boldsymbol{p}' \,|l)}{\sum_{i=n_{\mathrm{gm}}(m_{\mathrm{gm}}-1)+1}^{n_{\mathrm{gm}} m_{\mathrm{gm}}} p(i)\, p(\boldsymbol{p}' \,|i)} = \frac{\pi_l p\left(\boldsymbol{p}' \,|\mu_{\boldsymbol{p}',l}, \Sigma_{\boldsymbol{p}'\boldsymbol{p}',l} \right)}{\sum_{i=n_{\mathrm{gm}}(m_{\mathrm{gm}}-1)+1}^{n_{\mathrm{gm}} m_{\mathrm{gm}}} \pi_i p\left(\boldsymbol{p}' \,|\mu_{\boldsymbol{p}',i}, \Sigma_{\boldsymbol{p}'\boldsymbol{p}',i} \right)} \tag{5.26}$$

The direction of the leg's velocity vector at $k-1$ is then changed to the expected value, as follows:

$$\begin{bmatrix} \hat{x}^f_{k-1} \\ \hat{y}^f_{k-1} \end{bmatrix} = \begin{bmatrix} \cos\hat{\theta}_v \\ \sin\hat{\theta}_v \end{bmatrix} \|\boldsymbol{v}^f_{k-1}\| = \begin{bmatrix} \cos\hat{\theta}_v \\ \sin\hat{\theta}_v \end{bmatrix} \sqrt{\left(\dot{x}^f_{k-1}\right)^2 + \left(\dot{y}^f_{k-1}\right)^2} \tag{5.27}$$

$$\hat{\theta}_v = \hat{\theta}'_v + \frac{\pi}{2} - \theta_r \tag{5.28}$$

Next, the leg position at k is predicted from the acceleration in the expected direction, according to Section 5.2.2(1)–(2).

(3) Gating Using ML GMM

When the occlusion continues for several time steps, the validation region defined by the *a posteriori* covariance matrix expands, owing to the lack of filtering process. This induces an undesired

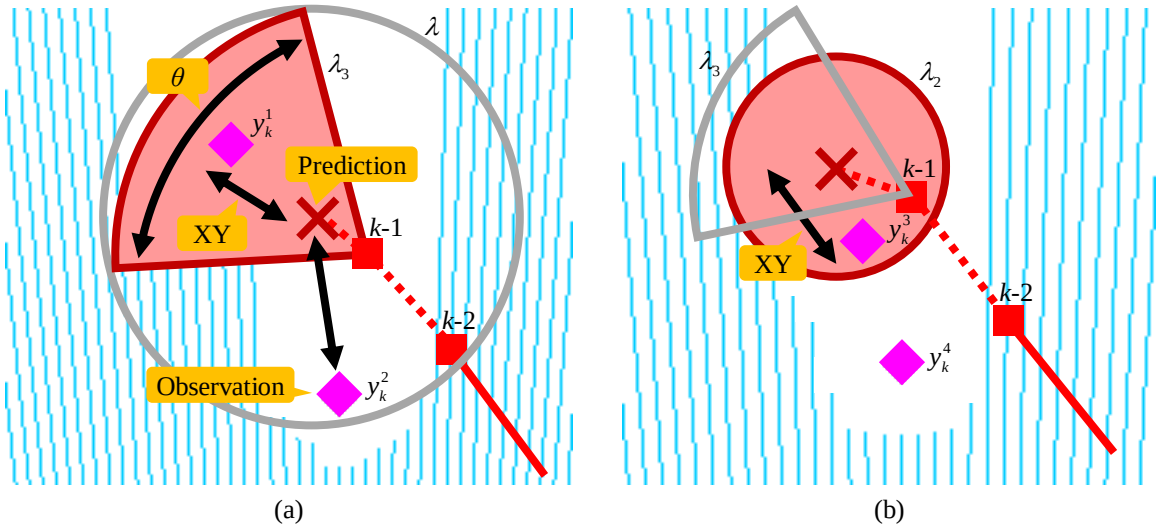

Figure 5.9. (a) The system excludes the undesired observation y_k^2 using the Mahalanobis distance λ_3, by evaluating the relations of the position and the traveling direction. (b) The observation y_k^3 (exhibiting a small distance on the XY-axis and a large direction error) is not excluded by the Mahalanobis distance λ_2, to account for the measurement noise of the LRS.

association with observations away from the traveling direction. To address this problem, the system excludes these undesired observations using the estimated traveling direction, as shown in Figure 5.9(a).

In the gating approach, the three-variable Mahalanobis distance—which evaluates the relations between the predicted position and XY-axis observation and between the ML GMM estimates and the direction from the leg position at $k-1$ to the observation—is calculated as follows:

$$d_{3,j}^f = \sqrt{\begin{bmatrix} x_k^j - \hat{x}_{k/k-1}^f \\ y_k^j - \hat{y}_{k/k-1}^f \\ \tan^{-1}\frac{y_k^j - y_{k-1}^f}{x_k^j - x_{k-1}^f} \end{bmatrix}^\top \begin{bmatrix} \boldsymbol{S}_k^f & \begin{matrix} 0 \\ 0 \end{matrix} \\ \begin{matrix} 0 & 0 \end{matrix} & \hat{\Sigma}_{\theta_v'\theta_v'} \end{bmatrix}^{-1} \begin{bmatrix} x_k^j - \hat{x}_{k/k-1}^f \\ y_k^j - \hat{y}_{k/k-1}^f \\ \tan^{-1}\frac{y_k^j - y_{k-1}^f}{x_k^j - x_{k-1}^f} \end{bmatrix}} \tag{5.29}$$

The threshold to $d_{3,j}^f$ is set to $\lambda_3 = 16.27$ according to the probability $P_G = 0.999$ extracted from the χ^2 distribution with three degrees of freedom. Meanwhile, observations exhibiting a small XY-axis distance and large direction error [as shown in Figure 5.9(b)] should not be excluded. Thus, the Mahalanobis distance on the XY-axis distance is also used to account for the measurement noise of the LRS (defined by covariance matrix $\boldsymbol{R}$):

$$d_{2,j}^f = \sqrt{\begin{bmatrix} x_k^j - \hat{x}_{k/k-1}^f \\ y_k^j - \hat{y}_{k/k-1}^f \end{bmatrix}^\top (\boldsymbol{R})^{-1} \begin{bmatrix} x_k^j - \hat{x}_{k/k-1}^f \\ y_k^j - \hat{y}_{k/k-1}^f \end{bmatrix}} \tag{5.30}$$

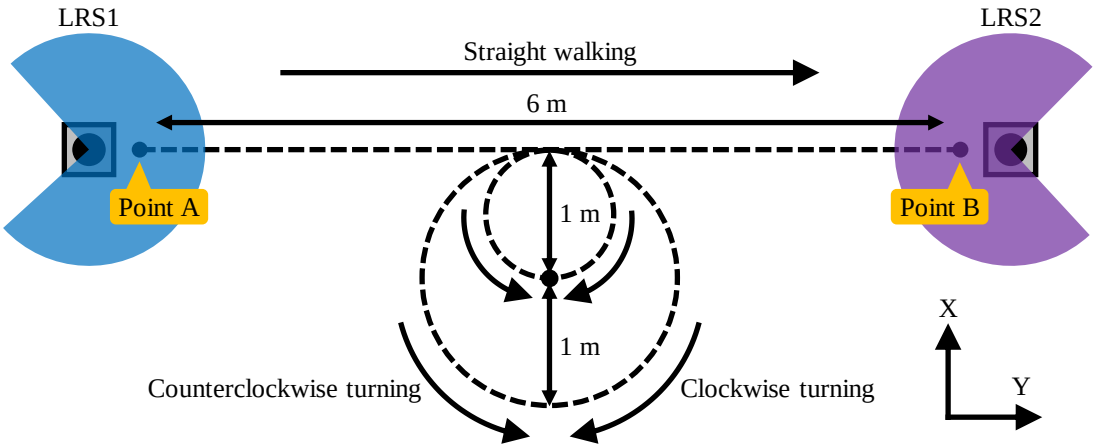

Figure 5.10. A schematic walkway including a straight path of 6 m and circular paths with 0.5 and 1 m radii, as well as walking directions.

The threshold to $d^f_{2,j}$ is set as $\lambda_2 = 13.82$, similar as described in Section 5.2.2(3).

After gating, the system performs data association by minimizing the sum of Mahalanobis distances on the XY-axis [as seen in Section 5.2.2(3)], and filtering is executed when an observation is assigned.

5.3 Evaluation of Learning-based Occlusion Compensation

5.3.1 Study Procedure

Six healthy adults (five males, age: 24.0 ± 3.6 years, height: 1.70 ± 0.07 m, body mass: 65.6 ± 7.2 kg) participated in this study. Ethical approval was obtained from Keio University Research Ethics Committee (reference number 31–80), and informed consent was obtained from participants prior to the experiment. The participants wore shoes containing the instrumented insoles. Their task executions were measured and recorded by the LRS–insole system, using custom software (C++) and a motion capture system comprising eight cameras and a Plug-in Gait lower-body marker set (Nexus, Vicon, Oxford, UK). The data were collected at 40 Hz from the LRS and at 100 Hz from the insoles and the motion capture cameras. All devices were synchronized via voltage inputs and radio communications. Insole measurements were recorded onto microSD cards located on electrical circuit boards fixed to the back of the user's lower leg, and tracking was executed offline using MATLAB. Participants were asked to perform the following tasks on the walkway (highlighted using tape), which included a straight line of 6 m and circular paths with 0.5 and 1 m radii, as illustrated in Figure 5.10.

A. ST: The participants walked in a straight line from points A to B. This task was repeated

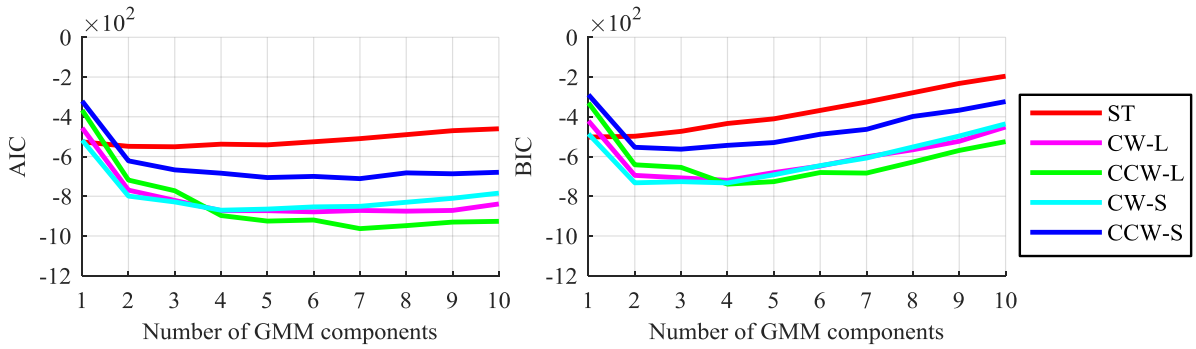

Figure 5.11. AIC and BIC for each number of GMM components.

eight times.

B. The participants walked directly from point A/B, turned clockwise/counterclockwise on the circular path with a radius of 0.5/1 m five times, walked in a straight line again, and stopped at point B/A. These tasks were repeated four times.

(I) CW-L: The participants started from point A and turned clockwise on the circular path of radius 1 m.

(II) CCW-L: The participants started from point B and turned counterclockwise on the circular path of radius 1 m.

(III) CW-S: The participants started from point A and turned clockwise on the circular path of radius 0.5 m.

(IV) CCW-S: The participants started from point B and turned counterclockwise on the circular path of radius 0.5 m.

5.3.2 Data Analysis

First, the proposed system tracked both legs using the merged observations from the two LRSs in tasks A and B. The time-series data were then divided into the walking cycle using the foot grounding times, which were detected by the insoles, and transformed into a unified coordinate system. The traveling direction was calculated from the transformed velocity vector. Next, all datasets (except those for two of the eight trials for task A and one of the four trials for task B) were integrated, and a GMM was fitted to each. The number of GMM components was set to four to ensure that the AIC and BIC values were sufficiently small for datasets describing all walking types, as shown in Figure 5.11. Finally, the system tracked the subject's legs using the observations from one LRS (installed at the start point side in each task) and executed learning-based compensation when occlusion occurred. The ground truth of the leg position in each task was calculated as an internally divided point at 270 mm above the floor between the

knee/ankle joints of the Plug-in Gait model obtained from the motion capture system. The time-series of the ground truth was resampled at 40 Hz according to the LRS.

To evaluate the tracking performance, the number of time steps until tracking failure was calculated. False tracking was identified when one of the following scenarios occurred over four consecutive steps (0.1 s):

- When data association was performed for both legs and the distance from the ground truth of the target leg position to its estimate exceeded the estimate for the opposite leg.
- When data association was not performed for one leg and its estimate was more than 1 m distant from the ground truth.

To assess the advantages of the proposed method [that is the fusion with the instrumented insoles and occlusion compensation (I+C)], two comparative methods were evaluated using the same observations, as follows:

- L-C: The method tracks legs using only a single LRS without fusion with insole data. The grounding of each foot was identified from threshold values of the estimated leg velocity. These was set to $v_{\mathrm{thr}}^{\mathrm{sw}} = 0.93$ (m/s) for the swing phase and $v_{\mathrm{thr}}^{\mathrm{st}} = 0.47$ (m/s) for the stance phase according to [66].
- I-C: The method tracks legs using the fusion with insole data but without occlusion compensation.

5.3.3 Results

The total number of tracking time steps (N_{ALL}), the success rate of tracking steps for L-C, I-C, and I+C ($r_{\mathrm{ST/ALL}}$), the number of trials successfully completed (NS), and the ratio between the number of steps requiring occlusion compensation and the successfully tracked steps for I+C ($r_{\mathrm{C/ST}}$) are listed in Tables 5.1 and 5.2. The results are summarized for each participant and overall. The tracking methods with the highest success rate are highlighted in bold. Examples of leg trajectories tracked by the comparative and proposed methods (I-C and I+C) for turning under different curvatures and directions in subjects B–E are shown in Figure 5.12. The trajectories of the left/right legs are plotted in blue/red, respectively. The accuracies of both leg positions as tracked by I+C in time steps that use data association are listed in Table 5.3. The accuracies were evaluated by one-sample t-test. The null hypothesis was that the accuracy of the method came from a population with a mean value of 100 mm. The alternative hypothesis was that the mean was under 100 mm. A cutoff of 100 mm was chosen because it has been reported as valid for capturing pathological gaits. This includes mild to moderate knee OA, which decreases walking step lengths by 200 mm [3].

Table 5.1. The total time steps, tracking success rate, and rate of occlusion compensation during successful tracking of I+C for gentle turning.

		CW-L						CCW-L					
			$r_{ST/ALL}(\%)$			$r_{C/ST}(\%)$			$r_{ST/ALL}(\%)$			$r_{C/ST}(\%)$	
ID	Trial	N_{ALL}	L-C	I-C	I+C	L	R	N_{ALL}	L-C	I-C	I+C	L	R
A	1	1438	100	37.1	37.1	4.7	4.5	1420	42.8	6.8	100	0.7	11.6
	2	1425	100	100	100	5.5	5.3	1441	6.9	42.7	100	0.8	11.1
	3	1420	100	100	100	5.8	5.1	1397	25.8	25.8	100	0.6	10.2
	4	1394	12.3	100	100	7.1	5.4	1415	61.2	6.8	100	0.8	9.7
	Mean	1419.3	78.1	**84.3**	**84.3**	6.0	5.2	1418.3	34.2	20.5	**100**	0.8	10.6
	NS		**3**	**3**	**3**				0	0	**4**		
B	1	1505	9.5	45.2	100	5.8	3.1	1413	10.4	7.0	100	1.4	9.6
	2	1427	9.7	27.8	100	6.2	3.0	1410	10.1	42.6	100	2.4	11.4
	3	1454	28.1	28.3	100	8.8	1.9	1420	6.8	24.5	100	2.5	9.4
	4	1470	9.7	9.7	100	8.8	2.7	1432	6.6	24.0	100	3.6	11.3
	Mean	1464.0	14.3	27.7	**100**	7.4	2.7	1418.8	8.5	24.5	**100**	2.5	10.4
	NS		0	0	**4**				0	0	**4**		
C	1	1394	40.3	40.3	100	8.8	4.0	1408	27.0	9.4	100	1.3	9.0
	2	1549	63.7	26.3	26.3	8.3	0.0	1527	17.3	17.3	100	1.2	8.1
	3	1421	64.3	100	100	9.5	3.2	1386	25.8	7.6	100	1.7	8.2
	4	1429	47.0	11.3	100	10.1	4.0	1387	11.5	8.1	100	1.4	8.3
	Mean	1448.3	53.8	44.5	**81.6**	9.4	3.4	1427.0	20.4	10.6	**100**	1.4	8.4
	NS		0	1	**3**				0	0	**4**		
D	1	1504	52.7	23.0	100	4.8	6.9	1553	7.0	7.0	100	4.6	9.9
	2	1503	27.4	81.4	100	5.4	5.3	1593	7.6	7.6	100	4.2	10.3
	3	1487	22.9	22.9	100	6.8	5.8	1569	24.3	7.1	100	4.8	8.5
	4	1496	17.9	100	100	5.8	4.8	1552	7.7	7.7	100	4.4	8.0
	Mean	1497.5	30.2	56.8	**100**	5.7	5.7	1566.8	11.7	7.4	**100**	4.5	9.2
	NS		0	1	**4**				0	0	**4**		
E	1	1526	8.7	8.7	100	7.1	4.9	1432	6.7	24.6	100	2.5	11.7
	2	1444	10.0	23.1	100	6.9	6.3	1426	6.9	7.2	100	2.3	9.5
	3	1412	10.3	23.7	88.6	8.2	6.4	1418	2.0	7.1	100	2.6	11.7
	4	1415	40.9	23.6	100	7.1	6.0	1424	44.0	25.2	100	2.1	10.7
	Mean	1449.3	17.5	19.8	**97.1**	7.3	5.9	1425.0	14.9	16.0	**100**	2.4	10.9
	NS		0	0	**3**				0	0	**4**		
F	1	1204	38.5	79.7	100	5.9	5.6	1462	70.3	68.3	100	1.4	12.2
	2	1275	90.7	100	100	7.9	4.5	1284	7.8	7.8	100	1.8	12.5
	3	1378	10.7	100	100	5.6	4.7	1277	83.4	100	100	1.1	11.9
	4	1417	100	35.0	100	7.8	2.6	1182	32.7	100	100	1.1	11.8
	Mean	1318.5	60.0	78.7	**100**	6.8	4.3	1301.3	48.6	69.0	**100**	1.4	12.1
	NS		1	2	**4**				0	2	**4**		

Table 5.2. The total time steps, tracking success rate, and rate of occlusion compensation during successful tracking of I+C for sharp turning.

		CW-S						CCW-S					
			$r_{ST/ALL}(\%)$			$r_{C/ST}(\%)$			$r_{ST/ALL}(\%)$			$r_{C/ST}(\%)$	
ID	Trial	N_{ALL}	L-C	I-C	I+C	L	R	N_{ALL}	L-C	I-C	I+C	L	R
A	1	1000	100	100	100	4.5	2.5	1048	100	100	100	1.3	13.1
	2	1002	100	100	100	6.0	2.8	1022	100	100	100	0.8	12.5
	3	1004	8.5	100	100	5.4	2.6	1045	100	100	100	1.1	12.8
	4	991	100	100	100	3.7	3.0	1064	61.6	26.5	100	1.7	14.2
	Mean	999.3	77.1	**100**	**100**	4.9	2.7	1044.8	90.4	81.6	**100**	1.2	13.2
	NS		3	**4**	**4**				3	3	**4**		
B	1	989	100	100	100	7.9	2.7	972	41.7	41.7	100	3.4	12.7
	2	968	14.6	100	100	6.0	2.2	1067	0.9	38.6	100	5.2	9.7
	3	993	100	100	100	4.5	2.1	983	9.7	9.7	100	1.7	7.1
	4	990	100	100	100	4.0	2.4	999	78.7	100	100	3.4	7.9
	Mean	985.0	78.6	**100**	**100**	5.6	2.4	1005.3	32.7	47.5	**100**	3.5	9.3
	NS		3	**4**	**4**				0	1	**4**		
C	1	945	100	100	100	7.8	3.4	991	13.0	13.0	100	0.8	8.1
	2	1157	100	100	100	6.5	2.6	1120	22.8	22.8	22.7	0.0	1.2
	3	1286	86.8	100	100	7.5	2.6	1178	11.4	11.4	100	0.6	7.6
	4	958	100	100	100	4.3	3.2	995	14.3	14.4	100	1.3	6.5
	Mean	1086.5	96.7	**100**	**100**	6.6	2.9	1071.0	15.4	15.4	**80.7**	0.8	7.0
	NS		3	**4**	**4**				0	0	**3**		
D	1	924	100	100	100	7.3	7.1	957	3.4	27.0	100	6.0	5.4
	2	881	1.7	100	100	4.3	4.7	986	13.5	13.5	100	7.3	5.2
	3	926	24.7	100	100	5.5	5.5	1143	39.1	64.1	100	5.5	4.7
	4	900	42.1	100	100	7.0	4.1	988	14.2	27.2	100	5.9	8.2
	Mean	907.8	42.1	**100**	**100**	6.0	5.4	1018.5	17.6	33.0	**100**	6.1	5.8
	NS		1	**4**	**4**				0	0	**4**		
E	1	869	1.7	100	100	5.2	5.3	862	12.3	23.9	77.3	8.4	8.1
	2	842	1.1	10.0	73.4	5.0	5.0	855	12.5	46.8	100	8.0	6.7
	3	868	25.2	100	86.8	7.3	3.1	835	12.5	29.2	100	8.6	8.3
	4	857	10.6	10.6	100	6.2	4.0	830	12.9	100	100	3.9	5.5
	Mean	859.0	9.7	55.1	**90.0**	5.9	4.3	845.5	12.5	50.0	**94.3**	7.2	7.1
	NS		0	**2**	**2**				0	1	**3**		
F	1	922	100	100	100	6.1	2.1	830	12.8	100	100	0.7	10.0
	2	892	100	100	100	4.7	3.0	840	13.6	100	100	0.7	6.5
	3	388	100	100	23.2	0.0	0.0	828	13.4	79.3	100	0.5	12.0
	4	934	100	100	100	3.9	3.4	729	100	100	100	0.5	9.1
	Mean	784.0	**100**	**100**	80.8	4.7	2.7	806.8	34.9	94.8	**100**	0.6	9.4
	NS		**4**	**4**	3				1	3	**4**		

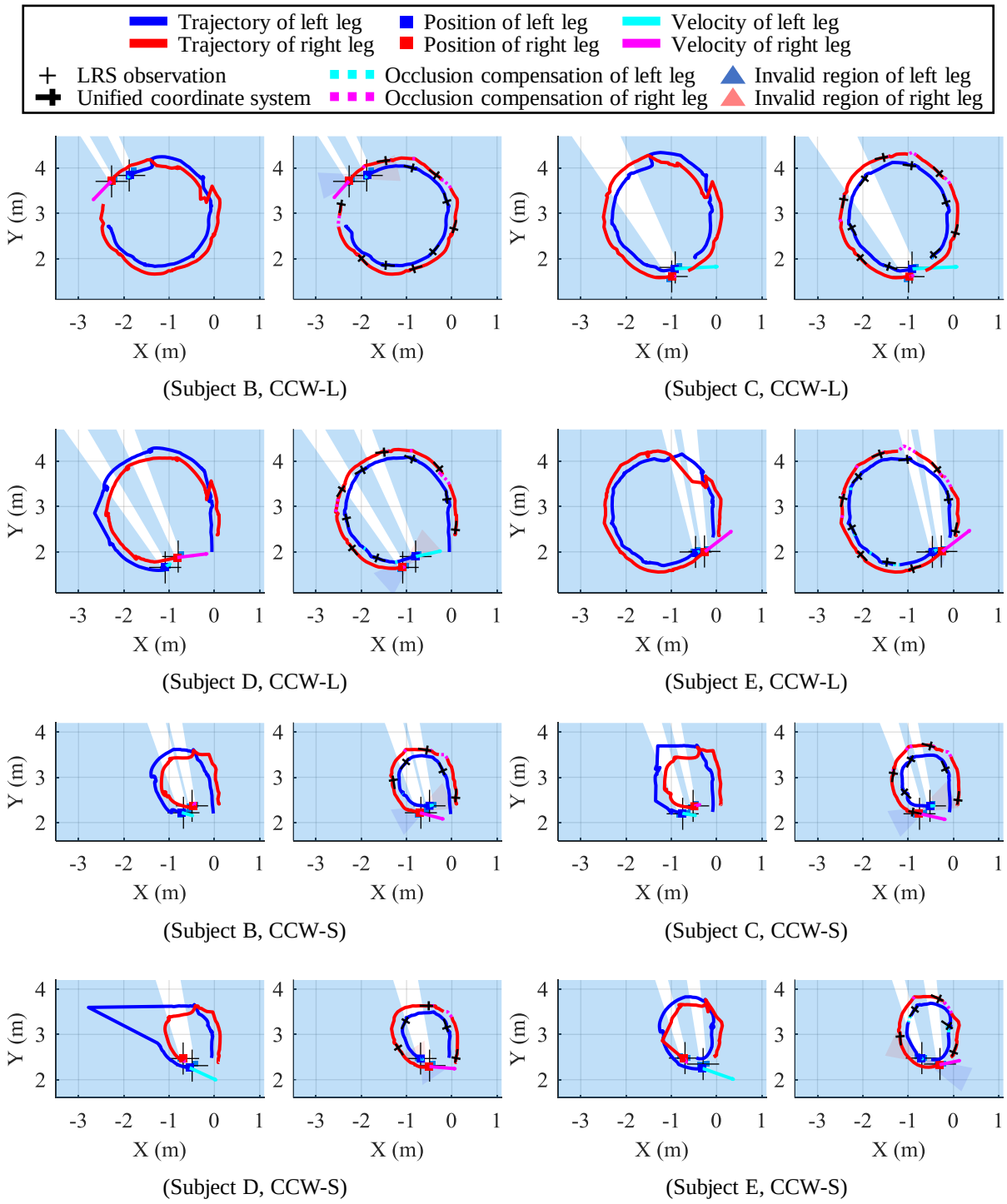

Figure 5.12. Leg trajectories tracked by I-C (left) and I+C (right) for gentle and sharp counterclockwise turning in subjects B–E.

Table 5.3. The mean (± SD) error of leg positions tracked by I+C in time steps with data association.

		CW-L		CCW-L		CW-S		CCW-S	
ID	Trial	L (mm)	R (mm)	L (mm)	R (mm)	L (mm)	R (mm)	L (mm)	R (mm)
A	1	45.4 (25.6)	58.6 (32.7)	51.2 (27.0)	42.7 (28.7)	33.3 (20.9)	49.4 (26.0)	44.1 (23.5)	27.6 (22.2)
	2	41.8 (28.1)	61.7 (32.5)	51.4 (28.3)	42.1 (28.4)	37.4 (21.9)	49.8 (28.2)	43.7 (24.3)	29.2 (22.5)
	3	41.3 (28.1)	62.9 (35.0)	50.6 (28.1)	43.1 (28.3)	33.8 (20.6)	48.5 (26.7)	45.4 (27.0)	28.5 (22.2)
	4	42.2 (28.2)	61.3 (34.2)	51.6 (29.7)	41.6 (27.3)	34.2 (22.0)	49.6 (27.7)	45.7 (27.0)	28.8 (25.2)
	Mean	42.2 (27.9)	61.6 (33.8)	51.2 (28.3)	42.4 (28.2)	34.7 (21.4)	49.3 (27.2)	44.7 (25.5)	28.5 (23.1)
B	1	44.8 (25.3)	57.8 (33.5)	46.5 (23.4)	38.4 (26.1)	35.6 (18.3)	49.4 (25.2)	35.2 (22.9)	35.7 (20.2)
	2	43.2 (22.7)	55.8 (31.9)	48.0 (26.2)	42.0 (28.4)	36.8 (18.8)	49.4 (27.2)	35.7 (21.0)	33.6 (20.0)
	3	47.2 (27.5)	64.9 (37.4)	48.6 (26.3)	40.4 (27.6)	34.6 (19.0)	50.7 (34.0)	37.3 (22.2)	34.6 (19.9)
	4	44.4 (24.6)	56.8 (33.5)	49.9 (25.2)	41.6 (28.4)	37.8 (19.6)	48.9 (24.9)	34.6 (18.2)	32.5 (19.6)
	Mean	44.9 (25.1)	58.8 (34.3)	48.2 (25.3)	40.6 (27.7)	36.2 (19.0)	49.6 (28.1)	35.7 (21.2)	34.0 (20.0)
C	1	53.6 (28.6)	51.7 (32.5)	47.3 (27.5)	42.4 (28.5)	46.7 (20.6)	42.4 (26.3)	34.6 (20.4)	35.2 (20.3)
	2	34.8 (38.1)	36.8 (31.1)	45.4 (26.1)	40.1 (28.1)	43.1 (21.9)	37.5 (25.7)	18.1 (17.5)	13.5 (15.2)
	3	50.8 (28.6)	49.1 (31.3)	47.1 (26.9)	43.1 (31.0)	39.8 (23.8)	36.0 (25.4)	32.8 (20.6)	33.1 (17.6)
	4	51.0 (28.5)	51.7 (32.8)	46.3 (26.4)	42.9 (30.0)	44.9 (19.9)	41.2 (25.5)	33.8 (20.3)	33.4 (19.0)
	Mean	50.3 (29.9)	49.5 (32.4)	46.5 (26.7)	42.1 (29.4)	43.3 (22.0)	38.9 (25.8)	32.5 (20.7)	32.2 (19.5)
D	1	42.2 (26.1)	55.0 (30.6)	50.7 (27.1)	43.5 (26.6)	40.1 (26.2)	57.9 (33.3)	58.0 (27.4)	42.3 (23.4)
	2	41.6 (26.8)	53.2 (30.8)	50.5 (26.5)	42.9 (27.3)	38.5 (25.7)	57.8 (31.9)	61.0 (27.7)	43.4 (24.1)
	3	44.5 (33.1)	56.6 (32.1)	51.0 (27.5)	44.7 (28.0)	40.6 (28.8)	58.8 (33.1)	58.4 (25.8)	44.3 (22.5)
	4	43.5 (27.9)	53.2 (29.1)	50.4 (26.0)	43.7 (28.4)	41.2 (27.1)	55.2 (31.4)	60.5 (30.4)	44.0 (24.5)
	Mean	42.9 (28.6)	54.5 (30.7)	50.6 (26.8)	43.7 (27.6)	40.1 (27.0)	57.5 (32.4)	59.4 (27.8)	43.5 (23.6)
E	1	50.8 (37.4)	52.7 (31.0)	49.7 (26.4)	40.4 (27.5)	52.6 (28.9)	57.9 (32.0)	46.3 (27.3)	59.2 (47.1)
	2	51.2 (39.8)	53.5 (32.1)	49.5 (25.6)	41.2 (28.6)	50.8 (24.2)	59.5 (32.9)	44.8 (27.2)	33.9 (23.2)
	3	53.4 (35.5)	57.2 (33.8)	49.1 (25.6)	40.3 (27.1)	48.8 (23.4)	61.7 (31.9)	45.3 (25.7)	35.5 (24.2)
	4	54.5 (40.2)	56.2 (32.9)	48.8 (25.9)	39.7 (26.4)	48.8 (25.2)	58.9 (30.9)	43.6 (24.7)	35.7 (22.7)
	Mean	52.4 (38.4)	54.8 (32.5)	49.2 (25.9)	40.4 (27.4)	50.2 (25.7)	59.4 (31.9)	44.9 (26.2)	40.0 (31.4)
F	1	41.8 (25.4)	44.2 (25.0)	44.3 (28.0)	46.9 (29.4)	37.6 (20.3)	36.9 (21.2)	47.3 (24.6)	46.9 (29.0)
	2	40.4 (24.0)	42.6 (24.9)	49.5 (31.5)	48.6 (29.4)	37.0 (20.0)	39.2 (21.4)	47.5 (23.2)	45.9 (26.0)
	3	38.9 (23.8)	41.4 (24.5)	49.9 (30.7)	48.5 (29.7)	35.7 (13.5)	36.6 (18.0)	47.4 (24.0)	44.8 (27.3)
	4	39.4 (25.2)	42.3 (22.5)	48.4 (29.6)	48.2 (28.5)	37.0 (19.4)	39.1 (21.3)	48.4 (23.9)	44.0 (22.9)
	Mean	40.1 (24.6)	42.6 (24.2)	47.9 (30.0)	48.0 (29.3)	37.2 (19.7)	38.3 (21.2)	47.7 (23.9)	45.4 (26.5)
All	Mean	45.4 (29.8)	53.7 (32.1)	49.0 (27.2)	42.8 (28.3)	40.0 (23.0)	48.6 (29.1)	44.3 (25.9)	37.3 (24.9)
	p	<0.001	<0.001	<0.001	<0.001	<0.001	<0.001	<0.001	<0.001
	$1-\beta$	0.985	0.915	0.987	0.994	1.000	0.978	0.997	1.000

5.3.4 Discussion

(1) General Discussion

Tables 5.1 and 5.2 show that, in most trials and for all walking types, the proposed method with occlusion compensation (I+C) continued tracking for more time steps than the comparative methods without compensation (L-C, I-C). Similarly, Figure 5.12 demonstrate that the method without compensation (I-C) often failed to continue tracking when occlusion occurs while the method with the compensation (I+C) did continue. This extension of the tracking distance is valuable because the GNN does not guarantee recovery after tracking failure. This advantage can lead to efficient clinical assessments, even when only a few trials can be measured (owing to physical burdens on the patients or limitations of consultation time).

Table 5.3 shows that, when tracked using the proposed method (I+C) in time steps with data association, the mean error of both leg positions was below 60 mm, which is valid for clinical assessment (under 100 mm, $p < 0.001$, $1 - \beta > 0.9$). From the above results, it can be seen that the proposed method—which applies learning-based occlusion compensation—can track the complicated dynamic motions of both legs during walking on circular paths with valid accuracy.

(2) Limitations

This study examined the validity of the proposed method for only a few types of periodic curved walking. However, the tasks included transitions from straight to curved walking trajectories and vice versa, and the proposed method improved the tracking performance for these phases. Therefore, the proposed method can be widely applied to walking tests, including turnings of various curvatures (e.g., the Figure-of-Eight Walk test). Meanwhile, the robustness of the method against specific leg motions (e.g., slow walking with short steps), which may induce extreme long-term occlusion, should be examined in future research.

5.4 Conclusion

This chapter presented the learning-based compensation of the leg position to facilitate LRS-based tracking of both legs during walking on circular paths, using the interlimb coordination during one walking cycle. The method measures straight walking and turning motions under different curvatures/directions in advance, and then learns the relationship between the trajectory and traveling direction for each leg during one cycle of each walking type using GMMs. During tracking, the walking type is identified from the joint probability of both legs' trajectories dur-

ing the walking cycle, according to the interlimb coordination, and the traveling direction and position of the hidden leg during occlusion are estimated by the ML GMM. Experimental results showed that the proposed method prevents undesirable data associations during occlusion and continues to track legs after recovering from occlusion.

Chapter 6

Conclusion

6.1 Summary of Contributions

To estimate and track human motions using wearable/fixed sensors, this dissertation focused on solving two problems that arise when modeling the relationships between the sensor measurements and motion parameters or complicated motion dynamics. The first is that the learning approaches lose estimation accuracy through overfitting when the diversity and size of the dataset are constrained by device resources and the user's limited motor abilities. The second is that a single model cannot adapt to changes in the sensor–motion relationship, owing to sensing conditions and the complicated motions that cannot be represented by a specific model.

To address these issues, data-efficient learning that uses small datasets and limited sensor resources (i.e., without highly accurate devices) is required to obtain motion estimation models. Moreover, the training of multiple models according to the measurement condition and adaptive estimation through selecting the adequate model therefrom are needed to handle changes in sensor–motion relationships and complicated dynamic motions. Therefore, this dissertation presented the biomechanics-driven stochastic learning for human motion sensing systems, which achieved data-efficient learning of motion estimation models using limited datasets and adaptive estimation using multiple models.

6.1.1 Theoretical Contributions

(1) Data-efficient Learning for User-specific Model Acquisition

Chapters 2 and 3 presented the constrained least squares method and data augmentation, which are based on biomechanics, and stochastic learning techniques. These facilitate the data-efficient learning of sophisticated models using a small dataset with constrained diversity while avoiding

overfitting.

More specifically, Chapter 2 presented the force plate-free learning that estimates vGRF during walking using an insole instrumented with a small number of force sensors. This method uses limited data that consists of only the insole measurements and the user's body weight. The system learns a linear regression model between the insole measurements during SLS and body weight by the least squares method, which is based on biomechanics that vGRF during SLS approximately matches the body weight. In the regression, linear constraints with upper/lower bounds based on the biomechanics that magnitudes of peak/trough vGRFs and stance durations during natural walking are linearly related are added to avoid overfitting. In addition, Chapter 3 presented the one-step learning that uses only one walking step to handle the cases in which performing SLS or multiple-step walking is difficult because of the user's decreased motor abilities. The system probabilistically augments the actual insole measurements and vGRF obtained from a low-cost body scale for a single step to a virtual dataset for multiple steps. This augmentation applies the biomechanical assumption that the insole measurements and vGRF obtained from the scale vary between multiple walking steps, owing to the inconsistencies of walking behaviors. In addition, the method learns a Gaussian process regression model, which prevents overfitting on a small dataset.

(2) Multiple Model Learning for Adaptive Estimation

Chapters 4 and 5 presented the learning of multiple GMMs and biomechanics-based identification of the ML model. These facilitate adaptive estimation by handling changes in the relationships between the sensor measurements and the motion parameters or complex motion dynamics, which are difficult to represent with a single model.

More specifically, Chapter 4 presented the shift-adaptive estimation to obtain the joint angle from a knee brace instrumented with two stretch sensors. This method consists of learning multiple models and performing adaptive estimation to changes in the relationship between the sensor strains and the joint angle due to the brace shift. The system alters the relationship between the strains of the two stretch sensors, which are placed above and below the patella hole of the brace, by utilizing biomechanics that the skin strain is high in the patella area and rapidly decreases further away from the joint. Next, the relationship between the two sensor strains and joint angles at varying brace shift positions is leaned via GMMs. In the estimation, an ML GMM is identified from the relationship between the two sensor strains, and the angle is calculated adaptively to the brace shift. In addition, Chapter 5 presented the learning-based occlusion compensation for leg position based upon the interlimb coordination for one walking cycle. This facilitates LRS-based tracking of complicated dynamic motions of both legs during walking on circular paths. The method measures straight walking and turning

under different curvatures/directions in advance, and then learns the relationship between the trajectory and traveling direction of each leg during one walking cycle for each walking type using GMMs. In the tracking, the walking type is identified using the joint probability of both legs' trajectories during the walking cycle under the biomechanical assumption that both legs move in a coordinated manner, and the ML GMM estimates the traveling direction and position of the hidden leg during occlusion.

6.1.2 Practical Contributions

(1) Kinetic Motion Sensing System

Chapter 2 presented force plate-free learning, which uses only the insole measurements during single leg stance and walking, and Chapter 3 proposed one-step learning, which uses the measurement of one walking step using the insole and a low-cost body scale. These learning schemes achieve an accessible and efficient vGRF estimation that does not require highly accurate devices (e.g., force plates) and complicated motions.

(2) Kinematic Motion Sensing System

Chapter 4 described the estimation of knee joint angle adaptive to the brace shift, which consists of a brace instrumented with two stretch sensors, learning of user-specific GMMs from multiple brace shift positions, and ML GMM identification. The system achieves the measurement of joint angle robust to the brace shifts during long-term wearing or donning/doffing.

(3) Spatial Motion Sensing System

Chapter 5 presented the learning-based occlusion compensation for leg position to facilitate the tracking of both legs during walking on circular paths. The system offers enhanced tracking performances for straight and curved walking and achieves efficient evaluation of step length/width using only a few clinical trials.

6.2 Future Work

6.2.1 Validation for Patients with Severe Musculoskeletal Disease

In this dissertation, the models for estimating human motion were learned as user-specific using datasets acquired from the users themselves. Thus, they can adapt to individual differences (e.g., foot size or body shape). Meanwhile, the proposed systems are intended for the assessment of

patients with mild to moderate musculoskeletal diseases, who can perform natural motions such as SLS, straight/curved walking, and knee flexion/extension. Therefore, the validity of each system for patients with severe musculoskeletal disease (who cannot perform such motions) should be investigated in future work.

6.2.2 Robustness for Different Conditions of Fabric and Clothes

Chapters 2 and 3 described that the instrumented insole was firmly fixed to the shoe and covered with a relatively hard insole to ensure sensitivity. However, slippage of the insole sensor and plastic deformation of the covering insole during actual use may affect the relationship between sensor measurements and vGRF. Chapter 4 used the brace capable of stabilizing the patella for the estimation of joint angle with stretch sensors, and the effect of the brace wrinkles was negligible. However, when the system is applied to a typical low-restraint brace with high stretchability, irregular deformations due to wrinkles may affect the strains of the stretch sensors. To manage these changes to the sensor, the systems must learn more diverse models beforehand or recognize the changes autonomously during actual use and perform re-learning to obtain a new model. In addition, Chapter 5 described LRS-based leg tracking, which assumes that the target person wears tight-fitting clothes. Thus, the robustness of leg tracking against fluctuations caused by the looser clothes must be enhanced, by using probabilistic learning approaches to model perturbation of surface shape.

6.2.3 Extension to Three-dimensional Motion Sensing

Although the instrumented insoles (described in Chapters 2 and 3) and the brace (described in Chapter 4) facilitates estimation of one-dimensional/uniaxial motion parameters, the three-dimensional GRFs and triaxial joint angles are essential for calculating joint torques that represent a more detailed motor function. In addition, although a two-dimensional LRS was used in Chapter 5, depth cameras (e.g., Microsoft's Kinect) have recently attracted attention in three-dimensional motion analysis. However, when estimating and tracking three-dimensional motion, the relationship between sensor measurements and motion parameters become further complicated. Therefore, large-scale models with multiple inputs and outputs (and considering the correlations between each of them) should be examined. In addition, changes to the sensor structure, as well as the addition of further sensors (e.g., IMUs) to obtain different motion parameters, could enhance the estimation.

Bibliography

[1] Anatole Vilhelm Wiik, Adeel Aqil, Mads Brevadt, Gareth Jones, and Justin Cobb. Abnormal ground reaction forces lead to a general decline in gait speed in knee osteoarthritis patients. *World Journal of Orthopedics*, 8(4):322–328, 2017.

[2] Xiaolong Zeng, Limin Ma, Zefeng Lin, Wenhan Huang, Zhiqiang Huang, Yu Zhang, and Chuanbin Mao. Relationship between kellgren-lawrence score and 3d kinematic gait analysis of patients with medial knee osteoarthritis using a new gait system. *Scientific Reports*, 7:8, 2017.

[3] Janie L. Astephen, Kevin J. Deluzio, Graham E. Caldwell, and Michael J. Dunbar. Biomechanical changes at the hip, knee, and ankle joints during gait are associated with knee osteoarthritis severity. *Journal of Orthopaedic Research*, 26(3):332–341, 2008.

[4] Eileen Chih-Ying Yang and Ming-Hsu Mao. 3d analysis system for estimating intersegmental forces and moments exerted on human lower limbs during walking motion. *Measurement*, 73:171–179, 2015.

[5] Yuzhu Guo, Fabio Storm, Yifan Zhao, Stephen A. Billings, Aleksandar Pavic, Claudia Mazza, and Ling-Zhong Guo. A new proxy measurement algorithm with application to the estimation of vertical ground reaction forces using wearable sensors. *Sensors*, 17(10), 2017.

[6] Erfan Shahabpoor and Aleksandar Pavic. Estimation of vertical walking ground reaction force in real-life environments using single imu sensor. *Journal of Biomechanics*, 79:181–190, 2018.

[7] Erfan Shahabpoor, Aleksandar Pavic, James M. W. Brownjohn, Stephen A. Billings, Ling-Zhong Guo, and Mateusz Bocian. Real-life measurement of tri-axial walking ground reaction forces using optimal network of wearable inertial measurement units. *IEEE Transactions on Neural Systems and Rehabilitation Engineering*, 26(6):1243–1253, 2018.

[8] Kieron Jie-Han Ngoh, Darwin Gouwanda, Alpha A. Gopalai, and Yu Zheng Chong. Estimation of vertical ground reaction force during running using neural network model and uniaxial accelerometer. *Journal of Biomechanics*, 76:269–273, 2018.

[9] Christian Liedtke, Steven A. W. Fokkenrood, Jasper T. Menger, Herman van der Kooij, and Peter H. Veltink. Evaluation of instrumented shoes for ambulatory assessment of ground reaction forces. *Gait & Posture*, 26(1):39–47, 2007.

[10] Tao Liu, Yoshio Inoue, and Kyoko Shibata. A wearable ground reaction force sensor system and its application to the measurement of extrinsic gait variability. *Sensors*, 10(11):10240–10255, 2010.

[11] H. L. P. Hurkmans, J. B. J. Bussmann, R. W. Selles, H. L. D. Horemans, Eric Benda, H. J. Stam, and J. A. N. Verhaar. Validity of the pedar mobile system for vertical force measurement during a seven-hour period. *Journal of Biomechanics*, 39(1):110–118, 2006.

[12] Carina Price, Daniel Parker, and Christopher Nester. Validity and repeatability of three in-shoe pressure measurement systems. *Gait & Posture*, 46:69–74, 2016.

[13] A. Forner Cordero, H. J. F. M. Koopman, and F. C. T. Van Der Helm. Use of pressure insoles to calculate the complete ground reaction forces. *Journal of Biomechanics*, 37(9):1427–1432, 2004.

[14] A. Forner-Cordero, H. J. F. M. Koopman, and F. C. T. Van der Helm. Inverse dynamics calculations during gait with restricted ground reaction force information from pressure insoles. *Gait & Posture*, 23(2):189–199, 2006.

[15] Yihwan Jung, Moonki Jung, Kunwoo Lee, and Seungbum Koo. Ground reaction force estimation using an insole-type pressure mat and joint kinematics during walking. *Journal of Biomechanics*, 47(11):2693–2699, 2014.

[16] Yihwan Jung, Moonki Jung, Jiseon Ryu, Sukhoon Yoon, Sang-Kyoon Park, and Seungbum Koo. Dynamically adjustable foot-ground contact model to estimate ground reaction force during walking and running. *Gait & Posture*, 45:62–68, 2016.

[17] Stacy J. Morris Bamberg, Ari Y. Benbasat, Donna Moxley Scarborough, David E. Krebs, and Joseph A. Paradiso. Gait analysis using a shoe-integrated wireless sensor system. *IEEE Transactions on Information Technology in Biomedicine*, 12(4):413–423, 2008.

[18] Edward S. Sazonov, George Fulk, James Hill, Yves Schutz, and Raymond Browning. Monitoring of posture allocations and activities by a shoe-based wearable sensor. *IEEE Transactions on Biomedical Engineering*, 58(4):983–990, 2011.

[19] Christian B. Redd and Stacy J. Morris Bamberg. A wireless sensory feedback device for real-time gait feedback and training. *IEEE/ASME Transactions on Mechatronics*, 17(3):425–433, 2012.

[20] Philip S. Dyer and Stacy J. Morris Bamberg. Instrumented insole vs. force plate: A comparison of center of plantar pressure. In *2011 Annual International Conference of the IEEE Engineering in Medicine and Biology Society*, pages 6805–6809, 2011.

[21] Adam M. Howell, Toshiki Kobayashi, Teri Rosenbaum Chou, Wayne Daly, Michael Orendurff, and Stacy J. Morris Bamberg. A laboratory insole for analysis of sensor placement to determine ground reaction force and ankle moment in patients with stroke. In *2012 Annual International Conference of the IEEE Engineering in Medicine and Biology Society*, pages 6394–6397, 2012.

[22] Daniel Tik-Pui Fong, Yue-Yan Chan, Youlian Hong, Patrick Shu-Hang Yung, Kwai-Yau Fung, and Kai-Ming Chan. Estimating the complete ground reaction forces with pressure insoles in walking. *Journal of Biomechanics*, 41(11):2597–2601, 2008.

[23] Adam M. Howell, Toshiki Kobayashi, Heather A. Hayes, K. Bo Foreman, and Stacy J. Morris Bamberg. Kinetic gait analysis using a low-cost insole. *IEEE Transactions on Biomedical Engineering*, 60(12):3284–3290, 2013.

[24] Fang Pu, Yang Yang, Xiaoya Fan, Shuyu Li, Yan Li, Deyu Li, and Yubo Fan. Optimal estimation of total plantar force for monitoring gait in daily life activities with low-price insole system. *Journal of Mechanics in Medicine and Biology*, 14(3), 2014.

[25] Ryo Eguchi and Masaki Takahashi. Accessible calibration of insole force sensors using the wii balance board for kinetic gait analysis. In *2018 IEEE SENSORS*, pages 1–4. IEEE, 2018.

[26] Hossein Rouhani, Julien Favre, Xavier Crevoisier, and Kamiar Aminian. Ambulatory assessment of 3d ground reaction force using plantar pressure distribution. *Gait & posture*, 32(3):311–316, 2010.

[27] Daniel A. Jacobs and Daniel P. Ferris. Estimation of ground reaction forces and ankle moment with multiple, low-cost sensors. *Journal of NeuroEngineering and Rehabilitation*, 12, 2015.

[28] Taeyong Sim, Hyunbin Kwon, Seung Eel Oh, Su-Bin Joo, Ahnryul Choi, Hyun Mu Heo, Kisun Kim, and Joung Hwan Mun. Predicting complete ground reaction forces and moments during gait with insole plantar pressure information using a wavelet neural network. *Journal of Biomechanical Engineering*, 137(9), 2015.

[29] Parker G. Rosquist, Gavin Collins, A. Jake Merrell, Noelle J. Tuttle, James B. Tracy, Evan T. Bird, Matthew K. Seeley, David T. Fullwood, William F. Christensen, and Anton E. Bowden. Estimation of 3d ground reaction force using nanocomposite piezo-responsive foam sensors during walking. *Annals of Biomedical Engineering*, 45(9):2122–2134, 2017.

[30] Charence Wong, Zhi-Qiang Zhang, Benny Lo, and Guang-Zhong Yang. Wearable sensing for solid biomechanics: A review. *IEEE Sensors Journal*, 15(5):2747–2760, 2015.

[31] Pietro Picerno. 25 years of lower limb joint kinematics by using inertial and magnetic sensors: A review of methodological approaches. *Gait & Posture*, 51:239–246, 2017.

[32] Jody L. Riskowski. Gait and neuromuscular adaptations after using a feedback-based gait monitoring knee brace. *Gait & Posture*, 32(2):242–247, 2010.

[33] Shweta Pant, Sharath Umesh, and Sundarrajan Asokan. Knee angle measurement device using fiber bragg grating sensor. *IEEE Sensors Journal*, 18(24):10034–10040, 2018.

[34] Peter T. Gibbs and H. Harry Asada. Wearable conductive fiber sensors for multi-axis human joint angle measurements. *Journal of NeuroEngineering and Rehabilitation*, 2(1):7, 2005.

[35] Dragan Z. Stupar, Jovan S. Bajic, Lazo M. Manojlovic, Milos P. Slankamenac, Ana V. Joza, and Milos B. Zivanov. Wearable low-cost system for human joint movements monitoring based on fiber-optic curvature sensor. *IEEE Sensors Journal*, 12(12):3424–3431, 2012.

[36] Abeer A. Mohamed, Jennifer Baba, James Beyea, John Landry, Andrew Sexton, and Chris A. McGibbon. Comparison of strain-gage and fiber-optic goniometry for measuring knee kinematics during activities of daily living and exercise. *Journal of Biomechanical Engineering*, 134(8), 2012.

[37] Andressa Rezende, Camille Alves, Isabela Marques, Marco Aurélio Silva, and Eduardo Naves. Polymer optical fiber goniometer: A new portable, low cost and reliable sensor for joint analysis. *Sensors*, 18(12), 2018.

[38] Po T. Wang, Christine E. King, An H. Do, and Zoran Nenadic. A durable, low-cost electrogoniometer for dynamic measurement of joint trajectories. *Medical Engineering & Physics*, 33(5):546–552, 2011.

[39] Alessandro Tognetti, Federico Lorussi, Nicola Carbonaro, and Danilo de Rossi. Wearable goniometer and accelerometer sensory fusion for knee joint angle measurement in daily life. *Sensors*, 15(11):28435–28455, 2015.

[40] Zamir Ahmed Abro, Yi-Fan Zhang, Nan-Liang Chen, Cheng-Yu Hong, Rafique Ahmed Lakho, and Habiba Halepoto. A novel flex sensor-based flexible smart garment for monitoring body postures. *Journal of Industrial Textiles*, 49(2):262–274, 2019.

[41] Yiğit Mengüç, Yong-Lae Park, Hao Pei, Daniel Vogt, Patrick M. Aubin, Ethan Winchell, Lowell Fluke, Leia Stirling, Robert J. Wood, and Conor J. Walsh. Wearable soft sensing suit for human gait measurement. *The International Journal of Robotics Research*, 33(14):1748–1764, 2014.

[42] Hyosang Lee, Jiseung Cho, and Jung Kim. Printable skin adhesive stretch sensor for measuring multi-axis human joint angles. In *2016 IEEE International Conference on Robotics and Automation (ICRA)*, pages 4975–4980, 2016.

[43] Hiroyuki Nakamoto, Hideo Ootaka, Mitsunori Tada, Ichiro Hirata, Futoshi Kobayashi, and Fumio Kojima. Stretchable strain sensor with anisotropy and application for joint angle measurement. *IEEE Sensors Journal*, 16(10):3572–3579, 2016.

[44] Massimo Totaro, Tommaso Poliero, Alessio Mondini, Chiara Lucarotti, Giovanni Cairoli, Jesus Ortiz, and Lucia Beccai. Soft smart garments for lower limb joint position analysis. *Sensors*, 17(10), 2017.

[45] Bo Huang, Mingyu Li, Tao Mei, David McCoul, Shihao Qin, Zhanfeng Zhao, and Jianwen Zhao. Wearable stretch sensors for motion measurement of the wrist joint based on dielectric elastomers. *Sensors*, 17(12), 2017.

[46] Dooyoung Kim, Junghan Kwon, Seunghyun Han, Yong-Lae Park, and Sungho Jo. Deep full-body motion network for a soft wearable motion sensing suit. *IEEE/ASME Transactions on Mechatronics*, 24(1):56–66, 2019.

[47] Dooyoung Kim, Min Kim, Junghan Kwon, Yong-Lae Park, and Sungho Jo. Semi-supervised gait generation with two microfluidic soft sensors. *IEEE Robotics and Automation Letters*, 4(3):2501–2507, 2019.

[48] Angelo M. Sabatini and Valentina Colla. A method for sonar based recognition of walking people. *Robotics and Autonomous Systems*, 25(1-2):117–126, 1998.

[49] Asif Mehmood, James M. Sabatier, Marshall Bradley, and Alexander Ekimov. Extraction of the velocity of walking human's body segments using ultrasonic doppler. *Journal of the Acoustical Society of America*, 128(5):EL316–EL322, 2010.

[50] Marshall Bradley and James M. Sabatier. Applications of fresnel-kirchhoff diffraction theory in the analysis of human-motion doppler sonar grams. *The Journal of the Acoustical Society of America*, 128(5):EL248–EL253, 2010.

[51] Gaddi Blumrosen, Ben Fishman, and Yossi Yovel. Noncontact wideband sonar for human activity detection and classification. *IEEE Sensors Journal*, 14(11):4043–4054, 2014.

[52] Ondřej Ťupa, Aleš Procházka, Oldřich Vyšata, Martin Schätz, Jan Mareš, Martin Vališ, and Vladimír Mařík. Motion tracking and gait feature estimation for recognising parkinson's disease using ms kinect. *Biomedical Engineering Online*, 14:20, 2015.

[53] B. Fosty, G. Ben-Sadoun, G. Sacco, A. König, V. Manera, P. Foulon, J. Brisswalter, P. H. Robert, and F. Bremond. Accuracy and reliability of the rgb-d camera for measuring walking speed on a treadmill. *Gait & Posture*, 48:113–119, 2016.

[54] Xi Cai, Guang Han, Xin Song, and Jinkuan Wang. Single-camera-based method for step length symmetry measurement in unconstrained elderly home monitoring. *IEEE Transactions on Biomedical Engineering*, 64(11):2618–2627, 2017.

[55] Maria do Carmo Vilas-Boas, Hugo Miguel Pereira Choupina, Ana Patrícia Rocha, José Maria Fernandes, and João Paulo Silva Cunha. Full-body motion assessment: Concurrent validation of two body tracking depth sensors versus a gold standard system during gait. *Journal of Biomechanics*, 87:189–196, 2019.

[56] Kentaro Yagi, Yuta Sugiura, Kunihiro Hasegawa, and Hideo Saito. Gait measurement at home using a single rgb camera. *Gait & Posture*, 76:136–140, 2020.

[57] Tomàs Pallejà, Mercè Teixidó, Marcel Tresanchez, and Jordi Palacín. Measuring gait using a ground laser range sensor. *Sensors*, 9(11):9133–9146, 2009.

[58] Nicola Bellotto and Huosheng Hu. Multisensor-based human detection and tracking for mobile service robots. *IEEE Transactions on Systems, Man, and Cybernetics, Part B (Cybernetics)*, 39(1):167–181, 2008.

[59] Oscar Martinez Mozos, Ryo Kurazume, and Tsutomu Hasegawa. Multi-part people detection using 2d range data. *International Journal of Social Robotics*, 2(1):31–40, 2010.

[60] Mercè Teixidó, Tomàs Pallejà, Marcel Tresanchez, Miquel Nogués, and Jordi Palacín. Measuring oscillating walking paths with a lidar. *Sensors*, 11(5):5071–5086, 2011.

[61] Woojin Chung, Hoyeon Kim, Yoonkyu Yoo, Chang-Bae Moon, and Jooyoung Park. The detection and following of human legs through inductive approaches for a mobile robot with a single laser range finder. *IEEE Transactions on Industrial Electronics*, 59(8):3156–3166, 2012.

[62] Tetsuya Matsumura, Toshiki Moriguchi, Minoru Yamada, Kazuki Uemura, Shu Nishiguchi, Tomoki Aoyama, and Masaki Takahashi. Development of measurement system for task oriented step tracking using laser range finder. *Journal of NeuroEngineering and Rehabilitation*, 10(1):47, 2013.

[63] Carlos A. Cifuentes, Anselmo Frizera, Ricardo Carelli, and Teodiano Bastos. Human–robot interaction based on wearable imu sensor and laser range finder. *Robotics and Autonomous Systems*, 62(10):1425–1439, 2014.

[64] Jing Yuan, Huan Chen, Fengchi Sun, and Yalou Huang. Multisensor information fusion for people tracking with a mobile robot: A particle filtering approach. *IEEE Transactions on Instrumentation and Measurement*, 64(9):2427–2442, 2015.

[65] Ayanori Yorozu, Shu Nishiguchi, Minoru Yamada, Tomoki Aoyama, Toshiki Moriguchi, and Masaki Takahashi. Gait measurement system for the multi-target stepping task using a laser range sensor. *Sensors*, 15(5):11151–11168, 2015.

[66] Ayanori Yorozu, Toshiki Moriguchi, and Masaki Takahashi. Improved leg tracking considering gait phase and spline-based interpolation during turning motion in walk tests. *Sensors*, 15(9):22451–22472, 2015.

[67] Yoonchang Sung and Woojin Chung. Hierarchical sample-based joint probabilistic data association filter for following human legs using a mobile robot in a cluttered environment. *IEEE Transactions on Human-Machine Systems*, 46(3):340–349, 2016.

[68] Lucas Beyer, Alexander Hermans, Timm Linder, Kai O. Arras, and Bastian Leibe. Deep person detection in two-dimensional range data. *IEEE Robotics and Automation Letters*, 3(3):2726–2733, 2018.

[69] Ángel Manuel Guerrero-Higueras, Claudia Álvarez-Aparicio, Maria Carmen Calvo Olivera, Francisco J Rodríguez-Lera, Camino Fernández-Llamas, Francisco Martín Rico, and Vicente Matellán. Tracking people in a mobile robot from 2d lidar scans using full convolutional neural networks for security in cluttered environments. *Frontiers in Neurorobotics*, 12:85, 2019.

[70] Claudia Álvarez-Aparicio, Ángel Manuel Guerrero-Higueras, Francisco Javier Rodríguez-Lera, Jonatan Ginés Clavero, Francisco Martín Rico, and Vicente Matellán. People detection and tracking using lidar sensors. *Robotics*, 8(3):75, 2019.

[71] Ayanori Yorozu and Masaki Takahashi. Estimation of body direction based on gait for service robot applications. *Robotics and Autonomous Systems*, 132:12, 2020.

[72] Huu Toan Duong and Young Soo Suh. Human gait tracking for normal people and walker users using a 2d lidar. *IEEE Sensors Journal*, 20(11):6191–6199, 2020.

[73] Julia M. Leach, Sabato Mellone, Pierpaolo Palumbo, Stefania Bandinelli, and Lorenzo Chiari. Natural turn measures predict recurrent falls in community-dwelling older adults: a longitudinal cohort study. *Scientific Reports*, 8(1):1–9, 2018.

[74] Marco Godi, Marica Giardini, and Marco Schieppati. Walking along curved trajectories. changes with age and parkinson's disease. hints to rehabilitation. *Frontiers in Neurology*, 10:532, 2019.

[75] Bruce Brownstein. Migration and design characteristics of functional knee braces. *Journal of Sport Rehabilitation*, 7(1):33–43, 1998.

[76] Jonathan C. Singer and Mario Lamontagne. The effect of functional knee brace design and hinge misalignment on lower limb joint mechanics. *Clinical Biomechanics*, 23(1):52–59, 2008.

[77] Dylan F. Glas, Takahiro Miyashita, Hiroshi Ishiguro, and Norihiro Hagita. Laser-based tracking of human position and orientation using parametric shape modeling. *Advanced Robotics*, 23(4):405–428, 2009.

[78] Paul Voigt and Axel Von dem Bussche. The eu general data protection regulation (gdpr). *A Practical Guide, 1st Ed., Cham: Springer International Publishing*, 2017.

[79] Lin Shu, Tao Hua, Yangyong Wang, Qiao Li, David Dagan Feng, and Xiaoming Tao. In-shoe plantar pressure measurement and analysis system based on fabric pressure sensing array. *IEEE Transactions on Information Technology in Biomedicine*, 14(3):767–775, 2010.

[80] Jacquelin Perry and Judith M. Burnfield. Kinetics of gait ground reaction forces vectors moments power and pressure. In *Gait Analysis*, pages 457–469. SLACK, 2010.

[81] Ava Segal, Eric Rohr, Michael Orendurff, Jane Shofer, Matthew O'Brien, and Bruce Sangeorzan. The effect of walking speed on peak plantar pressure. *Foot & Ankle International*, 25(12):926–933, 2004.

[82] Tony S. Keller, A. M. Weisberger, J. L. Ray, S. S. Hasan, R. G. Shiavi, and D. M. Spengler. Relationship between vertical ground reaction force and speed during walking, slow jogging, and running. *Clinical Biomechanics*, 11(5):253–259, 1996.

[83] Jeffrey M. Hausdorff, Zvi Ladin, and Jeanne Y. Wei. Footswitch system for measurement of the temporal parameters of gait. *Journal of Biomechanics*, 28(3):347–351, 1995.

[84] Ryo Eguchi, Ayanori Yorozu, and Masaki Takahashi. Kinetic and spatiotemporal gait analysis system using instrumented insoles and laser range sensor. In *2017 IEEE International Conference on Systems, Man, and Cybernetics (SMC)*, pages 705–709. IEEE, 2017.

[85] Veerle Segers, Peter Aerts, M. Lenoir, and Dirk De Clercq. Spatiotemporal characteristics of the walk-to-run and run-to-walk transition when gradually changing speed. *Gait & Posture*, 24(2):247–254, 2006.

[86] Felix Hebenstreit, Andreas Leibold, Sebastian Krinner, Götz Welsch, Matthias Lochmann, and Bjoern M. Eskofier. Effect of walking speed on gait sub phase durations. *Human Movement Science*, 43:118–124, 2015.

[87] Ryo Eguchi and Masaki Takahashi. Validity of the nintendo wii balance board for kinetic gait analysis. *Applied Sciences*, 8(2), 2018.

[88] Ryo Eguchi, Ayanori Yorozu, Takahiko Fukumoto, and Masaki Takahashi. Ground reaction force estimation using insole plantar pressure measurement system from single-leg standing. In *2016 IEEE International Conference on Multisensor Fusion and Integration for Intelligent Systems (MFI)*, pages 109–113. IEEE, 2016.

[89] Ryo Eguchi, Ayanori Yorozu, and Masaki Takahashi. Accessible ground reaction force estimation using insole force sensors without force plates. In *2017 11th Asian Control Conference (ASCC)*, pages 2861–2865. IEEE, 2017.

[90] Ross A. Clark, Adam L. Bryant, Yonghao Pua, Paul McCrory, Kim Bennell, and Michael Hunt. Validity and reliability of the nintendo wii balance board for assessment of standing balance. *Gait & Posture*, 31(3):307–310, 2010.

[91] Ross Allan Clark, Rian McGough, and Kade Paterson. Reliability of an inexpensive and portable dynamic weight bearing asymmetry assessment system incorporating dual nintendo wii balance boards. *Gait & Posture*, 34(2):288–291, 2011.

[92] Frank Koslucher, Michael G. Wade, Brent Nelson, Kelvin Lim, Fu-Chen Chen, and Thomas A. Stoffregen. Nintendo wii balance board is sensitive to effects of visual tasks on standing sway in healthy elderly adults. *Gait & Posture*, 36(3):605–608, 2012.

[93] Erik A. Wikstrom. Validity and reliability of nintendo wii fit balance scores. *Journal of Athletic Training*, 47(3):306–313, 2012.

[94] Arnold Huurnink, Duncan P. Fransz, Idsart Kingma, and Jaap H. van Dieen. Comparison of a laboratory grade force platform with a nintendo wii balance board on measurement of postural control in single-leg stance balance tasks. *Journal of Biomechanics*, 46(7):1392–1395, 2013.

[95] Julia M. Leach, Martina Mancini, Robert J. Peterka, Tamara L. Hayes, and Fay B. Horak. Validating and calibrating the nintendo wii balance board to derive reliable center of pressure measures. *Sensors*, 14(10):18244–18267, 2014.

[96] Pietro Scaglioni-Solano and Luis F. Aragon-Vargas. Validity and reliability of the nintendo wii balance board to assess standing balance and sensory integration in highly functional older adults. *International Journal of Rehabilitation Research*, 37(2):138–143, 2014.

[97] Jeffrey D. Holmes, Mary E. Jenkins, Andrew M. Johnson, Michael A. Hunt, and Ross A. Clark. Validity of the nintendo wii® balance board for the assessment of standing balance in parkinson's disease. *Clinical Rehabilitation*, 27(4):361–366, 2013.

[98] Giacomo Severini, Sofia Straudi, Claudia Pavarelli, Marco Da Roit, Carlotta Martinuzzi, Laura Di Marco Pizzongolo, and Nino Basaglia. Use of nintendo wii balance board for posturographic analysis of multiple sclerosis patients with minimal balance impairment. *Journal of NeuroEngineering and Rehabilitation*, 14, 2017.

[99] Go Yamako, Etsuo Chosa, Koji Totoribe, Yuu Fukao, and Gang Deng. Quantification of the sit-to-stand movement for monitoring age-related motor deterioration using the nintendo wii balance board. *Plos One*, 12(11), 2017.

[100] Sumayeh Abujaber, Gregory Gillispie, Adam Marmon, and Jr. Zeni, Joseph. Validity of the nintendo wii balance board to assess weight bearing asymmetry during sit-to-stand and return-to-sit task. *Gait & Posture*, 41(2):676–682, 2015.

[101] Keizo Yamamoto and Mamoru Matsuzawa. Validity of a jump training apparatus using wii balance board. *Gait & Posture*, 38(1):132–135, 2013.

[102] Julien Audiffren and Emile Contal. Preprocessing the nintendo wii board signal to derive more accurate descriptors of statokinesigrams. *Sensors*, 16(8):1208, 2016.

[103] Christopher K. I. Williams and Carl Edward Rasmussen. *Gaussian Processes for Machine Learning*. Gaussian Processes for Machine Learning. 2005.

[104] Nicole A. Wilson, B. Tom Mazahery, Jason L. Koh, and Li-Qun Zhang. Effect of bracing on dynamic patellofemoral contact mechanics. *Journal of Rehabilitation Research & Development*, 47(6):531–542, 2010.

[105] Baptiste Pierrat, Carine Millot, Jérôme Molimard, Laurent Navarro, Paul Calmels, Pascal Edouard, and Stéphane Avril. Characterisation of knee brace migration and associated skin deformation during flexion by full-field measurements. *Experimental Mechanics*, 55(2):349–360, 2015.

[106] Aude Billard, Sylvain Calinon, Ruediger Dillmann, and Stefan Schaal. Survey: Robot programming by demonstration. *Springer Handbook of Robotics*, pages 1371–1394, 2008.

[107] Gap filling algorithm: Rigid Body, VICON Support FAQs for software, Vicon Nexus.

[108] Klaudia Kozlowska, Miroslaw Latka, and Bruce J. West. Asymmetry of short-term control of spatio-temporal gait parameters during treadmill walking. *Scientific Reports*, 7:44349, 2017.

List of Achievements

Journals (Related to this dissertation)

[1] Ryo Eguchi, Brendan Michael, Matthew Howard, and Masaki Takahashi. Shift-Adaptive Estimation of Joint Angle Using Instrumented Brace With Two Stretch Sensors Based on Gaussian Mixture Models. *IEEE Robotics and Automation Letters*, 5(4):5881–5888, 2020.

[2] Ryo Eguchi, Ayanori Yorozu, Takahiko Fukumoto, and Masaki Takahashi. Estimation of Vertical Ground Reaction Force Using Low-Cost Insole With Force Plate-Free Learning from Single Leg Stance and Walking. *IEEE Journal of Biomedical and Health Informatics*, 24(5):1276–1283, 2020.

[3] Ryo Eguchi and Masaki Takahashi. Insole-Based Estimation of Vertical Ground Reaction Force Using One-Step Learning With Probabilistic Regression and Data Augmentation. *IEEE Transactions on Neural Systems and Rehabilitation Engineering*, 27(6):1217–1225, 2019.

Journals (Others)

[1] Koji Fujita, Hirotaka Iijima, Ryo Eguchi, Tomoyuki Kuroiwa, Toru Sasaki, Hiroyuki Yokoyama, Takafumi Koyama, Akimoto Nimura, Ryuichi Kato, Atsushi Okawa, and Masaki Takahashi. Gait analysis of patients with distal radius fracture by using a novel laser Timed Up-and-Go system. *Gait & Posture*, 80:223–227, 2020.

[2] Hirotaka Iijima, Ryo Eguchi, Kanako Shimoura, Keisuke Yamada, Tomoki Aoyama, and Masaki Takahashi. Transcutaneous Electrical Nerve Stimulation Improves Stair Climbing Capacity in People with Knee Osteoarthritis. *Scientific Reports*, 10(1):7294, 2020.

[3] Hirotaka Iijima, Ayanori Yorozu, Yusuke Suzuki, Ryo Eguchi, Tomoki Aoyama, and Masaki Takahashi. Hip abductor muscle weakness and slowed turning motion in people with knee osteoarthritis. *Journal of Biomechanics*, 101, 2020.

[4] Hala Zeidan, Ryo Eguchi, Hirotaka Iijima, Koji Fujimoto, Masaki Takahashi, Tomoki Aoyama, Yusuke Suzuki, Yuu Kajiwara, Keiko Harada, Kengo Nakai, and Kanako Shimoura. Detailed analysis of the transverse arch of hallux valgus feet with and without pain using weight-bearing ultrasound imaging and precise force sensors. *PLOS ONE*, 15(1), 2020.

[5] Hirotaka Iijima, Ryo Eguchi, Kanako Shimoura, Tomoki Aoyama, and Masaki Takahashi. Stair climbing ability in patients with early knee osteoarthritis: Defining the clinical hallmarks of early disease. *Gait & Posture*, 72:148–153, 2019.

[6] Hirotaka Iijima, Tomoki Aoyama, Ryo Eguchi, Masaki Takahashi, and Shuichi Matsuda. Effects of interaction between varus thrust and ambulatory physical activity on knee pain in individuals with knee osteoarthritis: an exploratory study with 12-month follow-up. *Clinical Rheumatology*, 38(6):1721–1729, 2019.

[7] Hirotaka Iijima, Kanako Shimoura, Ryo Eguchi, Tomoki Aoyama, and Masaki Takahashi. Concurrent validity and measurement error of stair climb test in people with pre-radiographic to mild knee osteoarthritis. *Gait & Posture*, 68:335–339, 2019.

[8] Hirotaka Iijima, Ryo Eguchi, Tomoki Aoyama, and Masaki Takahashi. Trunk movement asymmetry associated with pain, disability, and quadriceps strength asymmetry in individuals with knee osteoarthritis: a cross-sectional study. *Osteoarthritis and Cartilage*, 27(2):248–256, 2019.

[9] Ryo Eguchi and Masaki Takahashi. Validity of the Nintendo Wii Balance Board for Kinetic Gait Analysis. *Applied Sciences*, 8(2):1–10, 2018.

International conference (Full-length papers with reviews)

[1] Tomoko Ono, *Ryo Eguchi and Masaki Takahashi. Dynamic Motion Tracking Based on Point Cloud Matching with Personalized Body Segmentation. *The 8th IEEE RAS/EMBS International Conference on Biomedical Robotics and Biomechatronics (BioRob2020)*, pp. 61–67, Online, November 2020 (Oral presentation).

[2] *Ryo Eguchi, Brendan Michael, Matthew Howard, and Masaki Takahashi. Shift-adaptive Estimation of Joint Angle Using Instrumented Brace With Two Stretch Sensors Based on Gaussian Mixture Models. *The 2020 IEEE/RSJ International Conference on Intelligent Robots and Systems (IROS2020)*, Online, October 2020 (Oral presentation).

[3] *Ryo Eguchi, Ayanori Yorozu, and Masaki Takahashi. Spatiotemporal and Kinetic Gait Analysis System Based on Multisensor Fusion of Laser Range Sensor and Instrumented Insoles. *The 2019 IEEE International Conference on Robotics and Automation (ICRA2019)*, pp. 4876–4881, Montreal, Canada, May 2019 (Interactive presentation).

[4] *Ryo Eguchi and Masaki Takahashi. Accessible Calibration of Insole Force Sensors Using the Wii Balance Board for Kinetic Gait Analysis. *IEEE SENSORS 2018*, pp. 1–4, New Delhi, India, October 2018 (Poster presentation).

[5] *Ryo Eguchi, Ayanori Yorozu, and Masaki Takahashi, Accessible Ground Reaction Force Estimation Using Insole Force Sensors without Force Plates. *The 11th Asian Control Conference (ASCC2017)*, pp. 2861–2865, Gold Coast, Australia, December 2017 (Oral presentation).

[6] *Ryo Eguchi, Ayanori Yorozu, and Masaki Takahashi. Kinetic and Spatiotemporal Gait Analysis System Using Instrumented Insoles and Laser Range Sensor. *The 2017 IEEE International Conference on Systems, Man, and Cybernetics (SMC2017)*, pp. 705–709, Banff, Canada, October 2017 (Oral presentation).

[7] *Ryo Eguchi, Ayanori Yorozu, Takahiko Fukumoto, and Masaki Takahashi. Ground Reaction Force Estimation Using Insole Plantar Pressure Measurement System from Single-Leg Standing. *The 2016 IEEE International Conference on Multisensor Fusion and Integration for Intelligent Systems (MFI2016)*, pp. 109–113, Baden-Baden, Germany, September 2016 (Oral presentation).

International conference (Others)

None.

Domestic conference (in Japanese)

[1] *Ryo Eguchi and Masaki Takahashi. Human Leg Tracking System Based on Fusion of Laser Range Sensor and Instrumented Insoles Using Learning-based Occlusion Compensation. *JSME Symposium : Sports engineering and Human Dynamics 2020 (SHD2020)*, Online, November 2020 (Oral presentation).

[2] *Ryo Eguchi, Masaki Takahashi, Brendan Michael, and Matthew Howard. Joint Angle Measurement System Using Smart Knee Brace with Stretch Sensors Based on Stochastic

Machine Learning. *JSME Symposium : Sports engineering and Human Dynamics 2019 (SHD2019)*, Fukuoka, Japan, October 2019 (Oral presentation).

[3] *Ryo Eguchi and Masaki Takahashi. Insole-based Estimation of Vertical Ground Reaction Force Using One-step Learning With Probabilistic Regression and Data Augmentation. *LIFE2019*, Tokyo, Japan, September 2019 (Oral presentation).

[4] *Ryo Eguchi and Masaki Takahashi. Kinetic Gait Analysis System Using Instrumented Insoles Based on Accessible Calibration with Wii Balance Board. *JSME Symposium : Sports engineering and Human Dynamics 2018 (D&D2018)*, Kyoto, Japan, November 2018 (Oral presentation).

[5] *Ryo Eguchi, Ayanori Yorozu, and Masaki Takahashi. Kinetic and Spatiotemporal Gait Analysis System Based on Sensor Fusion Using Instrumented Insoles and Laser Range Sensor. *LIFE2018*, Tokyo, Japan, September 2018 (Oral presentation).

[6] *Ryo Eguchi, Ayanori Yorozu, and Masaki Takahashi. Multisensor Based Leg Tracking in Walking on Circle Trajectory by Fusing Laser Range Sensor and Instrumented Insoles. *Dynamics and Design Conference 2018 (D&D2018)*, Tokyo, Japan, August 2018 (Oral presentation).

[7] *Ryo Eguchi, Ayanori Yorozu, and Masaki Takahashi. Development of Spatiotemporal and Kinetic Gait Analysis System for TUG. *LIFE2017*, Tokyo, Japan, September 2017 (Oral presentation).

[8] *Ryo Eguchi, Ayanori Yorozu, and Masaki Takahashi. Kinetic and Spatiotemporal Gait Analysis System Using Instrumented Insoles and Laser Range Sensor. *Dynamics and Design Conference 2017 (D&D2017)*, Toyohashi, Japan, August 2017 (Oral presentation).

[9] *Ryo Eguchi, Ayanori Yorozu, Takahiko Fukumoto, and Masaki Takahashi. Development of insole Plantar Pressure Measurement System. *LIFE2016*, Sendai, Japan, September 2016 (Oral presentation).

Others (Awards and Prizes)

[1] IEEE Signal Processing Society Japan Student Journal Paper Award, December 2020.

[2] SICE International Young Authors Award (*IROS2020*), October 2020.

[3] JSME Sports Engineering & Human Dynamics Division Student Excellent Presentation Award (*SHD2018*), January 2019.

[4] Foundation of Barrier-Free System Integration Encouragement Award finalist (*LIFE2018*), September 2018.